Study of One-nucleon Transfer Reactions

A Dissertation Presented for the

Doctor of Philosophy

Degree

The University of Tennessee, Knoxville

Jerome Mathew Kovoor

May 2022

© by Jerome Mathew Kovoor, 2022
All Rights Reserved.

For my family and friends

Acknowledgments

I would like to thank :

My advisor, Dr. Kate Jones for welcoming me to the group, guiding me on the research and analysis, sending me to various experiments and workshops, and diligently reviewing multiple abstracts and presentations. With her support, I have been able to improve my research and presentation skills. Dr. Rituparna Kanungo for discussions and suggestions on the ^{13}Be analysis, and my doctoral committee members Dr. Thomas Papenbrock, Dr. Miguel Madurga, and Dr. Lawrence Heilbronn for their valuable feedback and their time.

Dr. Marija Vostinar for her time and effort in conveying to me the details of the ^{13}Be experiment that I was not a part of, and for teaching me the basics of nuclear data analysis. Dr. Sean Burcher for helping me get accustomed to the group and the research activities. Dr. Josh Hooker for introducing me to advanced data analysis techniques and simulations, and improving my programming skills.

Dr. Steve Pain for many valuable discussions on the ^{13}Be data analysis and giving me the opportunity to work with him on GODDESS experiments. Dr. Robert Grzywacz for teaching me different data acquisition techniques and guidance on the NEXT project. Dr. Kelly Chipps for proposing and helping me with this experiment.

All the collaborators who have helped make these experiments possible by helping with the setup and experiment shifts. My groupmates, especially, Rajesh Ghimire, Shree Neupane, Thomas King, Dr. Harry Sims, Dr. Nori Kitamura, and Dr. Joseph Heideman for their help at various stages of my graduate research. My friends mainly, Yadu Krishnan, Dony Varghese, Rakesh Kamath, Lakshmi Sundaresh, Akhil Francis, and Belvin Thomas for their support and help during my life in Knoxville.

Finally, I want to thank my family for their unwavering love and support.

Abstract

The structure of nuclei away from the line of stability and near the driplines in the nuclear chart has been of huge interest since the arrival of radioactive ion beam facilities. The properties of nuclei evolve as a function of proton and neutron numbers and understanding the mechanisms behind this is one of the keys to explaining the strong nuclear force. Single-nucleon transfer reactions using deuteron targets are powerful probes of nuclear structure when the emitted proton or neutron is measured with high fidelity.

A variety of structure phenomena are observed in the beryllium isotopes marking them particularly attractive for nuclear structure studies. The structure of ^{13}Be offers insights into the N=8 shell gap, the nature of the Borromean nucleus ^{14}Be, the influence of continuum, and the nature of neutron drip-line nuclei. However, despite the significant number of experiments performed over the last three decades, the energies and ordering of the low-lying resonances are less certain.

A ^{12}Be(d,p)^{13}Be transfer reaction was performed in inverse kinematics at ISAC II at TRIUMF. The ^{12}Be beam at 9.5 MeV/u interacted with the novel IRIS solid D_2 target, and ejectiles and recoils were detected in an annular silicon detector array and two delta E -E telescopes, respectively. A Q-value plot showing the population of resonances in the ^{13}Be continuum was obtained, and it was fitted using GEANT4 simulations, in combination with Bayesian optimization. An angular distribution of the lowest-lying strength in ^{13}Be was obtained, and it was fitted with DWBA calculations using different combinations of optical model potentials. Results from this work will be presented here, along with interpretations of five previous works performed on ^{13}Be, in comparison with our data.

The NEXT detector is a novel, high precision, segmented neutron detector which offers excellent position and timing resolution. It uses a pulse shape discriminating plastic

scintillator, which is crucial in identifying neutrons from a gamma-ray background in reaction experiments. A ^{20}Ne(d,n)^{21}Na proton transfer reaction was performed at ReA6 at NSCL to benchmark this detector for reaction experiment studies. The details and preliminary results of this experiment will also be presented.

Table of Contents

1 Introduction **1**

1.1 Nuclear Shell Model (NSM) 4

1.2 Deformed Shell Model 6

1.2.1 Nilsson Model 9

1.3 Halo Nuclei 11

1.4 Inversion of Levels 13

1.5 Previous studies of ^{13}Be 13

2 Theoretical Background **17**

2.1 Nuclear Reactions 17

2.1.1 Types of nuclear reactions 18

2.2 Reaction Kinematics 20

2.3 Distorted Wave Born Approximation 23

2.4 Optical Potentials 24

2.4.1 Deuteron global optical potentials for (d,p) entrance channel 26

2.4.2 Nucleon-nucleus optical potentials for (d,p) exit channel 27

3 Experimental Setup **28**

3.1 ISAC: Isotope Separator and Accelerator 28

3.2 IRIS: The ISAC charged particle reaction spectroscopy station 30

3.2.1 Ionization chamber 30

3.2.2 Solid D_2 target 32

3.2.3 Charged particle detectors 34

3.3 Signal Processing 36
3.4 Specifics of the experiment 38

4 Data Analysis **39**
4.1 Beam Identification 39
4.2 Energy Calibration of the Detectors 39
4.2.1 Calibration of the YU detectors 41
4.2.2 Calibration of the S3 detectors 41
4.3 Target Thickness Estimation 44
4.4 ^{12}C(d, p)^{13}C Reaction 44
4.5 ^{12}Be(d,p)^{13}Be Reaction 48
4.6 GEANT4 Simulations 57
4.7 Bayesian Optimization 57
4.7.1 Gaussian Process 59
4.7.2 Acquisition Functions 60

5 Results and Discussion **64**
5.1 Nilsson Levels 64
5.2 Bayesian Optimization and GEANT4 Simulations 66
5.3 Angular distributions 69
5.4 Interpretation of the Results 77
5.5 Discussion 80

6 Study of (d, n) Reactions Using NEXT **86**
6.1 Introduction to Neutron Detectors 86
6.2 NEXT Detector 90
6.2.1 Neutron-gamma discrimination 92
6.3 ^{20}Ne(d, n)^{21}Na at ReA6 NSCL 92
6.3.1 Experiment Setup 94
6.3.2 Measurements using NEXT 95
6.3.3 Compton Scattering and Detector Light Response 98

6.3.4 Preliminary Analysis and Results 101
6.3.5 Summary and Future Work 106

Bibliography **107**

Vita **117**

List of Tables

1.1 Some of the previously performed theoretical calculations to study the structure of ^{13}Be. Only the first three low-lying states for each calculation are shown here. These were shell model calculations. 15

1.2 Some of the previously performed measurements to study the structure of ^{13}Be. Only the low-lying states, up to 2 MeV above the threshold are shown here. Strength 1a represents the lowest reported resonance or a virtual s-wave state, 1b represents the next highest-lying resonance, and 2 represents resonance around 2 MeV. E_r denotes the energy in the case of a resonance, and a_s is the scattering length in the case of a virtual s-wave state. 16

4.1 A table showing the Q values of the states populated in ^{13}C using ^{12}C + d reaction. The ground and the first excited states were able to be resolved. The second and the third excited states were unresolved and hence that peak in the Q-vale spectrum was fitted using a single Gaussian function. Previously measured Q values of the ground state and the first excited states are given for comparison ^{13}C. The standard deviations of the fits are also shown. . . . 50

4.2 A table showing the Q values of the resonances in ^{13}Be using ^{12}Be + d reaction. The energies above the neutron threshold, Lorentzian width, and the Gaussian S.D. of the pseudo-Voigt function are also displayed. The Gaussian S.D.s are too small and hence these values cannot be used to model the ^{13}Be Q-value spectrum. 56

5.1 A table showing the Q values and the Breit-Wigner widths of the two strengths in the continuum of ^{13}Be, obtained by fitting the Q-value spectrum of ^{12}Be + d reaction, using GEANT4 simulations and Bayesian optimization 71
5.2 The fit parameters for the angular distribution obtained from the DWBA calculations performed using FRESCO with Daehnick Global, Lohr-Haeberli, and Perey-Perey potentials as the deuteron vertex potential and Koning-Delaroche potential as the proton vertex potential. 76
5.3 The results from fitting the data with the results from experiments performed by Kondo et al., Aksyutina et al., Randisi et al., Ribeiro et al., and Corsi et al., compared with the results from this work 84

List of Figures

1.1 Chart of nuclides showing the decay modes 2

1.2 Nuclear Shell Model 7

1.3 Nilsson Model for neutron levels in nuclei with $A \leq 50$. 10

1.4 Figures showing some of the exotic phenomena in nuclei as the neutron to proton ratio changes. 12

2.1 Two body reaction 21

2.2 The energy of the outgoing proton as a function of the angle in a $^{12}\mathrm{C}(\mathrm{d},\mathrm{p})^{13}\mathrm{C}$ reaction; shows the first four states of $^{13}\mathrm{C}$ being populated in the laboratory frame. Here, 'GS' and 'ES' stand for the ground state and excited state, respectively 22

3.1 Schematic of ISAC 29

3.2 Schematics of the experiment setup and the ionization chamber 31

3.3 (a) shows the silver backing foil. (b) shows the solid hydrogen target cell. (c) is a view of the heat shield. A cartoon of the beam and ejectile is shown using yellow and red arrows, respectively. 33

3.4 Pictures of the YY1 detector 35

3.5 Pictures of the CsI and Micron S3 detectors 37

4.1 Beam energy loss through the ionization chamber is shown in the channel number. The peak marked with the red gates corresponds to the ^{12}Be beam and the other peak is from noise 40

4.2 Calibration of a YU detector strip with ADC channel number, showing three peaks arising from ^{239}Pu, ^{241}Am, and ^{244}Cm emitting alpha particles of energy 5.155 MeV, 5.486 MeV, and 5.805 MeV respectively. The fine structure of the decay can be seen for each of the nuclei. The decay channel with the highest branching ratio was chosen for calibration. The red line is a convolution of three Gaussian functions. 42

4.3 Calibration of an SD1 detector ring with ADC channel number, showing three peaks arising from ^{239}Pu, ^{241}Am, and ^{244}Cm emitting alpha particles of energy 5.155 MeV, 5.486 MeV, and 5.805 MeV respectively. The red line is a convolution of three Gaussian functions. 43

4.4 Reconstructed SD energy of the beam from the ^{12}Be beam run. This is the energy of the beam after it passes through the silver foil. The red peak shows the energy of the beam with only the silver foil and the blue peak shows the energy of the beam with the solid deuterium target and silver foil backing. The thickness of the target can be calculated from the difference in energy. . 45

4.5 Particle identification plot for recoils from the ^{12}C + d data from the SD telescope. The red cut includes both the ^{13}C and the scattered ^{12}C, the black gate shows the elastic scattering, and the maroon circle shows the ^{4}He punch-through point. 46

4.6 Proton energy versus angle in the laboratory frame following the ^{12}C + d reaction after gating on the IC and the PID plot, and a detector threshold of 500 keV. Calculations of the kinematics for populating the lowest four states in ^{13}C are shown using solid lines. 47

4.7 ^{13}C Q-value spectrum obtained from ^{12}C + d reaction. The data is shown as black points with statistical error bars. A global fit to the data is shown as a red line using a convolution of three Gaussian functions. Individual fits for the ground and the first excited states are shown. The second and third excited states were not able to be resolved. Hence, the unresolved peak was fitted using a single Gaussian function. 49

4.8 A Q-value spectrum calculated for ^{12}C beam impinging on the silver backing target shows no significant data after applying the gates on IC and PID, and applying the detector threshold. 51
4.9 Particle identification plot for recoils from the ^{12}Be + d data from the SD telescope. The red cut includes both the reacted and scattered ^{12}Be, the black gate shows the elastic scattering, the pink and the maroon circles show the ^{6}Li and ^{4}He punch-through points, respectively. 52
4.10 Proton energy versus angle in the laboratory frame following the ^{12}Be + d reaction after gating on the IC and the PID plot, and applying a detector threshold of 200 keV. The highest Q values populated in the reaction can be seen here and the spectrum is clean above this line. 53
4.11 ^{13}Be Q-value spectrum obtained from ^{12}Be + d reaction. The data is shown as black points with statistical error bars. A global fit to the data is shown as a pink line using a convolution of three pseudo-Voigt functions to model three resonances. 55
4.12 Bayesian optimization iterations performed to maximize the test function $f(x) = \left(1/(x^2+1) + e^{-(x-4)^2/2}\right)\sin(x)$ (green line). Three random evaluation points are shown as red markers. The objective function is displayed using a green curve. The mean, 1σ, and 2σ confidence intervals of the GP are shown as the black dashed line, dark blue, and light-shaded areas, respectively. The next point of evaluation obtained from the UCB acquisition function is displayed as a yellow star. As the BayesOpt routine progresses, the algorithm converges on the maximum of the function. 62

5.1 (a) shows Nilsson level diagram for neutrons for light nuclei. (b) shows a schematic of the levels for ^{13}Be obtained by projecting the Nilsson diagram for $\epsilon = 0.61$. 65

5.2 ^{13}Be Q-value spectrum obtained from ^{12}Be + d reaction. The data is shown as black points with statistical error bars. A global fit to the data obtained using Bayesian optimization is shown as a red line. Low-lying strength lying at 0.55 MeV above the threshold is denoted as a blue-dashed line. Strength at 2.2 MeV above the threshold is shown as a green dot-dashed line. The non-resonant background is shown as a black dotted line. 68

5.3 The width of strength 1 was varied from the optimum value (χ^2_{min})and the simulations were carried out and the data was fitted. The χ^2 values for these fits are plotted against the widths in red color. The blue horizontal line shows where the χ^2 value becomes $\chi^2_{min} + 1$. The corresponding widths were used as the 1σ confidence interval. It is shown as green dashed lines. 70

5.4 An angular distribution plot fitted with DWBA calculations performed using FRESCO with Daehnick Global potential as the deuteron vertex potential and Koning-Delaroche potential as the proton vertex potential. Plot (a) shows data fitted with pure waves and plot (b) shows data fitted with a mixture of waves. 73

5.5 An angular distribution plot fitted with DWBA calculations performed using FRESCO with Lohr-Haeberli potential as the deuteron vertex potential and Koning-Delaroche potential as the proton vertex potential. Plot (a) shows data fitted with pure waves and plot (b) shows data fitted with a mixture of waves. 74

5.6 An angular distribution plot fitted with DWBA calculations performed using FRESCO with Perey-Perey potential as the deuteron vertex potential and Koning-Delaroche potential as the proton vertex potential. Plot (a) shows data fitted with pure waves and plot (b) shows data fitted with a mixture of waves. 75

5.7 Data fitted with GEANT4 simulations with energy and widths obtained from Randisi et al. The amplitude of the states were used from the angular distributions which were 89% of s wave and 11% of d wave 78

5.8 Data fitted with GEANT4 simulations with energy and widths obtained from Ribeiro et al. The amplitudes of the states were used from the angular distributions which were 39% of p wave and 61% of s wave 79
5.9 Data fitted with GEANT4 simulations with energy and widths obtained from Kondo et al. The amplitudes of the states were used from the angular distributions which were 61% of s wave and 39% of p wave 81
5.10 Data fitted with GEANT4 simulations with energy and widths obtained from Corsi et al. The amplitude of the states were used from the angular distributions which were 61% of s wave and 39% of p wave 82
5.11 Data fitted with GEANT4 simulations with energy and widths obtained from Aksyutina et al. The amplitudes of the states were used directly obtained from BayesOpt results. 83

6.1 Calculation of figure of merit for a plastic scintillation detector. 89
6.2 (a) shows the dimensions of a NEXT module. There are eight segments in the direction of neutrons. (b) shows a cross-sectional view of stacked scintillator crystals before they are wrapped. 91
6.3 (a) shows PSD-QDC histogram obtained from a NEXT module for a ^{252}Cf source. The two bands from neutrons and gammas can be clearly distinguished. (b) shows projection of the PSD-QDC histogram in the QDC range of 80000-90000. A FOM of 1.2 ± 0.06 was obtained using the criterion shown in Figure 6.1b. 93
6.4 Schematic of the beam production mechanism at the ReA facility, NSCL. . . 96
6.5 Signals from the EBIT (green), RF (cyan), and EBIT-gated RF (yellow). The EBIT-gated RF signal was used as the start trigger for the experiment. (b) shows a time period of 130 ms for the EBIT signal 97
6.6 (a) shows the experiment setup with reaction chamber carrying the target connected to the beamline and the beam stop Faraday cup. (b) shows eleven NEXT modules covering a laboratory angular range of 90° to 165°. 99

6.7 A photograph from inside the target chamber showing two C_2D_4 targets of thicknesses 0.5 mg/cm^2 and 2 mg/cm^2. A collimator was also used to take the data without the target. 100
6.8 QDC histogram with a ^{137}Cs source showing Compton plateau and Compton edge. 102
6.9 PSD histograms for module 10 from ^{20}Ne(d,n)^{21}Na reaction. The red gate shown in (a) is the locus of minimum between the gamma and neutron peaks, as shown in (b), for different QDC ranges. This gate was used to remove the gamma background. 104
6.10 TOF-QDC histograms 105

Chapter 1

Introduction

Nuclear physics is the study of the constituents of an atomic nucleus and the interactions between them. In the standard model, the strong nuclear force is described by the quantum chromodynamics (QCD) Lagrangian [1] and the degrees of freedom are quarks and gluons. A nucleon which is a constituent of a nucleus is made up of quarks and gluons. The strong interaction between the quarks mediated by gluons is weak and hence QCD is perturbative in the high energy regime, or at short distances, but non-perturbative at low energies. The degrees of freedom relevant at low energies are nucleonic degrees of freedom due to confinement and hence the interaction between nucleons can be considered an effective interaction between the quarks and gluons. In chiral effective field theory (EFT), nuclear interactions are mediated by mesons. There are different ab-initio (from first principles) calculation techniques that can be performed to understand the properties of nuclei where all nucleons are considered as interacting individually with each other via nucleon-nucleon (NN), three-nucleon (NNN), or higher-order interactions. Some of the examples of ab-initio calculations are the no-core shell model (NCSM) [2, 3], coupled-cluster (CC) [4, 5], quantum Monte Carlo (QMC) methods [6], etc. As the number of nucleons increases, these calculations become very computationally expensive to solve.

To organize different nuclides according to their properties, nuclear physicists designed the chart of nuclides, which is similar to the periodic table for atomic elements. It arranges the nuclei according to their atomic number, or the number of protons (Z along the y-axis) and the number of neutrons (N along the x-axis) as shown in Figure 1.1. It is also known as

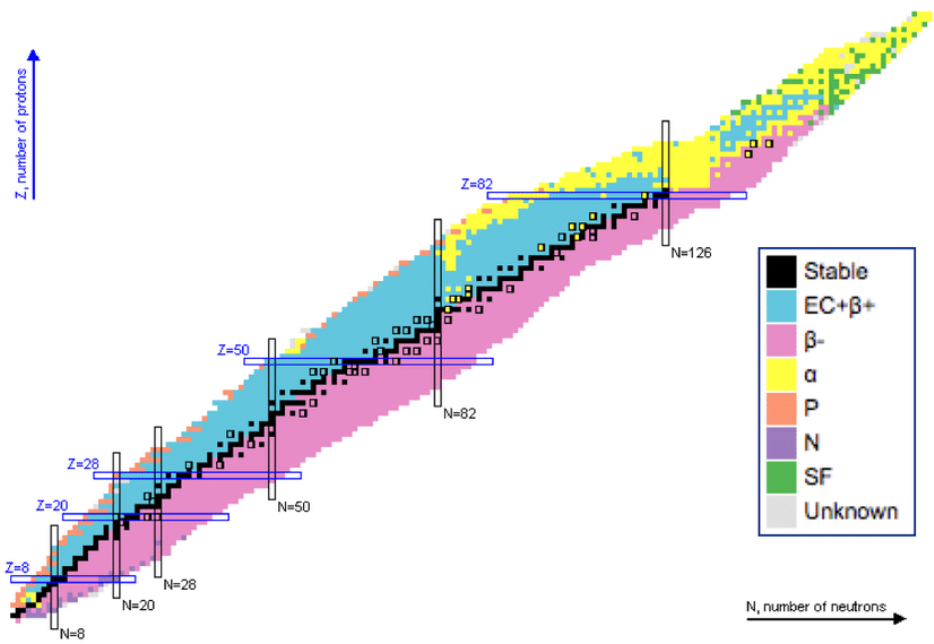

Figure 1.1: Chart of nuclides showing the decay modes, adapted from [7]. The magic numbers are shown by the labeled blue boxes.

Segrè Chart after the physicist Emilio Segrè. The nuclei marked in black are stable, while the other colors denote different modes of decays that those nuclei undergo. The boundaries of the chart are called the neutron drip-line (towards the neutron side) and the proton drip-line (towards the proton side). At the driplines, the valence neutrons and protons start to become unbound and begin to 'drop off' from the nucleus.

Exotic nuclei, which are nuclei far from stability, have been an important research area because they show a variety of new phenomena compared to stable nuclei. Several of these nuclei cannot be explained well using the well-known nuclear shell model because the traditional shell closures will start to disappear and new ones appear as you move away from stability. ^{11}Be is an example of N=8 shell-breakdown.

From the structural point of view, a particularly interesting type of exotic nuclei is halo nuclei. When the binding of the last one or two nucleons in a nucleus becomes very weak, they tend to extend from a well-defined core containing the rest of the nucleons [8]. The term 'halo' in this case means that there is an extended probability distribution of finding one or more nucleons outside a more compact structure. Hence, the radii of halo nuclei are exceptionally larger than those of otherwise similar systems. The first halo nucleus was discovered by Tanihata et al. at LBNL's Bevalac in 1985 [9] when they observed comparatively large interaction cross-sections for some neutron-rich helium and lithium isotopes. Studying these exceptional behaviors of exotic nuclei helps us in understanding the strong nuclear force. It became possible to study these systems experimentally with the advent of new radioactive ion beam facilities that could produce nuclei near the driplines of the nuclear chart.

Direct reactions are an excellent tool to study the single-particle structure of exotic nuclei because they happen on a very short time scale and can leave the rest of the nucleus unperturbed. Transfer reactions are a subgroup of direct reactions where the exchange of one or two nucleons happens between the participating nuclei. Specific examples of transfer reactions that will be studied in this project are neutron transfer e.g., the (d, p) reaction, and proton transfer e.g., the (d, n) reaction. In the (d, p) reaction, the neutron is transferred from the deuteron to the other participating nucleus and the proton is ejected while in the (d, n) reaction, the proton is transferred and the neutron is ejected. The angular distribution

of the ejected nucleon gives information about the angular momentum transferred. Single-nucleon transfer reactions are useful in studying the single-particle structure of nuclei. In the field of nuclear astrophysics, they are used as alternatives to study neutron capture and proton capture process owing to better cross-sections for transfer reactions compared to capture reactions. In this dissertation, we will be focusing on a neutron transfer experiment performed at TRIUMF to study the nuclear structure of a neutron unbound, exotic nucleus, ^{13}Be which has always been an enigma for the past few decades. In the last chapter, we will also be discussing a proton transfer experiment, which was performed to benchmark a novel neutron detector called NEXT for future reaction experiments.

1.1 Nuclear Shell Model (NSM)

The single-particle separation energy of a nucleus is defined as the energy required to remove the least bound nucleon from that nucleus. Experiments have revealed that nuclei having a certain number of protons show a higher proton separation energy and similarly higher neutron separation energy for a specific number of neutrons. In the 1930s, experiments performed to measure the binding energy of some nuclei revealed that these same numbers of protons and neutrons resulted in exceptionally high corresponding binding energies. These numbers later came to be known as the "magic numbers" and they are 2, 8, 20, 28, 50, 82, 126 [10]. The separation energy and binding energy are the highest for doubly-magic nuclei in which both neutrons and protons are of magic numbers. Some other experimental evidence for the shell model in nuclei includes a dip in neutron absorption cross-section of nuclei with a magic number of neutrons, large changes in electric quadrupole transition probability (B(E2)), and first 2^+ excited energy (E_{2^+}) in even N-even Z nuclei with a magic number of nucleons. To explain this shell structure of nucleons, the Nuclear Shell Model was introduced.

This model describes protons and neutrons as independent particles in the presence of a mean field due to the rest of the nucleons in the nucleus, giving the nucleons their own discrete energy levels. To the lowest order approximation, this field created by interactions among the nucleons is common to all the nucleons. The wavefunctions and energies of single

particles can be solved as a one-particle problem with a potential described by experimental findings.

To understand the shell model, one can use some of the simple potentials like infinite well potential and harmonic oscillator (HO) potential. But these potentials are not physical. The infinite well has sharp edges and to remove a nucleon, an infinite amount of energy needs to be applied which is not the case. The HO potential also tends to infinity as the distance increases. It is given by,

$$V(r) = \frac{1}{2}m\omega^2(r^2 - R^2). \tag{1.1}$$

Although the HO potential is not suitable to describe nuclear systems, it is good for a first-order approximation. The energy levels are equally spaced with energy given as,

$$E_N = \hbar\omega\left(N + \frac{3}{2}\right), \tag{1.2}$$

where, N is the number of oscillator quanta and $N = 2(n-1) + l$, n is the radial quantum number, l is the orbital angular momentum quantum number with, $n = 1, 2, 3, .., l = 0, 1, 2, ...$ The quantum number N defines a specific shell. The degeneracy of each l level is given by $2(2l+1)$ and of each N shell is given by $\frac{1}{2}(N+1)(N+2)$.

After solving the Schrödinger equation with these potentials, they both reproduce the magic numbers, 2, 8, and 20 but not the higher ones. In 1948, M. Goeppert Mayer, along with Otto Haxel, Hans Jensen, and Hans Seuss proposed a strong spin-orbit coupling term [11, 12], and adding this term to the potential was able to reproduce the higher magic numbers. Mayer and Jensen shared a Nobel Prize for this discovery. This term is given by,

$$V_{LS}(r) = -\frac{V^{'}(r)}{r}\vec{L}\cdot\vec{S}, \tag{1.3}$$

where $\vec{L}$ and $\vec{S}$ are angular and spin momentum operators respectively, $V^{'}(r)$ is the coupling strength and it peaks at the surface since it is the derivative of a volume term. This strong coupling term splits the degenerate l levels to $j = l \pm 1/2$ and each j-level has a degeneracy of $2j+1$. This is termed attractive because experimental observations have revealed that $j = l - 1/2$ levels are higher in energy than the corresponding $j = l + 1/2$ levels. Sometimes,

a level becomes so much lower in energy such that it "intrudes" into the lower shell and these are called "intruder" states. This becomes more relevant when the nuclei become deformed, and in regions close to the drip lines.

The Woods-Saxon potential is a better model to explain the mean field as it also converges to zero when the distance of the nucleon from the rest of the nucleons becomes large. It is given by,

$$V(r) = \frac{V_0}{1 + \exp\left(\frac{r-R}{a}\right)}, \tag{1.4}$$

where r is the radial distance, V_0 is the depth of the potential, which is of the order of -50 MeV, radius, $R = 1.27A^{1/3}$, where A is the atomic mass, and a is the diffuseness, which has a value generally between 0.6 fm and 0.8 fm. As shown in Figure 1.2, even the Woods-Saxon potential (Intermediate form) alone cannot reproduce the experimentally observed shell closures and the coupling term is always necessary.

Although the NSM is successful in explaining the shell gaps, sometimes, even in the region of closed shells, it cannot explain the nuclei adequately. A full picture of the nucleus is required in such cases, but a nucleus of mass number 'A' has 'A' strongly interacting nucleons, and solving the full Hamiltonian for such a nucleus will be a very hard problem. Hence, modifications are required for shell model calculations to account for different interactions between the nucleons. One such method that we are interested in is called the shell model configuration mixing (SCM). The calculation assumes a shell model space with a valence space and a residual space. The nucleons are allowed to move in this shell-model space following the various conservation laws. Then, the effect of a certain number of particle-hole excitations from the residual space on the valence space is studied. For SCM calculations, the ground state configuration of a nucleus is considered to be at $0\hbar\omega$ and n particle-n hole excitations are labeled as $n\hbar\omega$ [13].

1.2 Deformed Shell Model

The nuclear shell model performs well in explaining closed shell or nearly-closed shell nuclei. But as the proton-neutron ratio become unbalanced or as the mass number increases, the shape of the nuclei starts to change or deform. The independent particle model works in

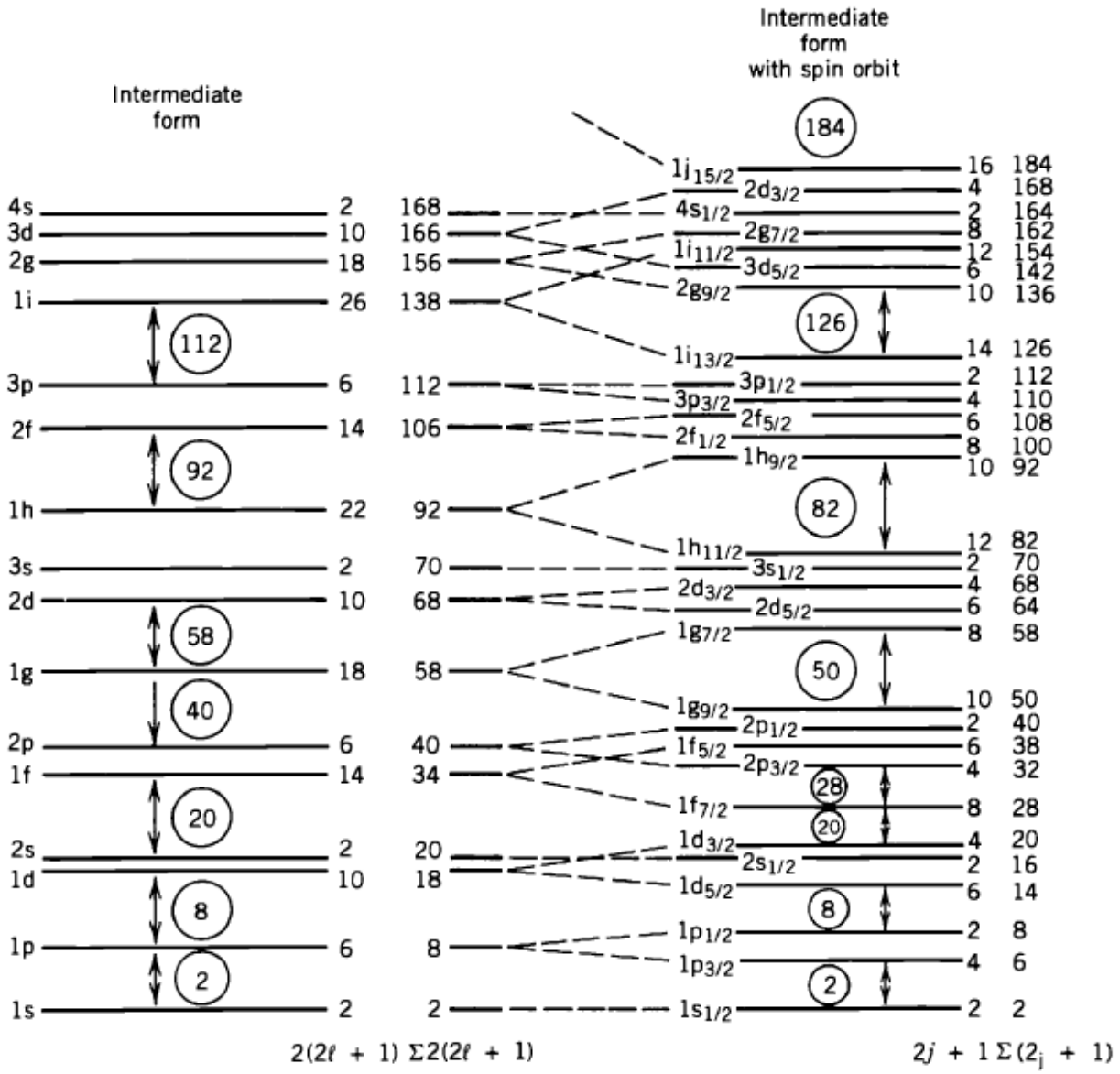

Figure 1.2: Nuclear Shell Model, adapted from [16]. The intermediate form is obtained using the Woods-Saxon potential. After adding the spin-orbit term, it can be seen that the experimentally observed magic numbers are reproduced.

this scenario but a deformed single-particle potential is required in such cases. Deformations in nuclei have been evident from experimental observations and some of the existence of rotational bands resulting from the collective rotation of the nucleus [14], large quadrupole moments in nuclei far from spherical closed shells, single-particle spectra unexplained by the spherical shell model [15].

To explain the deformed shell model, one could use the anisotropic harmonic potential. Assuming an ellipsoid distribution of nuclear matter, the Hamiltonian for a single particle can be written as

$$H = -\frac{\hbar^2}{2m}\nabla^2 + \frac{1}{2}m(\omega_x^2 x^2 + \omega_y^2 y^2 + \omega_z^2 z^2), \tag{1.5}$$

where, $\omega_i (i = x, y, z)$ satisfy, $\omega_i = \omega \frac{R}{a_i}$, and $\omega_x \omega_y \omega_z = \omega^3$.

In this study, we are only considering axially symmetric quadrupole deformations, and generally, for prolate and oblate deformations, the symmetry axis is taken as the z-axis, and $\omega_x = \omega_y$. Following these assumptions, the surface of the nucleus can be parametrized by describing the radius vector as,

$$R(\theta, \phi) = R_0[1 + \beta_2 Y_{20}(\theta, \phi)]. \tag{1.6}$$

Here, β_2 is the deformation parameter and it is related to the average radius of the nucleus, R_{av} by the following relation,

$$\beta_2 = \frac{4}{3}\sqrt{\frac{\pi}{5}}\frac{\Delta R}{R_{av}}, \tag{1.7}$$

where, ΔR is the difference between the semi-major and semi-minor axes of the ellipsoid. Positive, zero, and negative values of β_2 correspond to prolate, spherical and oblate shapes, respectively. Larger values of β_2 denote larger quadrupole deformations. Sometimes, the deformation parameter is also written in terms of quadrupole deformation parameter ϵ_2. To first order, ϵ_2 and β_2 are related as [15],

$$\beta_2 \approx \frac{1}{3}\sqrt{\frac{16\pi}{5}}\epsilon_2 = 1.057\epsilon_2. \tag{1.8}$$

1.2.1 Nilsson Model

In 1955, Nilsson performed deformed shell model calculations using anisotropic potentials [17]. Since it is a non-spherical potential, the angular momentum quantum number, l, and the intrinsic spin s are not good quantum numbers anymore. The states calculated from the Schrödinger equation will have a mixture of different l values but with the same parity. The level energies are no longer determined by the j value but are dependent on the spatial orientation of the orbit, or in other words on the projection of the total angular momentum on the symmetry axis. The projection of j along the symmetry axis is denoted as Ω, and $\Omega = +\Sigma$, where, Λ and Σ are the projections of the orbital angular momentum and the nuclear spin respectively. In axially symmetric nuclei, $+\Omega$ and $-\Omega$ levels have the same energy because of the symmetry along the reflection axis. For example, the previously degenerate $d_{5/2}$ orbital, which can have six components state will split into 3 states in the deformed shell model ($\Omega = 1/2, 3/2, 5/2$). In the case of prolate deformations, the orbit with the smallest Ω is more tightly bound and interacts more strongly with the core, and is the lowest in energy but for oblate shapes, the orbit with the largest Ω has the lowest energy and largest interaction with the core.

The Nilsson levels are denoted as $\Omega[Nn_z\Lambda]$, where, N is the oscillator shell quantum number and n_z is the projection of N along the symmetry axis. Similar to the spherical shell model, a more realistic potential is required to explain nuclear systems. The Woods-Saxon potential in the Nilsson model is given as [15],

$$V_{WS}(r,\theta,\phi) = -V_0 \left[1 + \exp\left(\frac{r - R(\theta,\phi)}{a(\theta,\phi)}\right)\right]^{-1}. \tag{1.9}$$

and the spin-orbit coupling term required for the deformed shell model is given as,

$$V_{SO}(r,\theta,\phi) = -\lambda_{SO}\left[-\frac{\hbar}{2mc}\right]^2 (\nabla V_{WS} \times p)\sigma. \tag{1.10}$$

Nilsson model calculated using Woods-Saxon potential including the spin-orbit term, for neutron levels in nuclei with mass number, $A \leq 50$ is given in Figure 1.3. Here, it can be

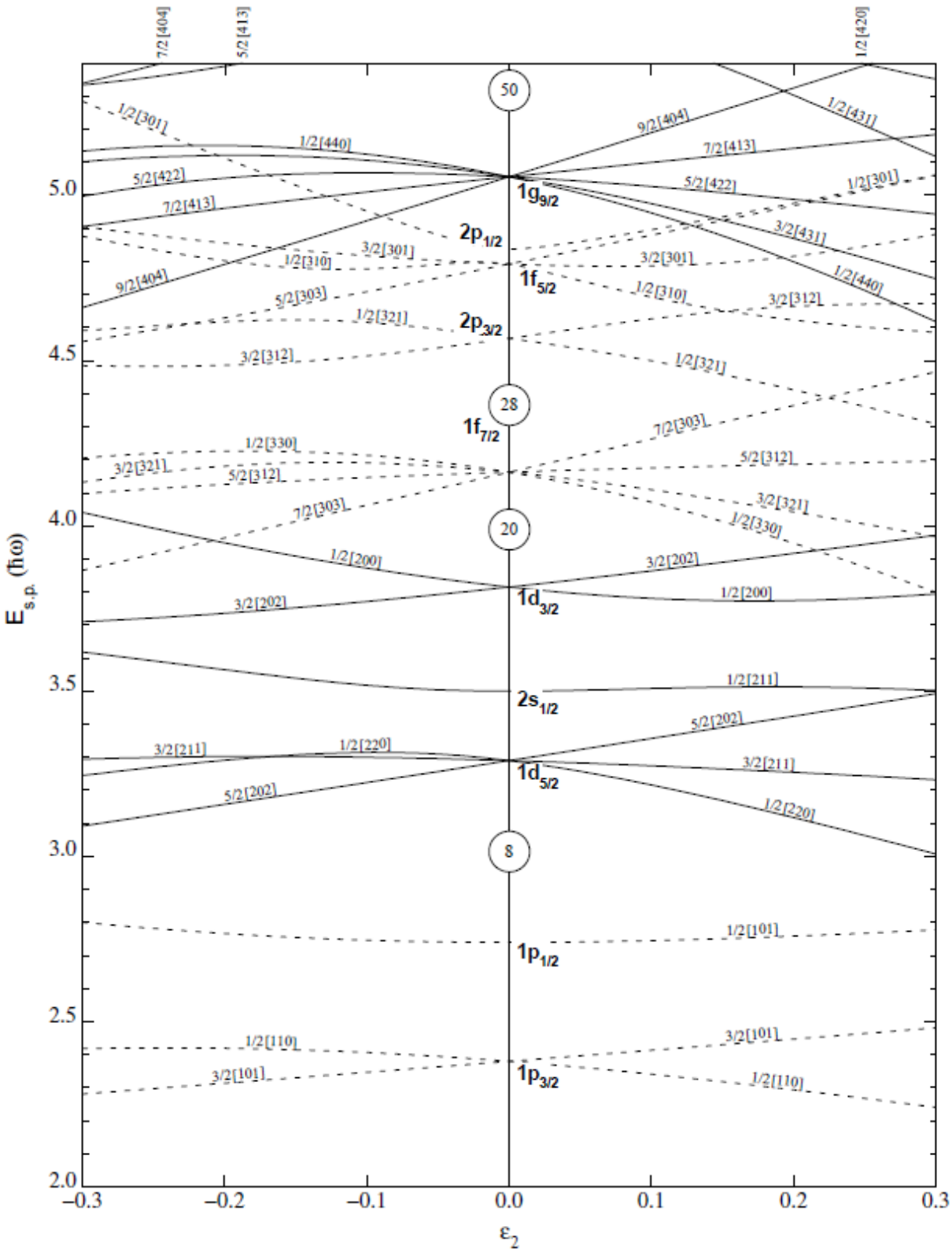

Figure 1.3: Nilsson Model for neutron levels in nuclei with $A \leq 50$, adapted from [18]. The spherical magic numbers are shown at zero deformation. As the deformation increases, the magic numbers start to evolve.

seen that the spherical magic numbers evolve when there is deformation in the shape of the nuclei. As it was noted earlier, each Nilsson level has a degeneracy of two.

1.3 Halo Nuclei

Some of the most studied halo nuclei are ^{6}He, ^{11}Li, and ^{11}Be for neutron halos and ^{8}B, ^{13}N, and ^{17}Ne for proton halos. Neutron halos are more spatially extended compared to proton halos because of the confining Coulomb barrier of the latter. For example, ^{11}Li has a larger halo than ^{8}B. The valence proton in ^{8}B is in a p orbital, which creates a centrifugal barrier as well. A typical neutron halo nucleus has at least a 50% probability of finding the halo neutron outside the core potential range. The Shell Model is not very useful in explaining these light halo nuclei because of the diffuse nature of the nucleus. However, it was able to explain some of the features by treating these nuclei as an inert core and valence nucleons.

Halo nuclei are found near the drip-lines of the nuclear chart owing to the weak binding of the abundant valence nucleons. Neutron halos form when a neutron tunnel out of the nuclear core because of its very weak binding energy. One of the most famous halo nuclei is ^{11}Li. It has a root-mean-square matter radius comparable to that of ^{40}Ca, and the total extent of the halo neutrons is similar to that of outermost neutrons in ^{208}Pb, albeit being much lighter and having about 20 times fewer nucleons than the latter [19]. It is a two-neutron halo and the probability density of the last two neutrons continues to around 6 fm from the center. Figure 1.4a shows some of the reported halo nuclei.

Another interesting kind of nuclei is Borromean nuclei. These are mostly two-nucleon halos. A Borromean system is a bound system that consists of three bodies in which the two-body subsystems are unbound. For example, ^{14}Be is a Borromean nucleus and it is bound, but its two-body subsystems, ^{13}Be and the dineutron are unbound. Some other common Borromean two-neutron halos are ^{6}He, ^{8}He, and ^{17}B.

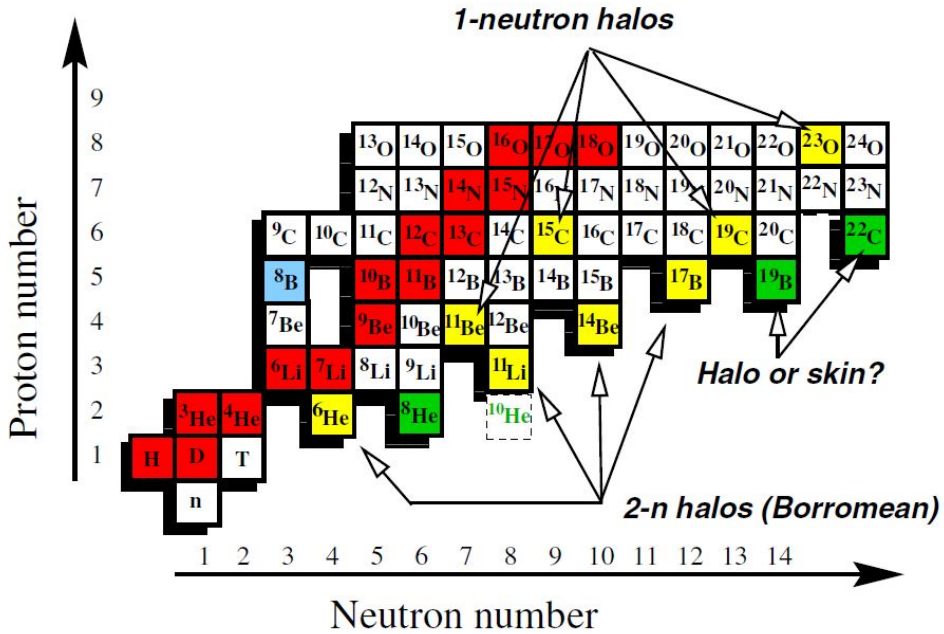

(a) Portion of the nuclei chart with halo nuclei, adapted from [21]. The red squares how the stable nuclei. The yellow squares depict neutron halo nuclei. The green squares display halo or skin nuclei. The blue square shows a proton halo nucleus.

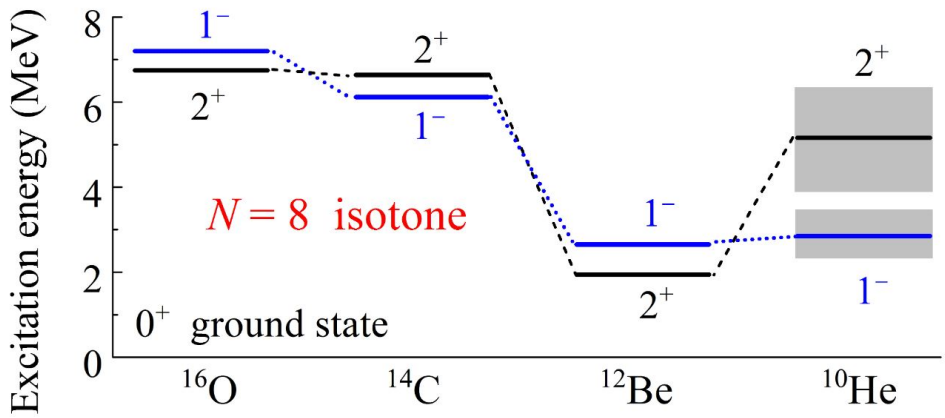

(b) Inversion of the $\nu p_{1/2}$ and $\nu s_{1/2}$ levels in N=8 isotones. Figure adapted from [22]

Figure 1.4: Figures showing some of the exotic phenomena in nuclei as the neutron to proton ratio changes.

1.4 Inversion of Levels

A feature found in the shell model as we move away from stability is that the shell gaps begin to evolve and disappear and new shell gaps begin to appear. This is thought to be because of the shifts in the single-particle energies due to the interactions between the valence protons and neutrons [20]. Some known shell breakdowns are at N = 8, 14, 20, 28, and 40. In Figure 1.4b, the case of the N = 8 shell gap breakdown is shown. We can see that there is an inversion in the neutron energy levels $\nu p_{1/2}$ and $\nu s_{1/2}$ of ^{12}Be. To study these shell gap breaking, theorists need to have access to spectroscopic data for the isotopes in these regions.

1.5 Previous studies of ^{13}Be

Beryllium isotopes show a variety of structural phenomena such as alpha clustering in ^{8}Be [23], molecular structure in ^{10}Be [24], a one-neutron halo in ^{11}Be [25], and two-neutron Borromean halo in ^{14}Be [26, 27]. These properties make the isotopic chain intriguing for structural studies. Although, various experiments and theoretical calculations were performed in the past to study the structure of ^{13}Be, very little is known about this neutron unbound nucleus.

^{13}Be is a subsystem of the Borromean nucleus ^{14}Be and the continuum structures of the former are essential for understanding the two-neutron halo nucleus. It is one neutron away from the N=8 shell closure and the instability of ^{13}Be might be due to the shell gap breakdown at N=8 for neutron-rich nuclei. Since it is near the neutron drip-line, this nucleus can give us more insights into the influence of the continuum [28].

We will go through some of the results obtained from shell-model configuration mixing calculations in the $0p-1s0d$ model space, used by different groups, to study the structure of ^{13}Be, over the years. On applying the $(0+1)\hbar\omega$ shell-model calculations, Poppelier et al. [29] predicted a $1/2^-$ ground state at 1.16 MeV above the neutron threshold and a $5/2^+$state close to it. Using mean field theory with a Woods-Saxon potential, Lenske et al. [30] calculated a $1/2^+$ state at 0.9 MeV above the one-neutron threshold. On employing $(0-3)\hbar\omega$ shell-model

calculations, Fortune [31] predicted a $5/2^+$ state at 1.39 MeV above the $1/2^+$ ground state. Here, mixing between the 0 and $2\hbar\omega$, and the 1 and $3\hbar\omega$ shell configurations were taken into account [32]. In a recent study, within the Nilsson model, Macchiavelli et al. [33], predicted a $5/2^+$-state at around 1.8 MeV above the threshold. Therefore, we can see that these predictions cannot definitively determine the energy and ordering of the low-lying states. A detailed list is given in Table 1.1.

If we look at the experimental side of ^{13}Be, things are not very different. Despite a significant number of experiments over three decades, there are discrepancies between these measurements. The first observation of an unbound resonance close to 1.8 MeV above the ^{12}Be+n threshold was reported by Aleksandrov et al. [34]. Belozyorov et al. [35] in 1998 also observed a weakly populated state at 0.80(9) MeV above the threshold in the ^{14}C(^{11}B,^{12}N)^{13}Be reaction. Ostrowski et al. [30] measured a resonance at 2.01 MeV above the neutron threshold.

Some of the recent experiments performed are knockout reactions from ^{14}Be using a carbon target by Simon et al. at GSI [36], using a liquid hydrogen target by Kondo et al. at RIKEN [37] and Aksyutina et al. at GSI [38], and breakup on a carbon target of ^{14,15}B at 35 MeV/u by Randisi et al. at GANIL [32]. The most recent measurement on ^{13}Be was carried out by Corsi et al. [39] and they observed states at 0.43 MeV, 2.3 MeV, and two states above that. Table 1.2 lists the interpretations of these previous experimental measurements in terms of combinations of resonances and virtual states. Meaningful comparisons can be made by observing strengths at similar ranges of energies. The strengths from those closest to the threshold, including low-lying resonances and virtual states, up to close to 2 MeV above the threshold are shown here. Strength 1a represents the lowest reported resonance or a virtual s-wave state, 1b represents the next highest-lying resonance, and 2 represents resonance around 2 MeV.

Mostly these theoretical predictions and experiments agree on a resonant state around 2 MeV above the neutron threshold, but the energies and ordering of states below this resonance are less certain. The best way to study the low-lying structure is to perform a (d, p) reaction on ^{12}Be at a low beam energy because that will help us understand the single-particle properties of ^{13}Be.

Table 1.1: Some of the previously performed theoretical calculations to study the structure of ^{13}Be. Only the first three low-lying states for each calculation are shown here. These were shell model calculations.

Author (year)	Energy above the threshold (MeV)		
	Strength 1	Strength 2	Strength 3
Poppelier et al. (1983) [29]	$1.16(\frac{1}{2}^-)$	$1.21(\frac{5}{2}^+)$	$2.44(\frac{5}{2}^-)$
Lenske et al. (1992) [30]	$0.9(\frac{1}{2}^+)$	$2.3(\frac{3}{2}^-)$	$2.45(\frac{5}{2}^+)$
H. T. Fortune (2014) [32]	$0.4(\frac{1}{2}^+)$	$1.79(\frac{5}{2}^+)$	$2.7(\frac{5}{2}^+)$
Macchiavelli et al. (2018) [33]	$x(\frac{1}{2}^+)$[a]	-	$1.8 + x(\frac{5}{2}^+)$

[a] x is the threshold energy

Table 1.2: Some of the previously performed measurements to study the structure of ^{13}Be. Only the low-lying states, up to 2 MeV above the threshold are shown here. Strength 1a represents the lowest reported resonance or a virtual s-wave state, 1b represents the next highest-lying resonance, and 2 represents resonance around 2 MeV. E_r denotes the energy in the case of a resonance, and a_s is the scattering length in the case of a virtual s-wave state.

Author (year)	Reaction	E_r (MeV) or a_s (fm)		
		Strength 1a	Strength 1b	Strength 2
Aleksandrov et al. (1983) [34]	^{14}C(^{7}Li,^{8}B)	-	-	1.8
Ostrowski et al. (1992) [30]	^{13}C(^{14}C,^{14}O)	-	-	2.01($\frac{5}{2}^+$ or $\frac{1}{2}^-$)
Korsheninnikov et al. (1995) [40]	^{12}Be(d,p)	-	-	2.0
Von Oertzen et al. (1995) [41]	^{13}C(^{14}C,^{14}O)	-	-	2.01($\frac{5}{2}^+$)
Belozyorov et al. (1998) [35]	^{14}C(^{11}B,^{12}N)	-	0.80($\frac{1}{2}$)	2.02($\frac{5}{2}^+$)
Thoenessen et al. (2000) [42]	^{9}Be+^{18}O	0.20($\frac{1}{2}^+$)	-	-
Simon et al. (2007) [36]	Knockout	-3.2	-	2.00($\frac{5}{2}^+$)
Kondo et al. (2010) [37]	Knockout	-3.4	0.51($\frac{1}{2}^-$)	2.39($\frac{5}{2}^+$)
Aksyutina et al. (2013) [38]	Knockout	0.46($\frac{1}{2}^+$)	-	1.95($\frac{5}{2}^+$)
Randisi et al. (2014) [32]	Dislocation	0.40($\frac{1}{2}^+$)	0.85($\frac{5}{2}^+$)	2.35($\frac{5}{2}^+$)
Ribeiro et al. (2018) [43]	Dislocation	0.44($\frac{1}{2}^-$)	0.86($\frac{1}{2}^+$)	2.11($\frac{5}{2}^+$)
Corsi et al. (2019) [39]	^{14}Be(p,pn)	-9.2	0.48($\frac{1}{2}^-$)	2.30($\frac{5}{2}^+$)

Chapter 2

Theoretical Background

The size of a nucleus is of the order of 10^{-15} meters. So, in order to probe the nuclear structure, that is to know the proton and neutron energy levels, its ordering of a nucleus, we need appropriate tools to delve into this energy regime (in the MeV range). One of the ways, in which we can do this is by using nuclear reactions. In this chapter, we will see the basic principles of a two-body nuclear reaction and reaction kinematics.

2.1 Nuclear Reactions

Nuclear reactions play an important role in the study of nuclear structure. During a reaction, the participating nuclei exchange energy, or nucleons, or both and this can be used to measure the binding energy and the excitation energies of the nucleus and give access to the nature of the states populated. Nuclear reactions are also utilized to study different nucleosynthesis processes in cosmic sources such as stars and supernovae which leads to the formation of new elements. A nuclear reaction can give rise to new products when two nuclei collide with each other if there is sufficient energy. A typical nuclear reaction can be written in the following form:

$$\mathrm{a} + \mathrm{X} \longrightarrow \mathrm{b} + \mathrm{Y}, \tag{2.1}$$

where a is the beam, X is the target (usually at rest in the lab frame), b is the ejectile and Y is the recoil. In shorthand, the reaction can be written as X(a,b)Y.

The products of the reaction can be the same as the reactants with only a difference in the kinetic energy like in, ${}^{12}_{6}\mathrm{C} + {}^{107}_{47}\mathrm{Ag} \longrightarrow {}^{12}_{6}\mathrm{C} + {}^{107}_{47}\mathrm{Ag}$ and it depends on the incident energy. Two situations can arise in this case: 1) Energy is transferred between the reactants and if the products are in the ground state, then it is called an elastic scattering; 2) If some of the energy transferred is used in the excitation of one of the incident particles, it is called inelastic scattering.

There are various conservation laws that govern a nuclear reaction depending on the type of interaction between the particles, and that is determined by the energy of the interacting particles. In a binary reaction with particles interacting through strong force, the energy, spin, and parity of the recoiling particle can be inferred by measuring the energy and the angular distribution of the reaction projectile.

2.1.1 Types of nuclear reactions

There can be different types of reactions depending on the energy of the incident particle, the time scale, and the impact parameter of the reaction. Two main kinds of reactions are compound-nucleus (CN) interactions and direct reactions. These reactions are mainly distinguished based on their timescales. Direct reactions happen rapidly ($10^{-22}s$) compared to CN reactions ($10^{-16} - 10^{-18}s$).

Compound nucleus reaction is a two-step process. In these reactions, the reactants fuse together to form a compound nucleus, which then decomposes into products that may or may not be the same as the incident particles, $\mathrm{a} + \mathrm{X} \longrightarrow \mathrm{C}^* \longrightarrow \mathrm{b} + \mathrm{Y}$. CN reactions usually occur at low incident energy. A low-energy incident nucleon has a higher de Broglie wavelength which will result in it seeing the nucleus as a whole. The lower energy leads to a longer interaction time and this gives the nucleus enough time to reorganize itself which leads to a compound reaction. In a CN reaction, the incident particle may interact with one of the nucleons of the target nucleus which then interact with other nucleons and after multiple interactions, the compound nucleus loses the information on how it was formed. After multiple interactions, one or more nucleons may attain enough energy to evaporate out of the compound nucleus. Due to this, CN reactions are characterized by the energy of the compound nucleus and not the way in which it was formed. Fusion is an example of

CN reaction. Fusion evaporation occurs by equilibration of the compound nucleus through emitting gamma rays and nucleons.

A direct reaction occurs through a single interaction between the projectile and a degree of freedom of the target nucleus. This degree can be either a collective coordinate or a single or few nucleons of a nucleus [44]. Collective coordinates can include oscillations or rotations of nuclei. Direct reactions mostly involve interactions between the incident particle and one or a few valence nucleons of the heavier nucleus. As the energy of the incident particle increases, its wavelength decreases, resulting in nucleon-nucleon interactions. Examples of direct reactions include elastic, inelastic, transfer, knockout, coulomb dissociation reactions, etc. One important aspect of single-particle transfer reactions is its ability to study the low-lying shell model states of nuclei.

There are energies at which both types can happen and that depends on the impact parameter of the reaction, meaning whether it was a direct collision or a glancing one. In between these two extremes, there are resonance reactions in which a quasi-bound state is formed before a particle is ejected from it.

Normal kinematics and inverse kinematics

A reaction is said to be performed in normal kinematics when a light-ion beam impinges on a target consisting of a heavy nucleus. In inverse kinematics, a heavy-ion beam impinges on a target made of a lighter nucleus. Before the arrival of radioactive ion beam (RIB) facilities, direct reactions were carried out in normal kinematics. Light-ion beam accelerators with protons, deuterons, or alpha particles were used. The types of nuclei that could be studied using this technique were limited because targets are necessarily made from stable, or long-lived nuclei. Over the past few decades, RIB facilities became available and made it possible to explore deeper into the neutron- and proton-rich areas of the nuclear chart.

There are some advantages and disadvantages to both methods. In normal kinematics, there is less kinematic compression because the kinematics does not change much as we change the reference frames. The energy and angle of scattering are similar in both laboratory and center of mass frames. In experiments where the heavier recoil needs to be detected, inverse kinematic proves useful. Heavy recoils will be able to escape the target due to

their higher momentum compared to reactions in normal kinematics. The energy-angle systematics of the light-ejectiles in inverse kinematics are less sensitive to the energy and mass of the beam for reactions of a given type. Hence, one method is preferred over the other depending on the experiment requirements.

2.2 Reaction Kinematics

In an experiment, the energy and angle of one, or both of the final products are the main observables. Using conservation of energy, the following relation can be written,

$$m_a c^2 + T_a + m_X c^2 + T_X = m_b^* c^2 + T_b + m_Y^* c^2 + T_Y, \tag{2.2}$$

where the T_is and m_is are the kinetic energies and the rest masses of the respective nuclei as shown in Figure 2.1. $m^* c^2 = mc^2 + E_{ex}$, where E_{ex} is the excitation energy of the recoils. $E_{ex} = 0$ if the recoils are left in the ground state.

For a reaction, the reaction Q-value is defined as the difference in the total masses of the products and the reactants. It is therefore given by,

$$Q = (m_{reactants} - m_{products})c^2 = (m_X + m_a - m_Y^* - m_b^*)c^2. \tag{2.3}$$

This is equal to the excess kinetic energy of the products. Therefore from Eqn. 2.2, we have

$$Q = T_b + T_Y - T_a - T_X. \tag{2.4}$$

Conservation of linear momentum along the directions parallel and perpendicular to the beam gives another two equations. Solving them along with Eqn. 2.2 gives the energy of the lighter particle assuming that the Q-value of the reaction is known. Similarly, we can also find out the Q-value of the reaction by measuring the energy and angles of the emergent light particle. Figure 2.2 shows the energy of the outgoing proton as a function of the angle in a $^{12}\mathrm{C}(\mathrm{d,p})^{13}\mathrm{C}$ reaction. Here, we can see that the ground state and the first three excited states of $^{13}\mathrm{C}$ are populated and we can differentiate these four states by Q-value. This

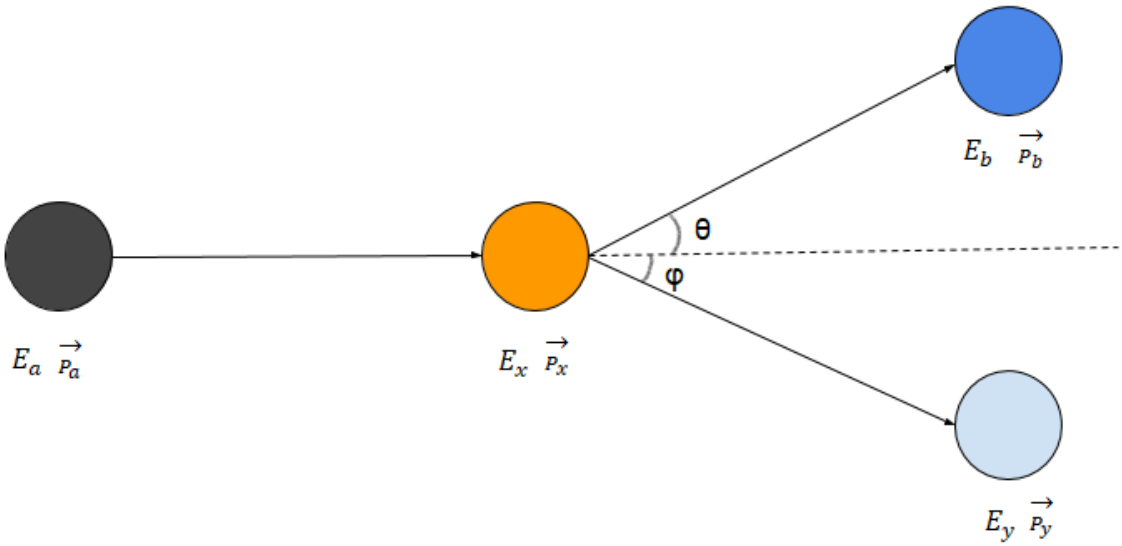

Figure 2.1: Two body reaction

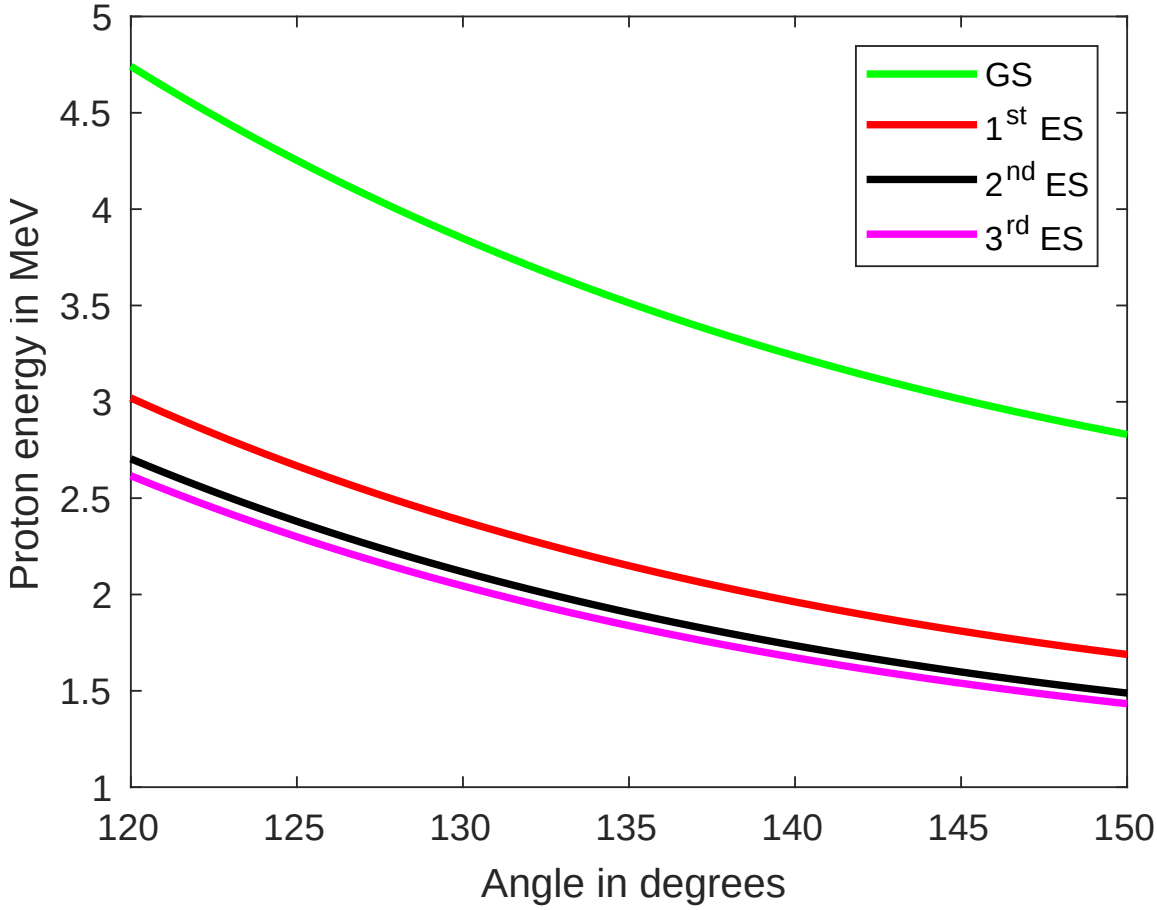

Figure 2.2: The energy of the outgoing proton as a function of the angle in a $^{12}\mathrm{C}(\mathrm{d},\mathrm{p})^{13}\mathrm{C}$ reaction; shows the first four states of $^{13}\mathrm{C}$ being populated in the laboratory frame. Here, 'GS' and 'ES' stand for the ground state and excited state, respectively

method can be used to differentiate between the ejectiles of different reactions as it will be shown in section 3.4

By solving the conservation laws simultaneously, we can obtain the Q-value of a reaction as,

$$Q = T_b\left(1 + \frac{m_b}{m_Y}\right) - T_a\left(1 - \frac{m_a}{m_Y}\right) - 2\left(\frac{m_a}{m_Y}\frac{m_b}{m_Y}T_aT_b\right)^{1/2}\cos\theta. \tag{2.5}$$

In an experiment, if one knows the beam energy (T_a), the masses of the beam (m_a), the projectile (m_b), and the recoil (m_Y), then the energy (T_b) and angle of the projectile (θ) can be measured, thereby obtaining the Q-values of the different states of the recoil nucleus.

2.3 Distorted Wave Born Approximation

One nucleon transfer reactions, which are direct reactions, are an important tool in studying nuclear structure. Reactions like (d,p) neutron transfer, or (d,n) proton transfer is helpful in understanding single-particle states, which in turn are important to test nuclear models. In a reaction process denoted by X(a,b)Y, (a+X) is called the entrance channel, and (Y+b) is called the exit channel. When 'a' and 'X' come in close contact, interacting with each other through a potential V, different exit channels can open up. Direct nuclear reactions can be thought of as a transition happening between two channels. This includes the exchange of energy or nucleons or both and it depends on the energy and structure of the interacting nuclei. The transition amplitude of this interaction can be approximated by the truncated first-order Born approximation.

$$\mathcal{T} = \int e^{-i\vec{k_b}\cdot\vec{r_b}} \langle\psi_Y\psi_b| V |\psi_X\psi_a\rangle e^{i\vec{k_a}\cdot\vec{r_a}} dr_a dr_b, \tag{2.6}$$

where $\vec{k}$ and $\vec{r}$ are the relative momenta and the separation between the centers of the mass for the entrance and the exit channels respectively. The wave functions of the components of the reaction are represented by ψ_i. The interaction term can be written as a multipole series expansion in terms of spherical harmonics.

$$\langle\psi_Y\psi_b| V |\psi_X\psi_a\rangle = \sum_{l,m} f_l(r)Y_{l,m}(\theta,\phi), \tag{2.7}$$

where f_l are the coefficients of the spherical harmonics, $Y_{l,m}(\theta, \phi)$. The l and m dependence in Eqn. 2.7 shows that reactions can uniquely determine the transferred angular momentum for specific states in the nucleus in the exit channel. In the Born approximation, the incoming and outgoing particles were treated as plane waves, but the nuclear interior distorts these waves and plane waves can be modified to be an asymptotic sum of plane waves and incoming and outgoing spherical waves of the form,

$$\chi^{\pm}(\vec{k}, \vec{r}) \rightarrow e^{i\vec{k}\cdot\vec{r}} + f(\theta)\frac{e^{\pm ikr}}{r}. \tag{2.8}$$

Here, $f(\theta)$ is the scattering amplitude due to the potential produced by the nuclear interior and the scattering cross-section is proportional to the square of the scattering amplitude. We will talk about this potential in the next section. χ^+ and χ^- are the distorted waves for the entrance and exit channels respectively and they are treated as a mixture of plane and scattered spherical waves. This is called the distorted wave Born approximation (DWBA).

After modifying Eqn. 2.6, the transition amplitude in the DWBA model can be written as,

$$\mathcal{T}_{DWBA}(\theta, \phi) = \int \chi^-(\vec{k}_b, \vec{r}_b) \langle \psi_Y \psi_b | V | \psi_X \psi_a \rangle \chi^+(\vec{k}_a, \vec{r}_A) d\vec{r}_a d\vec{r}_b. \tag{2.9}$$

When a single nucleon is transferred in the DWBA model, the elastic scattering is assumed to be the dominant channel and the direct reactions can be thought of as perturbations to the elastic scattering. In order to calculate the distorted wave functions and the transition amplitude, the potential between the nuclei needs to be calculated.

2.4 Optical Potentials

An optical potential replaces the interactions between nuclei which is a complex many-body problem. The average field on a particular nucleon due to the rest of the nucleons is represented by a central potential, U. When two nuclei come in contact, they interact through the combined field generated by nucleons in each nucleus before and after the reaction. Thus, U depends only on the relative coordinate between them.

Consider a partition α of two nuclei X and a with internal wave functions ψ_X and ψ_a. Then the wave function of the partition ψ_α can be written as

$$\psi_\alpha(x_\alpha) = \psi_X(x_X)\psi_a(x_a). \tag{2.10}$$

The total wave function for the system can be written as a product of the internal nuclear wave function ψ_α and a relative wave function χ_α,

$$\Psi = \chi_\alpha(\mathbf{r}_\alpha)\psi_\alpha(x_\alpha). \tag{2.11}$$

χ_α depends only on the relative coordinates. The Schrödinger equation for partition α with a and X interacting through the central potential U_α is given by,

$$(H_\alpha + T_\alpha + U_\alpha - E)\Psi = 0, \tag{2.12}$$

where, H_α is the internal Hamiltonian of the nuclei a and X, and T_α is the kinetic energy of their relative motion. The Schrödinger equation is separable into the nuclear coordinates and the relative coordinates and hence for this particular partition α, the following simplification can be done,

$$(T_\alpha + U_\alpha - E_\chi)\chi_\alpha(\mathbf{r}_\alpha) = 0. \tag{2.13}$$

Since U depends only on the relative coordinates, it cannot produce any change in the internal structure of the nuclei and hence describes elastic scattering.

When two nuclei collide, if the bombarding energy is low, most of the cross-section will be due to elastic scattering but as the bombarding energy increases inelastic and reaction channels open.

Thus direct reactions can be explained by a simple model where the average interaction between a nucleus and a nucleon can be considered as a shallow absorbing potential well. This is similar to the case of a photon scattering off of a hard-sphere and hence the name Optical Model. In order to account for the removal of flux, we need U to be complex, with the real part describing scattering and the imaginary part describing absorption (present in

reactions).

$$U(r) = V(r) + iW(r) \tag{2.14}$$

The real and the imaginary terms have radial dependence. Optical potentials have volume, surface, and spin-orbit terms and each of these terms can have real as well as imaginary parts. The volume term of the nuclear potential is usually of the form of Woods-Saxon. The surface potential term leads to an interaction between the valence nucleons, and therefore the derivative of the Wood-Saxon is assumed to describe the surface terms. To account for the spin-orbit force, an $\vec{L} \cdot \vec{\sigma}$ interaction term is also included in the potential. And a Coulomb term is required if the projectile of the reaction is a charged particle. A commonly used form of the optical potential is given as,

$$\begin{aligned} U(r) = &- V_v f(r, R_v, a_v) - iW_v f(r, R_w, a_w) \\ &+ 4ia_w W_s \frac{df}{dr}(r, R_w, a_w) \\ &+ 2(V_{SO} + iW_{SO}) \left(\frac{1}{r}\frac{df}{dr}(r, R_{SO}, a_{SO}) \vec{L} \cdot \vec{\sigma} \right) + V_c, \end{aligned} \tag{2.15}$$

where,

$$f(r, R, a) = \frac{1}{1 + \exp((r - R)/A)}. \tag{2.16}$$

Here R and a are the radius and diffuseness parameters of the potential, respectively. The term V is the real part and W is the imaginary part of the potential. The subscripts v, s and SO stand for the volume, surface, and the spin-orbit terms, respectively. $\vec{L}$ is the angular momentum V_c is the coulomb potential term.

The optical model parameters are determined by comparison to elastic scattering data for a nucleus by nucleus basis. This is carried out by fitting angular distributions to large amounts of scattering data obtained for nuclei over a wide mass range at different energy ranges. Such potentials are called global optical model potentials.

2.4.1 Deuteron global optical potentials for (d,p) entrance channel

A deuteron global optical model potential is used in DWBA calculations to study interactions between a deuteron and a nucleus. Hence, it can be used as entrance channel potential in

(d,p) reactions. The potentials used in this work are Perey-Perey [45], Daehnick [46], and Lohr-Haeberli [47]. The parameters of these potentials are available from the code FRONT [48].

The Perey-Perey potential is usually used for nuclei with atomic numbers greater than 12 and deuteron energies in the range of 12 MeV to 25 MeV. The Daehnick potential can be used for a wider range of deuteron energies, from 11.8 MeV to 90 MeV, and nuclei in the mass range of 27 to 238. The Lohr-Haeberli potential works for a narrower range of deuteron energies from 8 MeV to 13 MeV and for nuclei with mass numbers greater than 40. The Perey-Perey potential differs from the other two potentials in not having a spin-orbit coupling term. All the three potentials have volume and surface terms.

2.4.2 Nucleon-nucleus optical potentials for (d,p) exit channel

Nucleon-nucleus global optical potentials provide scattering potential parameterizations for both neutrons and protons as a function of atomic and mass numbers, and the bombarding energy. Therefore, this potential can be used as the exit channel potential for (d,p) reactions. Some of the common nucleon-nucleus potentials are Chapel-Hill 89 (CH89) [49] and Koning-Delaroche (KD) [50]. The CH89 potential was developed by R. L. Varner et. al. by the parametrization of scattering data obtained from nuclei ranging from A = 40 to 209, proton energies from 16 to 65 MeV, and neutron energies from 10 to 26 MeV. It is based on the understanding of the many-nucleon problem and the folding-model potential for finite nuclei. The KD potential covers a much more exhaustive range of proton and neutron energies from 1 keV to 200 MeV scattering on nuclei with mass numbers from A = 24 to 209. These potentials were built based on a comprehensive database of angular distributions of proton and neutron differential cross sections and hence they are very useful. The KD potential has both real and imaginary spin-orbit coupling terms.

In the analysis of ^{12}Be(d,p)^{13}Be, we have used all of the three deuteron global optical potentials and KD nucleon-nucleus potential to fit the angular distribution of the protons emitted from the reaction.

Chapter 3

Experimental Setup

The experimental setup and the techniques used to conduct the ^{12}Be(d,p)^{13}Be transfer reaction are described as well as the various stages of the measurement and the detectors used.

3.1 ISAC: Isotope Separator and Accelerator

Recently, there has been a huge interest worldwide in studying the properties of nuclei far from stability. Nuclei exhibit anomalous behavior, including ordering of nuclear orbitals, which deviate from the conventional nuclear shell model scheme, as we move away from the valley of stability. Some exotic nuclei also have astrophysical implications, like studying the reaction rates of different nucleosynthesis processes. There are different facilities across the world that produce radioactive ion beams (RIB) to conduct experiments for studying the properties of exotic nuclei. The ISAC (Isotope Separator and Accelerator) facility at TRIUMF uses the ISOL (Isotope Separator Online) technique to produce RIBs. Energetic protons accelerated to 500 MeV using the TRIUMF cyclotron, bombard a SiC target, placed at the target station, to produce a large number of radioactive isotopes as shown in Figure 3.1. These are then separated according to the mass-over-charge (A/Q) ratio using the mass separator. There are three main stages of acceleration of these isotopes and the final energy depends on the A/Q ratio. The first and second stages happen in ISAC I raising the energy from 2.04 keV/u to 150 keV/u, then further accelerating the beam to a maximum of 1.3

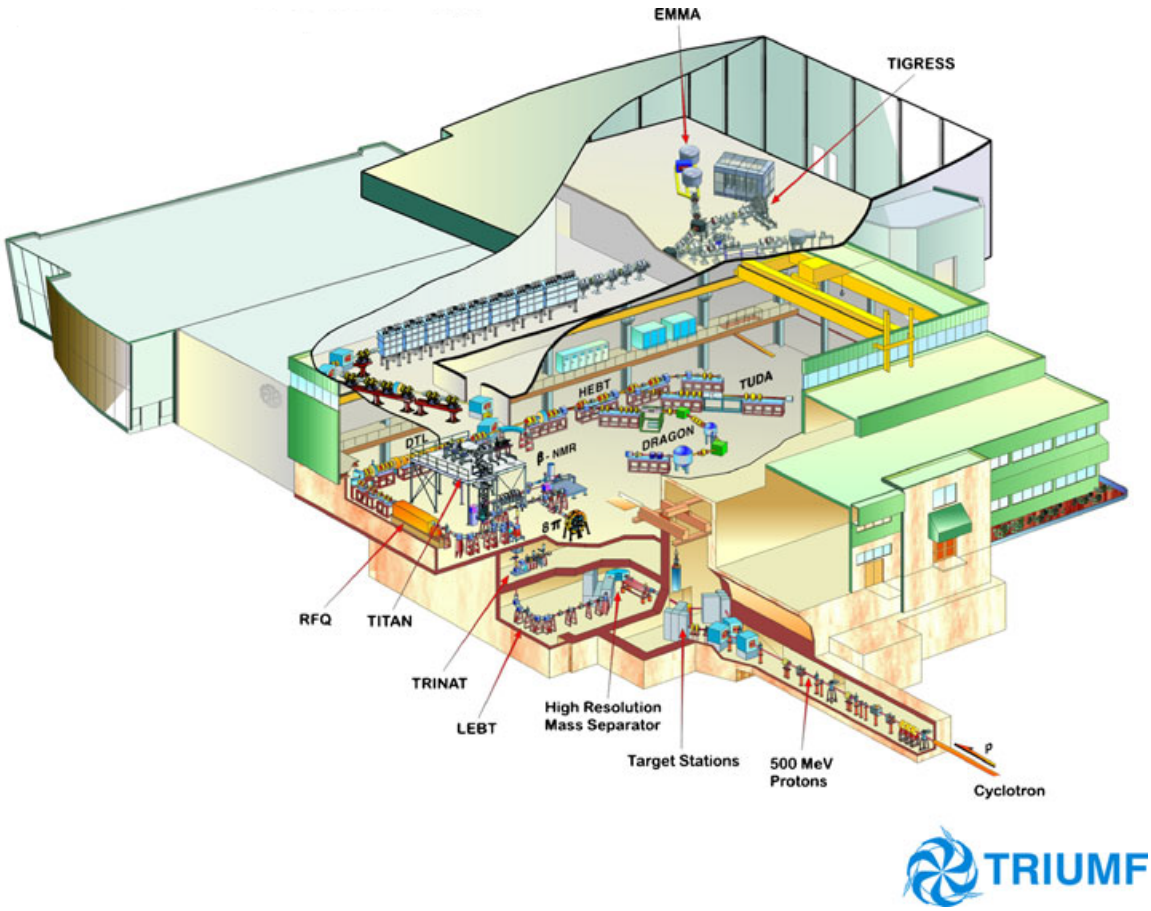

Figure 3.1: Schematic of ISAC

MeV/u to 1.9 MeV/u depending on the A/Q ratio, with a drift tube linac. The third and final stage happens in ISAC II where it is accelerated up to 16.5 MeV/u for an A/Q ratio of 2 [51].

3.2 IRIS: The ISAC charged particle reaction spectroscopy station

Located in the ISAC II experimental area, the IRIS facility was designed for direct reaction studies and inelastic scattering of RIBs, mainly isotopes with large neutron to proton ratios [52]. The aim of this facility is to perform reactions of rare isotope beams with a solid H_2 or D_2 target and to detect the energy and angle of the charged particle reaction products. The major components of the facility are the ionization chamber (IC), a solid deuterium target, and the charged particle detectors. The IRIS system will be described in the following subsections in the order they appear on the beamline. A schematic diagram of the IRIS facility is given in Figure 3.2a.

3.2.1 Ionization chamber

The beam of interest generated by ISAC may have contaminants in it depending on the beam species. In that situation, an ionization chamber (IC) can be used to isolate the required beam from isobaric contaminants before it hits the target, by comparing the energy lost passing through the gas in the chamber. This is most important for medium and heavy nuclear species because it is difficult to accelerate those as pure beams. The IC is filled with isobutane at low pressure, around 19.5 Torr, and is located upstream of the reaction target. The windows of the chamber are made of 50 nm thick silicon nitride foils with dimensions of 10 mm x 10 mm, to isolate the gas volume from the vacuum [52]. These thin windows and the low-pressure gas help to deliver the beam to the target with minimal energy loss and straggling effects. It has a field cage that creates an electric field gradient from the cathode to the anode (Figure 3.2b). This negatively charged cage is made of metal strips that run around the perimeter of the chamber and creates an electric field gradient in the IC that

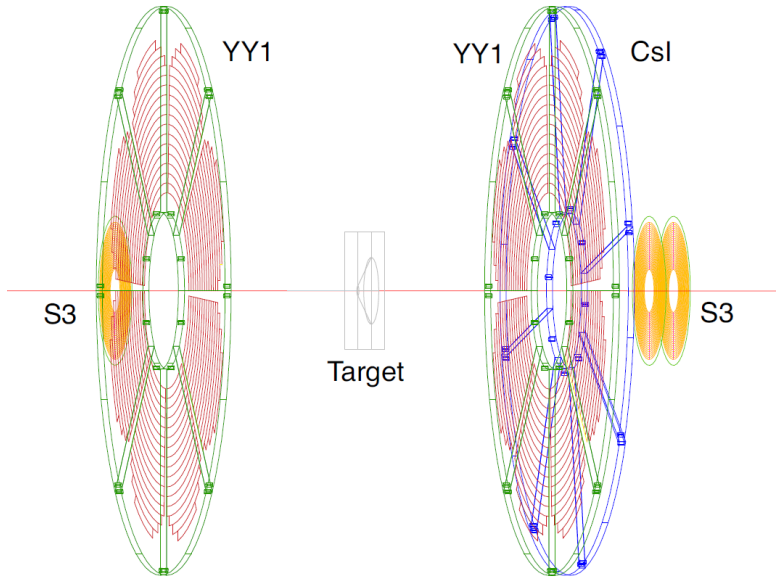

(a) A CAD drawing of the experiment setup at IRIS

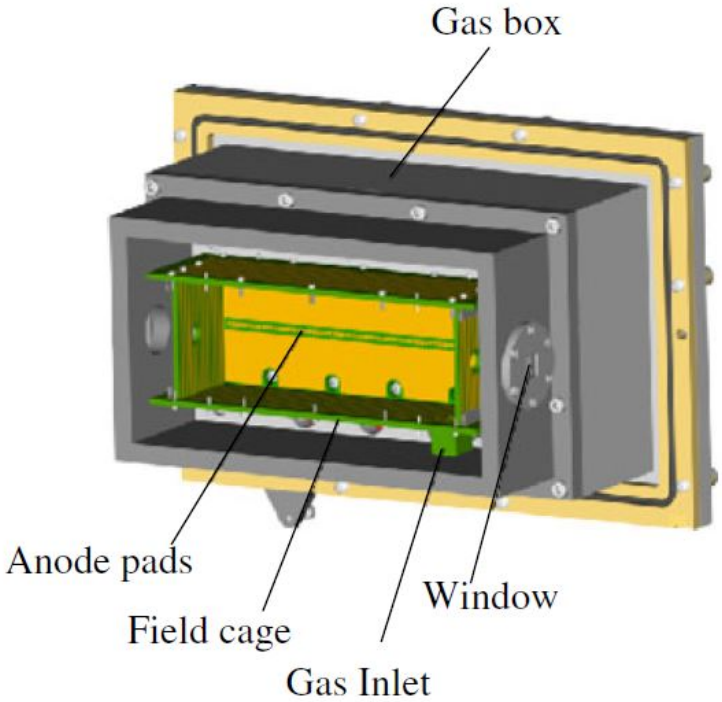

(b) A schematic of the IC [52]

Figure 3.2: Schematics of the experiment setup and the ionization chamber

causes the electrons to drift in the direction of the anode strip. There are eleven segmented metallic strips that run from the cathode to the co-planar anode. The cathode is at a negative potential with respect to the anode. This voltage is fed through each subsequent level of the field cage through a series of resistors and hence the gradient in the electric field with decreasing negative potential nearing the anode. This helps in the transverse drift of electrons. The electrons are then concentrated on the anode strip at the center by the electric field created by the co-planar anodes. Nuclear species with a similar A/Z ratio to that of the beam of interest can pass through the ISAC mass separator which needs to be identified using the IC during the data analysis.

3.2.2 Solid D_2 target

The innovative feature at the center of IRIS is the solid D_2 target. A solid D_2 target has advantages over conventional targets like deuterated polyethylene (C_2D_4) such as a higher density of D_2 atoms without the associated energy loss due to the carbon for a given thickness, offering a better reaction yield without compromising on the resolution. This helps in performing reactions with low-intensity beams of exotic nuclei. Also, the solid D_2 target does not give rise to a scattering or fusion evaporation background from carbon.

The target assembly is shown in Figure 3.3. There is a copper target cell that has a hole of 5 mm in diameter enclosed by a heat shield made of copper and is maintained at a temperature of 30 K by connecting to a cryocooler with a helium compressor. The use of this heat shield is to minimize the radiative heating of the target. The solid target is backed by a thin silver foil which has a thickness of 5.4 μm. The foil is cooled to a temperature of approximately 4K. After the target cell and the heat shield have attained stable temperatures, gaseous deuterium is sprayed onto the silver foil using a diffuser to form the solid D_2 target. The gas flows smoothly through the fine porous surface of the diffuser allowing its deposition diameter to be similar to that of the diffuser itself, which is around 16 mm.

The typical target thickness varies from 40-60 μm and is controlled by the volume of the gas injected into the system [52]. The required volume for a particular thickness can be calculated given the diameter of the target. The diffuser is retracted back after the target

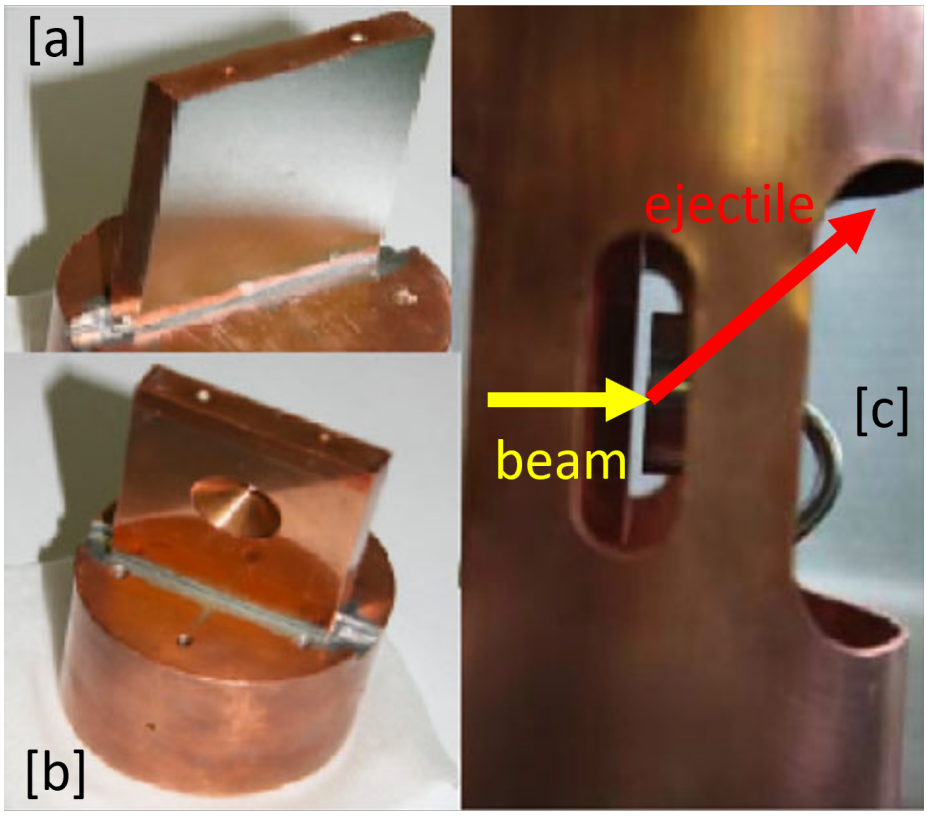

Figure 3.3: Target assembly picture adapted from [52]. [a] shows the silver backing foil. [b] shows the solid hydrogen target cell. [c] is a view of the heat shield. A cartoon of the beam and ejectile is shown using yellow and red arrows, respectively.

is formed. The incoming beam interacts with the target and reactions can occur within the entire thickness of the target depending on the beam energy, reaction Q-value, etc., giving rise to reaction products that travel through the remaining part of the target or go backwards through the part of the target traversed by the beam, before being detected. Any possible fusion-evaporation background due to reactions on the silver foil can be measured by impinging the beam on the silver foil. Later, we will see that for the reaction of interest, there was no background from fusion-evaporation reactions in the laboratory angles measured.

3.2.3 Charged particle detectors

The principal aim of IRIS is to detect the charged particles generated from a reaction on the solid target. Two different sets of detectors detect the light emergent particles and the heavy recoils. The light target-like particles are identified using silicon strip detectors of YY1 type by MICRON Semiconductors. The YY1 detector is divided into sixteen rings (Figure 3.4) and it covers an angle of 45° in azimuthal angle. Hence, an array of eight of these independent azimuthal sectors forms a complete circle. The YY1 detector array is annular in geometry with an inner radius of 50 mm and an outer radius of 129 mm. Hence each ring has a width of 4.9375 mm and subtends a range of different angles with respect to the target depending on the distance from the target center. There were two YY1 detector arrays and each one had a total of $8 \times 16 = 128$ signals which were readout. Of the two arrays, one is upstream of the target, referred to as YU (YY1 upstream) to detect the backward scattered low energy particles and the other one is downstream of the target, referred to as YD (YY1 downstream) to detect the forward scattered higher energy particles. For this experiment, the YU detector array was placed at a distance of 80.8 mm from the target center and hence it covered laboratory angles from 125° to 150°. The YU detectors are single-layered with a thickness of 500 microns and it uses an energy-angle correlation to identify the particles. The YD detectors were placed at a distance of 86 mm downstream to the target and they covered laboratory angles from 30.1° to 56.2°. It is only 100 microns thick and is backed by a CsI scintillator further downstream. The combination of these two detectors uses a ΔE-E correlation to identify particles. This is also known as a telescopic configuration, where the first detector is a thin detector, and the particles of interest pass through this, and the second

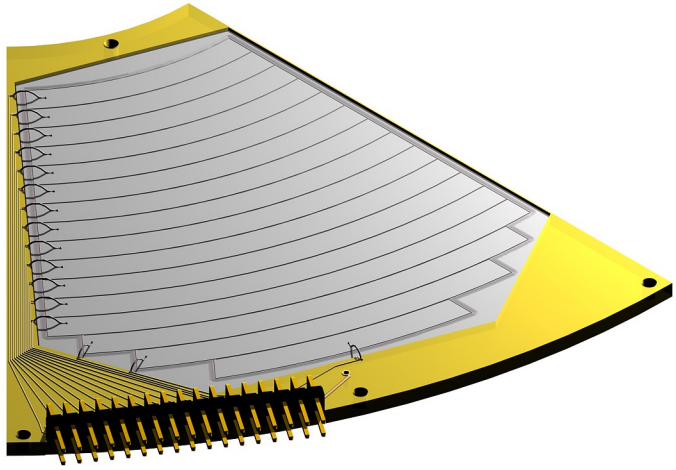

(a) An image of the YY1 detector showing 16 rings, adapted from Micron semiconductors [53]

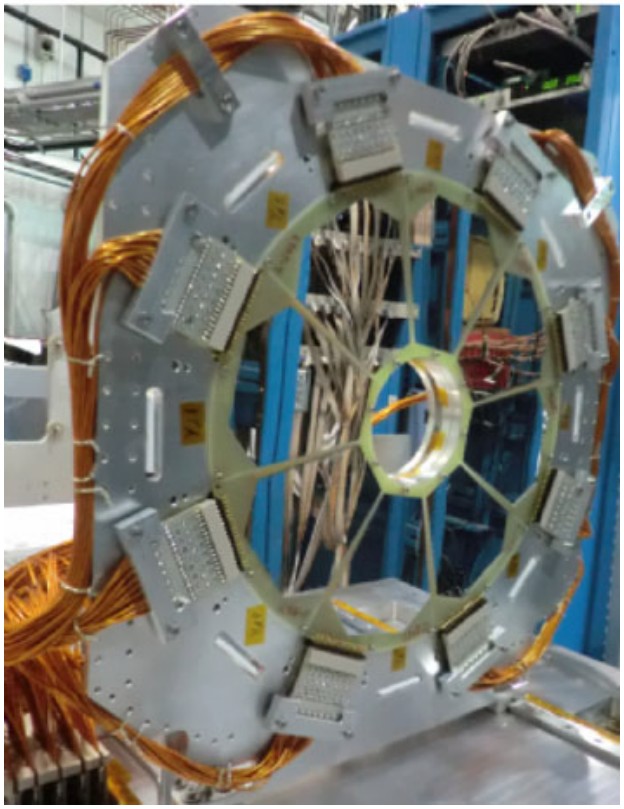

(b) An image showing an array of eight YY1 detectors, adapted from [52]

Figure 3.4: Pictures of the YY1 detector

detector is a thicker one and the particles get stopped in this detector. The first detector (YU) measures the energy lost by the particles (ΔE) and the second one (CsI) measures the remaining energy (E) of the particles. The CsI scintillator is a 12 mm thick annular array of 16 individual crystals that are read out using silicon photodiodes as shown in Figure 3.5a. The 16 crystals of CsI detector array are placed right behind YD and both of them are in the same azimuthal configuration with each of the YD sectors coinciding with two sectors of the CsI scintillator.

To detect the heavy recoils, which pass through the central aperture of the YD detector, two S3-type detectors, SD1 and SD2 (Figure 3.5b), made by MICRON Semiconductors, were placed downstream to the YD in a telescopic configuration to have a ΔE-E identification of the heavy residues of the reaction. SD1 has a thickness of 60 μm and SD2 is 500 μm thick. The SD1 and SD2 detectors were placed at 600 μm and 690 μm, respectively, downstream of the target. The SD detectors have 24 rings on the front side that measures the energy and 32 sectors on the backside for azimuthal angle information [54].

3.3 Signal Processing

The detectors used for this experiment were semiconductor detectors and they work by the generation of electron-hole pairs when charged particles interact with them. Semiconductor detectors are reverse biased in order to get a larger depletion zone which acts as the active volume for detection. These charge carriers (electron-hole pairs) are then collected by the electric field present in the active volume, which is then converted into a voltage pulse [55]. The intensity of this voltage pulse is proportional to the charge of the charge carriers which in turn depends on the energy deposited by the charged particle in the detector. The first components of the signal processing unit are the preamplifiers. The preamplifiers used for this experiment integrate the charge in the input pulse and the amplitude of the output pulse is proportional to the total integrated charge. The output pulse has a sharp rise and a slow decay and these times depend on the time constant of the RC circuit. For pulse shaping and further amplification, these signals are passed through the shaping amplifiers.

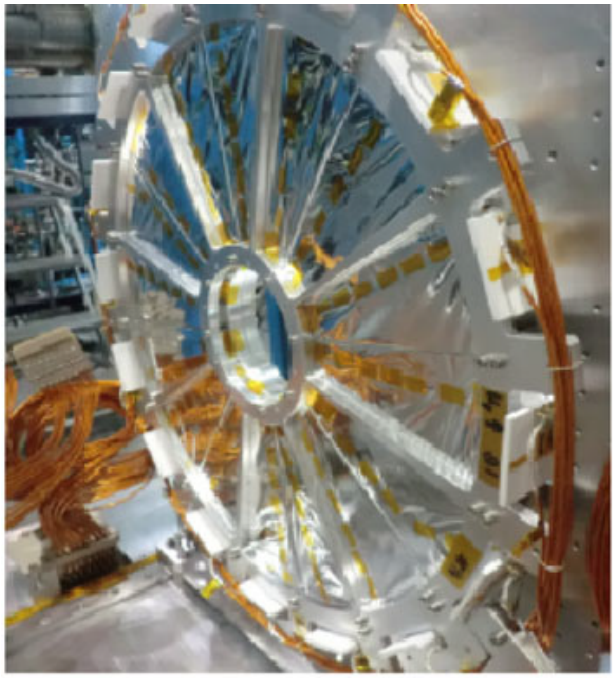

(a) An image of the CsI Detector [52]

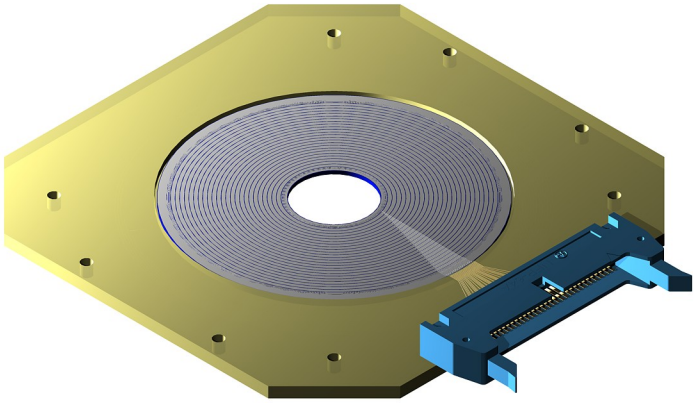

(b) An image showing the front side of the S3 detector, adapted from Micron semiconductors [54]

Figure 3.5: Pictures of the CsI and Micron S3 detectors

IRIS uses the Mesytec MSCF-16 shaping and timing amplifiers with a leading-edge constant fraction discriminator. They are 16-channel NIM modules with a CR-RC network that amplifies the signal and changes the shape of the output pulse from the preamplifiers to Gaussian. The discriminator in the MSCF-16 generates a logic pulse only if the input signal is above a particular voltage threshold. This threshold is set by the user to reject the electronic noise and the logic pulse is used to generate the trigger. The thresholds were set to an optimal value such that noise wouldn't flood the system. The energy of the particle is obtained from the pulse height of the Gaussian waveform. The next component in the series is a peak sensing analog to digital converter (ADC). MADC-32 ADCs are used at IRIS which are made by Mesytec. The ADCs had a resolution of 12 bits and they digitize the voltage spectrum into 4096 channels, meaning they convert the voltage amplitude to a digitized number which is then stored by the data acquisition computers (DAQ). Each ADC channel corresponds to a particular voltage which in turn gives the energy of the detected particle once it is calibrated.

3.4 Specifics of the experiment

The ^{12}Be beam was delivered by ISAC II and the IRIS setup was used to study the ejectiles and the recoils from the reaction. To calibrate the detectors, a triple alpha source was used. It was placed at different positions to calibrate different detectors. After that, a ^{12}C(d,p) reaction was performed to benchmark the calibrations and the setup, since ^{13}C is a well-known nucleus. The ISAC II beamline delivered ^{12}C beam for six hours at an energy of 9.5 MeV/u which reacted on the solid deuteron target with thickness around 45 μm. We probed the $^{12}\mathrm{C(d,p)}^{13}\mathrm{C}$ channel by detecting the protons using the YU detector. Data from the $^{12}\mathrm{C(d,p)}$ reaction was used as an internal calibration to benchmark the experimental setup before carrying out the $^{12}\mathrm{Be(d,p)}$ reaction. For studying the $^{12}\mathrm{Be(d,p)}^{13}\mathrm{Be}$ reaction, the same procedure was followed. The target was changed before the start of the beryllium run and also halfway through the experiment. The ^{12}Be beam time was close to 4.8 days. The details of the analysis will be explained in the next chapter.

Chapter 4

Data Analysis

In this chapter, the details of the data analysis of ^{12}Be(d,p)^{12}Be are presented using the concepts outlined in Chapter 2. This will include details about the energy calibration of detectors, beam identification, measurement of the target thickness, construction of reaction kinematics spectra, and the Q-value spectrum.

4.1 Beam Identification

The first detector through which the radioactive beam passes is the ionization chamber (IC). As presented in the last chapter, the IC is placed upstream of the target to identify the impurities in the beam. Different beam species lose energy at different rates while passing through the isobutane gas in the IC since the stopping power of a charged particle is proportional to the square of its atomic number. Figure 4.1 shows the ADC spectrum of the ionization chamber. There are two peaks. The one marked with red vertical lines corresponds to ^{12}Be, the other peak is due to the noise from the electronics.

4.2 Energy Calibration of the Detectors

During the experiment, the data in the form of ADC (analog to digital converter) is recorded. There is a linear relationship between the energy of the particles and these recorded signals

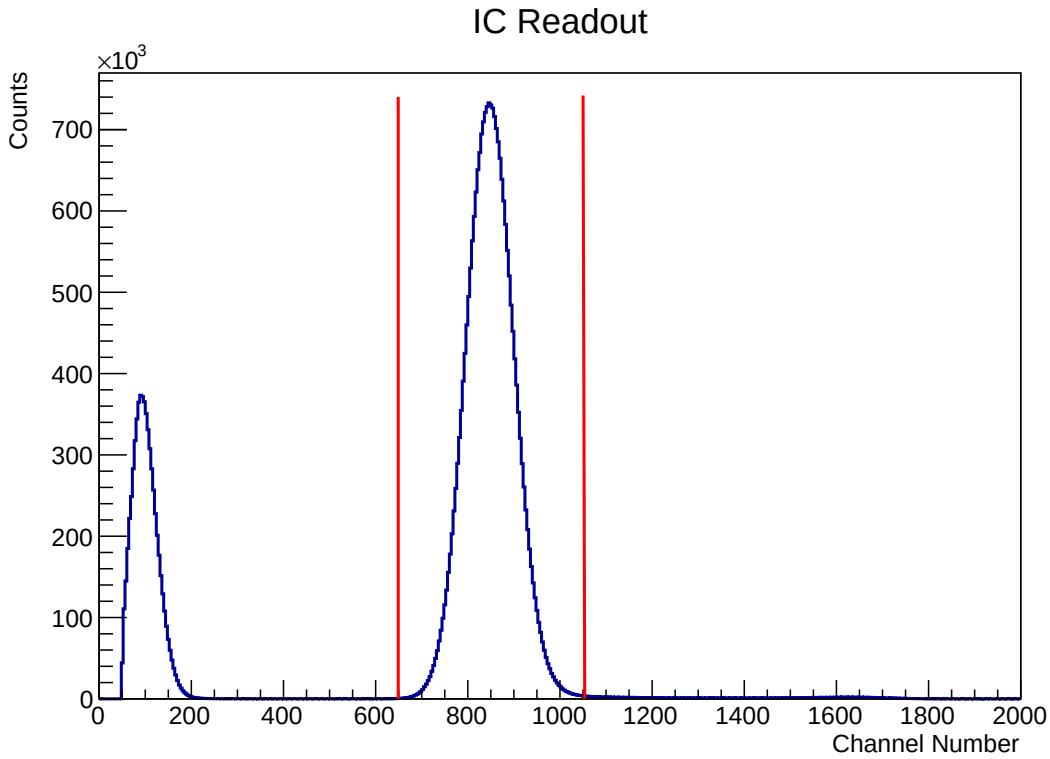

Figure 4.1: Beam energy loss through the ionization chamber is shown in the channel number. The peak marked with the red gates corresponds to the ^{12}Be beam and the other peak is from noise

which is given by,

$$E = a \times (C - P) + b, \tag{4.1}$$

where E is the incident energy, C is the channel number, P is the pedestal, which is the offset in the channel number when there is no incident ion, and a and b are the slope and intercept of the linear fit, respectively.

4.2.1 Calibration of the YU detectors

The YY1 detectors were calibrated using a triple alpha source consisting of the radioactive isotopes ^{239}Pu, ^{241}Am, and ^{244}Cm which emit alpha particles of energy 5.155 MeV, 5.486 MeV, and 5.805 MeV respectively. These energies correspond to the alpha decays with the highest branching ratio in the fine structure for each of the nuclei. The YY1 detectors have two dead layers in the front which are 0.1 μm thick Aluminum and 0.05 μm thick Boron. The alpha particles lose some energy while passing through these and hence the detector will record energies that are lower than the nominal values. The alpha energy spectrum for one out of the 128 strips of the YU detector is shown in the Figure 4.2. The peaks were identified and they were fitted using a convolution of three Gaussian functions with a single standard deviation since that is the property of the detector strip. The peak positions were taken as the channel numbers corresponding to the alpha energies. All the 128 strips were calibrated using the relation given in Eqn. 4.1.

4.2.2 Calibration of the S3 detectors

There were two S3 detectors placed downstream. The first one called the SD1 was calibrated using the same triple-alpha source which was used for the YU detector (Figure 4.3). The SD2 was calibrated using the ^{12}C data with and without the solid deuterium target. It was a two-point calibration, using the ^{12}C elastic peak when there was no target and the ^{4}He punch-through point with the target in. A punch-through point is defined as the energy at which a particle starts to pass through the detector without depositing all of its energy. The maroon circle in Figure 4.5 shows the punch-through point for ^{4}He. The channel numbers of these two points were then calibrated with the corresponding energy values using Eqn.

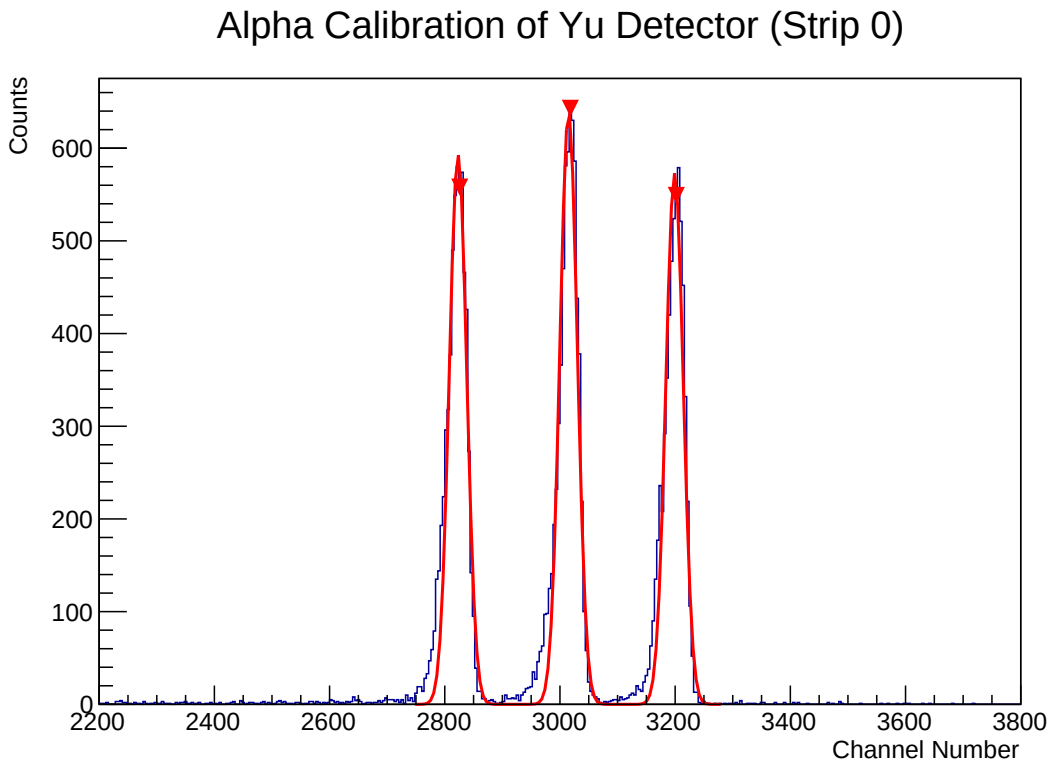

Figure 4.2: Calibration of a YU detector strip with ADC channel number, showing three peaks arising from ^{239}Pu, ^{241}Am, and ^{244}Cm emitting alpha particles of energy 5.155 MeV, 5.486 MeV, and 5.805 MeV respectively. The fine structure of the decay can be seen for each of the nuclei. The decay channel with the highest branching ratio was chosen for calibration. The red line is a convolution of three Gaussian functions.

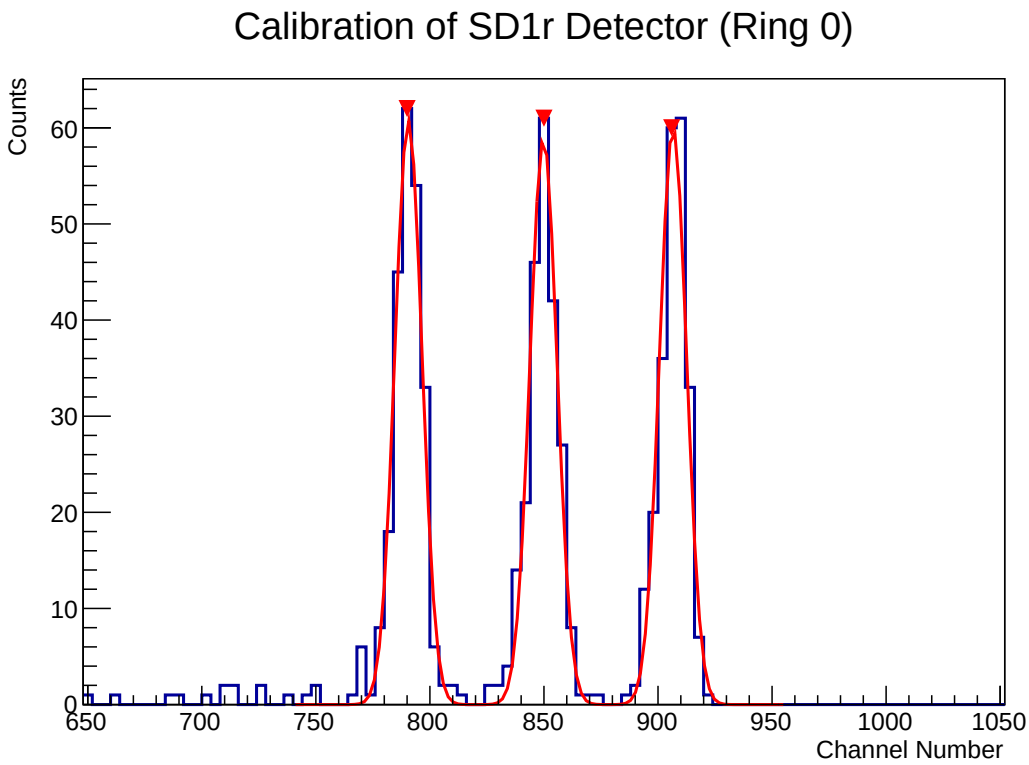

Figure 4.3: Calibration of an SD1 detector ring with ADC channel number, showing three peaks arising from ^{239}Pu, ^{241}Am, and ^{244}Cm emitting alpha particles of energy 5.155 MeV, 5.486 MeV, and 5.805 MeV respectively. The red line is a convolution of three Gaussian functions.

4.1. The ^{4}He punch-through point position was calculated from LISE++ [56], which gave the energy deposited in SD1 and SD2.

4.3 Target Thickness Estimation

The thickness of the solid deuterium target is an important parameter in the experiment. For the analysis, it is assumed that the reaction happens at the center of the target. In order to calculate the energy lost by the protons while traversing through the target, the target thickness needs to be estimated. For this calculation, the beam energy recorded in SD1 and SD2 was obtained and all the energy losses through the dead layers of the SD detectors and the silver foil were added back. This is called the reconstructed energy. The beam loses more energy when there is a target. Figure 4.4 shows the reconstructed energy of ^{12}Be beam with and without the target and the difference in these energies was used to find the target thickness. For the ^{12}C run, an average target thickness of 47 microns was estimated. During the ^{12}Be run, the target was changed twice and the thickness was measured to be 43.8 microns during the first half and 39.6 microns during the second half.

4.4 ^{12}C(d, p)^{13}C Reaction

The ISAC II beamline delivered ^{12}C beam at an energy of 9.5 MeV/u which was then allowed to react with the solid deuterium target. The ^{12}C(d, p)^{13}C channel was investigated by detecting the emergent protons measured in the YU detector.

The particle identification in the SD telescope was used to isolate the reaction channel of interest. A gate was applied on the ΔE-E locus of ^{13}C (Figure 4.5). The protons detected by the YU detectors that were in coincidence with ^{13}C were analyzed. After gating on the IC and the PID plot (Figure 4.5), the kinematic locus of the ground state and the first three excited states of ^{13}C from the data were obtained (Figure 4.6). These were then compared with the known spectrum of ^{13}C to benchmark for the reaction kinematics, e.g., the beam position on the target and the distance from the target to the detector. The latter was adjusted as an internal calibration of the measured kinematic spectrum.

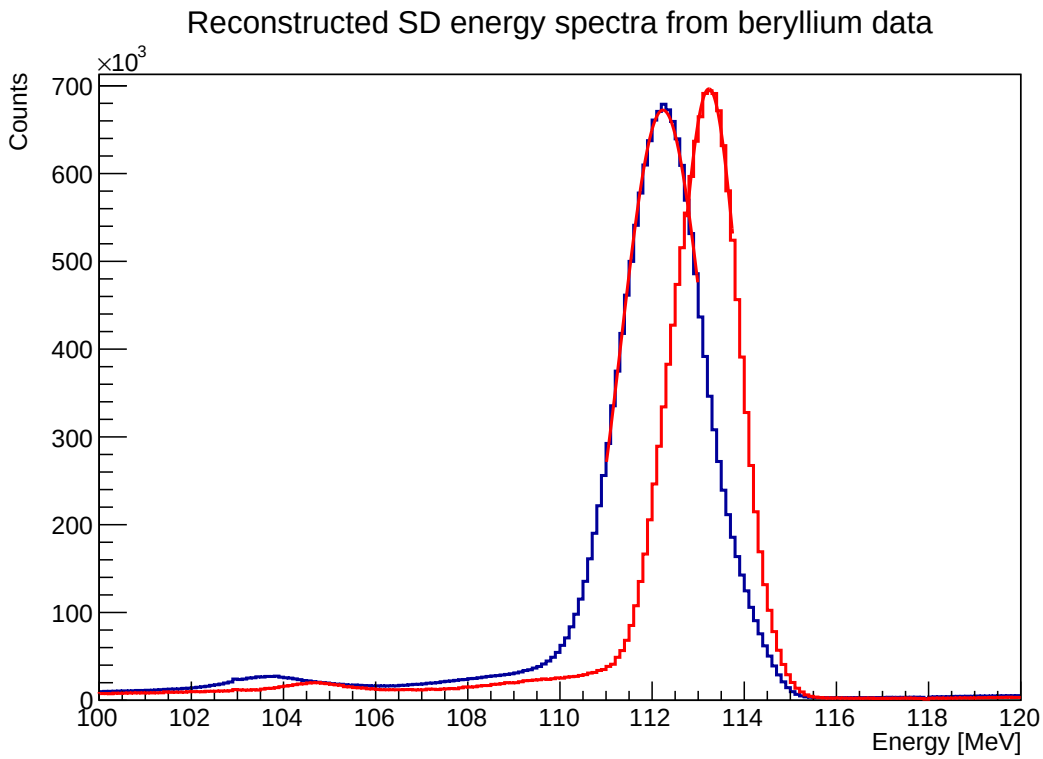

Figure 4.4: Reconstructed SD energy of the beam from the ^{12}Be beam run. This is the energy of the beam after it passes through the silver foil. The red peak shows the energy of the beam with only the silver foil and the blue peak shows the energy of the beam with the solid deuterium target and silver foil backing. The thickness of the target can be calculated from the difference in energy.

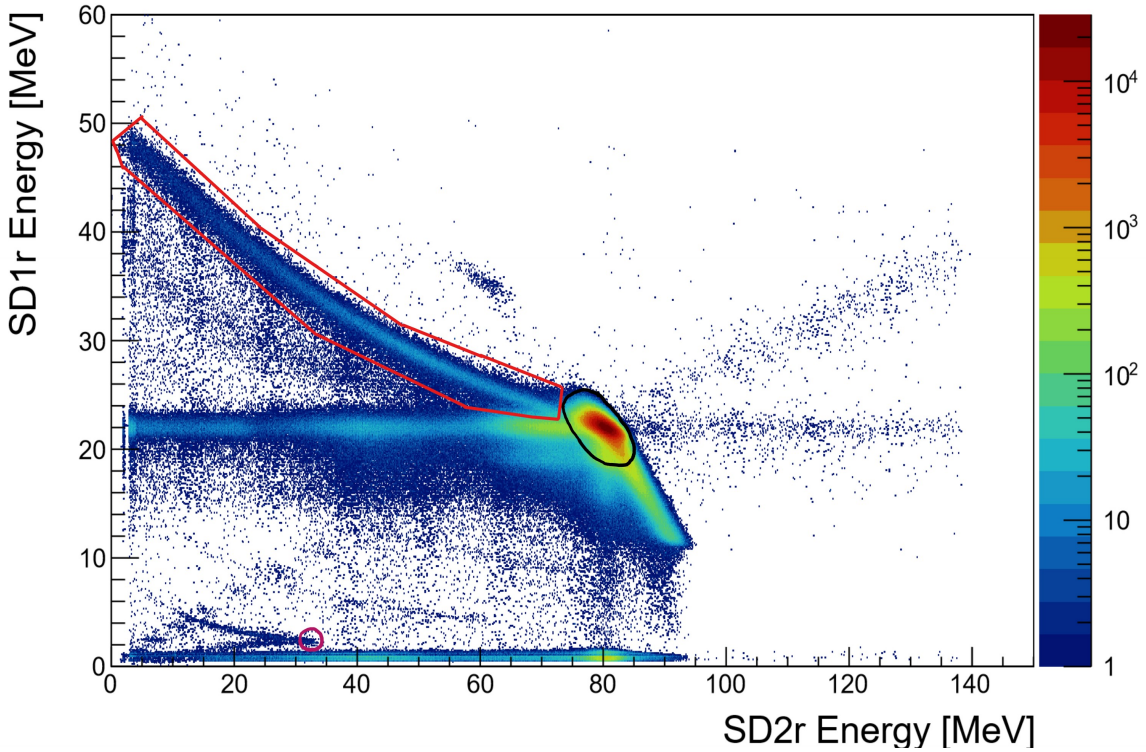

Figure 4.5: Particle identification plot for recoils from the ^{12}C + d data from the SD telescope. The red cut includes both the ^{13}C and the scattered ^{12}C, the black gate shows the elastic scattering, and the maroon circle shows the ^{4}He punch-through point.

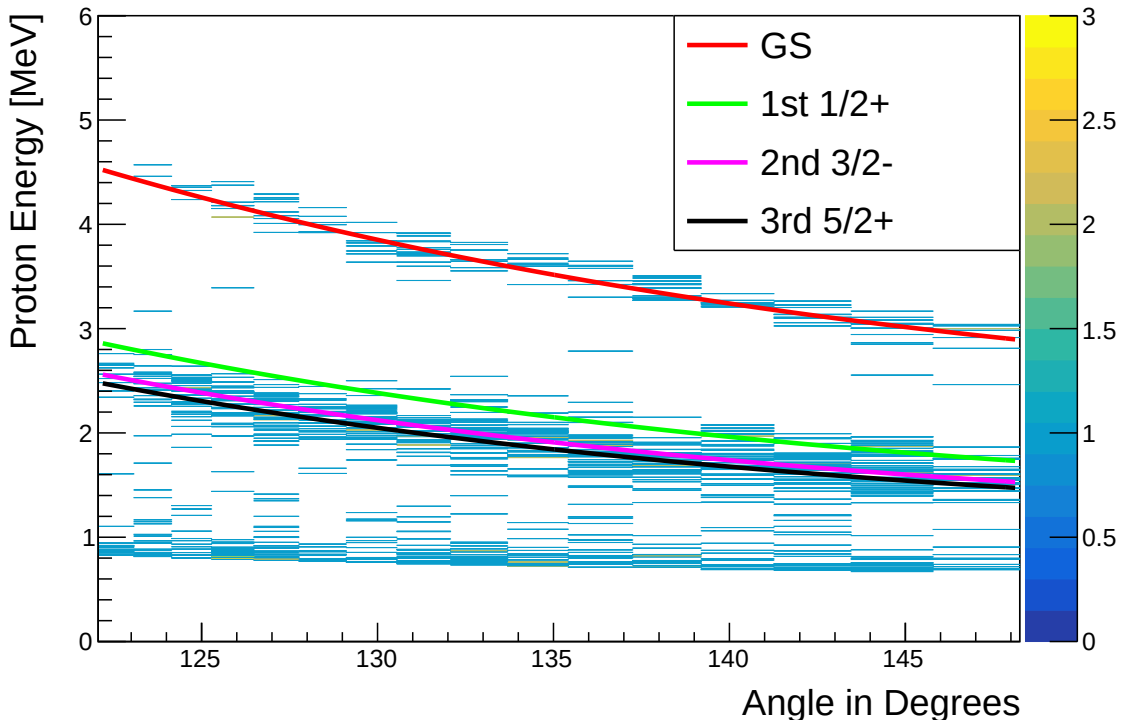

Figure 4.6: Proton energy versus angle in the laboratory frame following the ^{12}C + d reaction after gating on the IC and the PID plot, and a detector threshold of 500 keV. Calculations of the kinematics for populating the lowest four states in ^{13}C are shown using solid lines.

The Q-value spectrum of ^{13}C was obtained with the gates mentioned above. It was calculated on an event-by-event basis using Eqn. 5.2 in Chapter 2. In a typical Q-value spectrum, the ground state of the recoil nucleus will have the highest Q value and the higher excited states will be to the left of that. Four known states of ^{13}C were identified. The second and the third excited states were not resolved. Hence, this spectrum was fitted using a convolution of three Gaussian functions which includes the ground state, and the first three excited states with the second and third excited states modeled using a single Gaussian. A common standard deviation parameter was used for the ground state and the first excited state but a different one for the unresolved second and third excited states. Figure 4.7 shows the Q-value spectrum along with the fit. Table 4.1 gives a comparison of the measured Q-values and the previously reported Q-values of some of the low-lying states of ^{13}C.

The background from the silver foil is not present in the angular range of the YU detector since neither the beam nor the emergent protons can make it through the silver foil and this was confirmed with the data taken without a D_2 target formed as shown in Figure 4.8.

4.5 ^{12}Be(d,p)^{13}Be Reaction

Following the ^{12}C stable beam run, the ISAC II accelerator delivered ^{12}Be beam for 4.8 days at an energy of 9.5 MeV/u which was reacted on the solid deuteron target of IRIS. The $^{12}\mathrm{Be(d,p)}^{13}\mathrm{Be}$ channel was probed by detecting the reaction protons using the YU detector.

Since ^{13}Be is neutron unbound it decays into ^{12}Be and a neutron with a half-life of, $T_{1/2} \approx 10^{-21}$ s. To select only the $^{12}\mathrm{Be(d,p)}$ events, a cut was applied to the SD telescope and analyzed the protons detected by the YU detectors. These proton events coincide with the events falling inside the gate.

The punch-through points for ^{4}He and ^{6}Li are marked in the PID plot (Figure 4.9). These points were compared with the reported values to check the calibration of the SD detectors and were found to be within the error bars.

The proton kinematics from the $^{12}\mathrm{Be(d,p)}$ reaction, shown in Figure 4.10 were obtained by gating on the IC (Figure 4.1) and the PID plot (Figure 4.9). It is very hard to identify the states from the kinematics spectrum itself and one needs to look at the Q-value spectrum

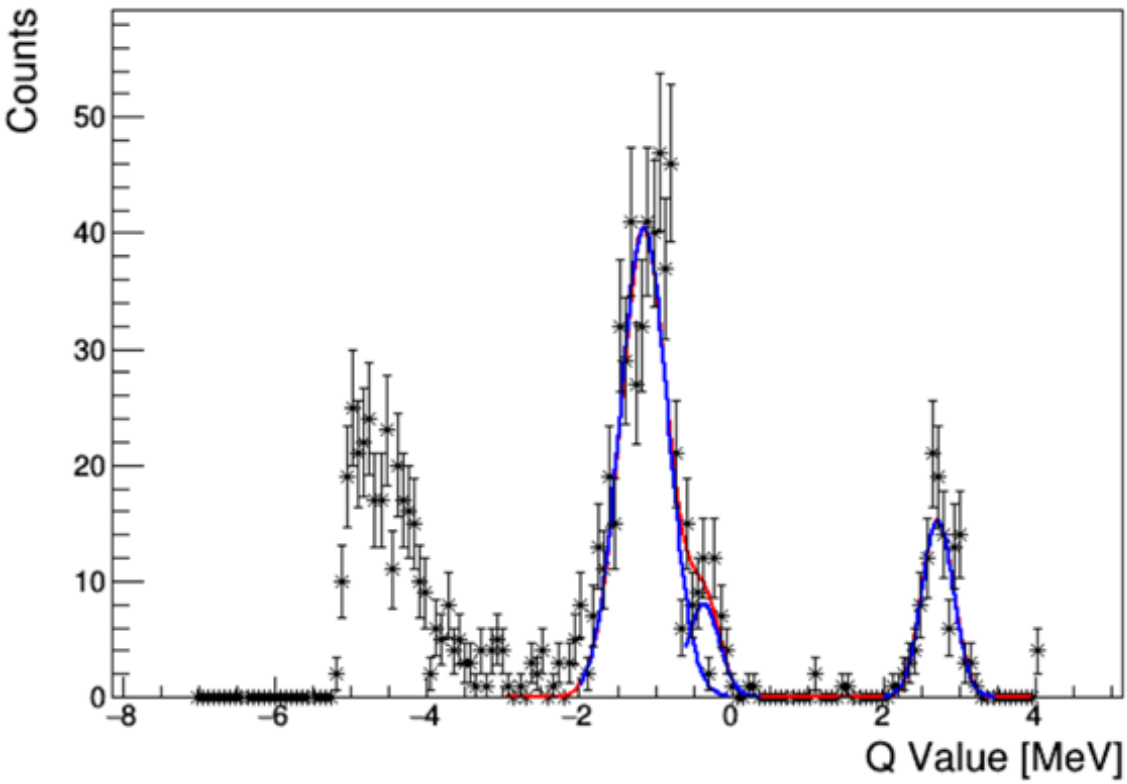

Figure 4.7: ^{13}C Q-value spectrum obtained from ^{12}C + d reaction. The data is shown as black points with statistical error bars. A global fit to the data is shown as a red line using a convolution of three Gaussian functions. Individual fits for the ground and the first excited states are shown. The second and third excited states were not able to be resolved. Hence, the unresolved peak was fitted using a single Gaussian function.

Table 4.1: A table showing the Q values of the states populated in ^{13}C using ^{12}C + d reaction. The ground and the first excited states were able to be resolved. The second and the third excited states were unresolved and hence that peak in the Q-vale spectrum was fitted using a single Gaussian function. Previously measured Q values of the ground state and the first excited states are given for comparison ^{13}C. The standard deviations of the fits are also shown.

State	Q value [MeV]	NNDC [MeV]	Gaussian S.D. [MeV]
G.S.	2.72	2.722	0.21
I	-0.35	-0.36	0.21
II + III	-1.15	-0.962 + 1.132	0.32

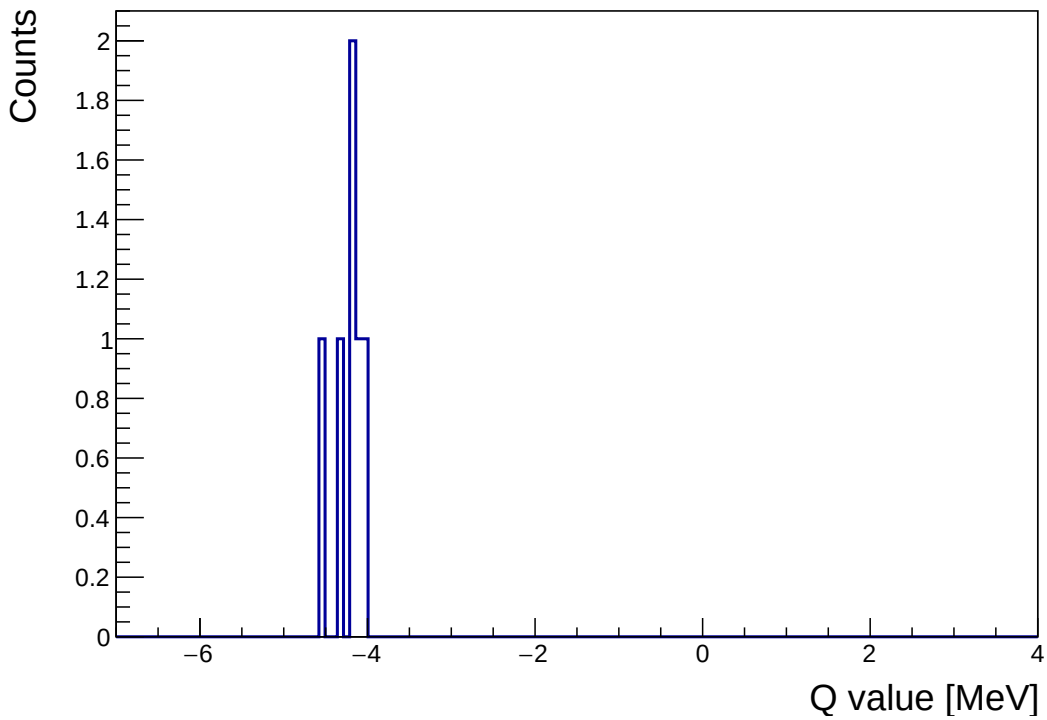

Figure 4.8: A Q-value spectrum calculated for ^{12}C beam impinging on the silver backing target shows no significant data after applying the gates on IC and PID, and applying the detector threshold.

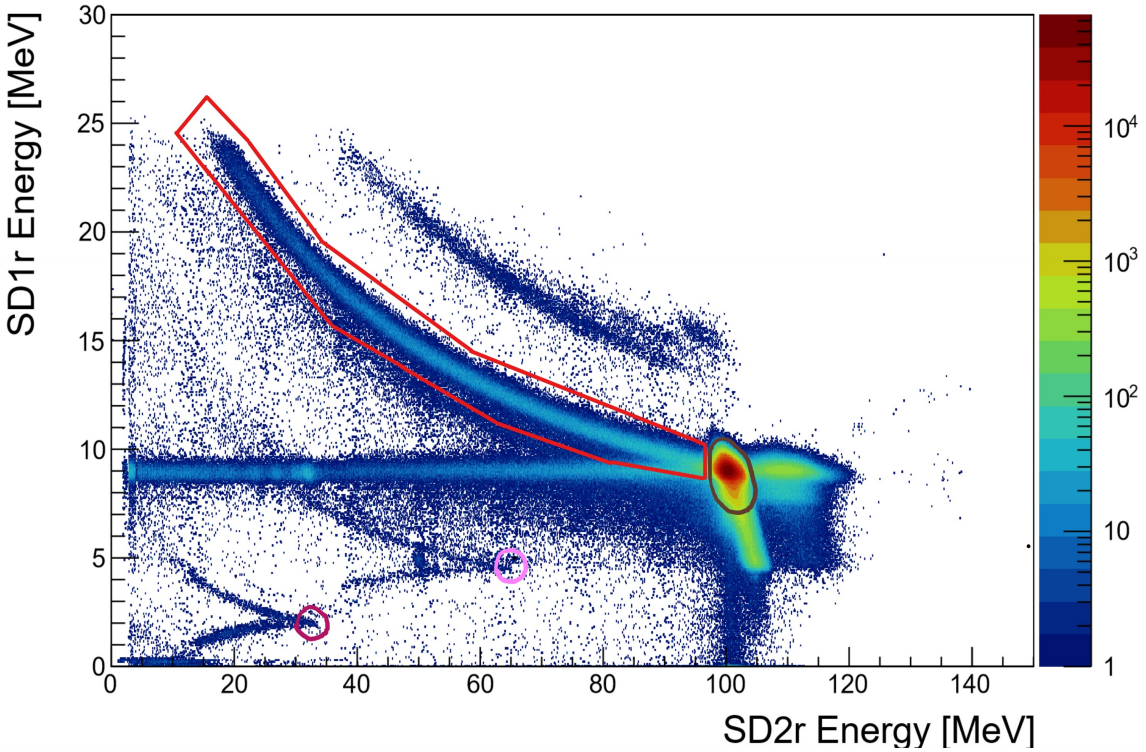

Figure 4.9: Particle identification plot for recoils from the ^{12}Be + d data from the SD telescope. The red cut includes both the reacted and scattered ^{12}Be, the black gate shows the elastic scattering, the pink and the maroon circles show the ^{6}Li and ^{4}He punch-through points, respectively.

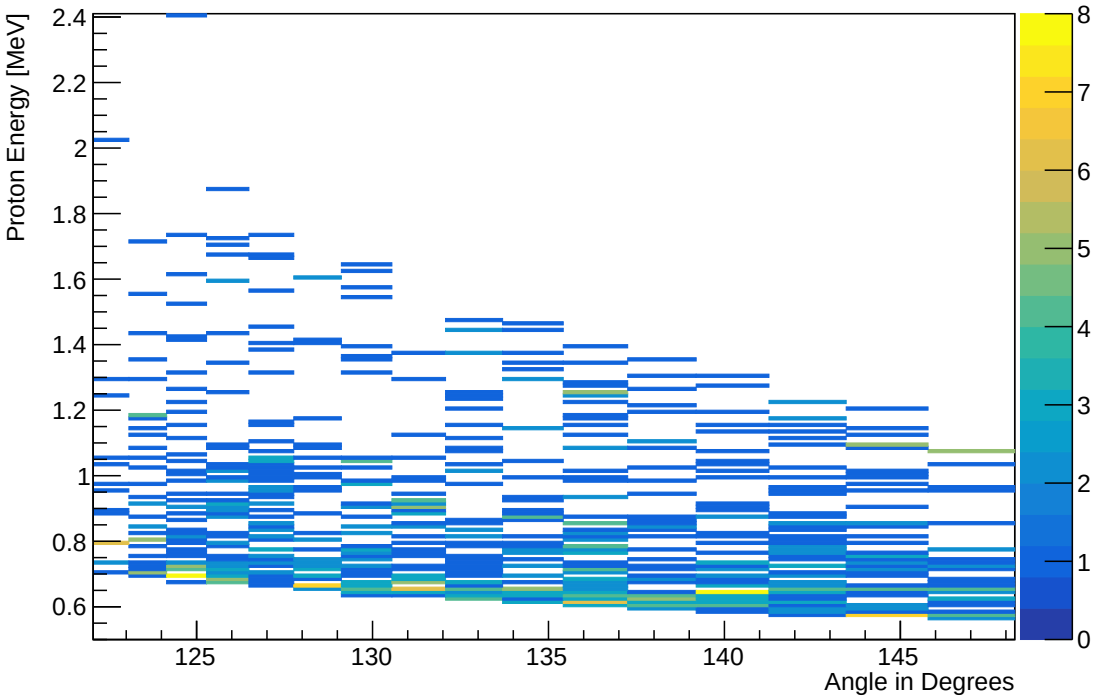

Figure 4.10: Proton energy versus angle in the laboratory frame following the ^{12}Be + d reaction after gating on the IC and the PID plot, and applying a detector threshold of 200 keV. The highest Q values populated in the reaction can be seen here and the spectrum is clean above this line.

alongside. Loci from neutron transfer can be seen in the kinematics plot shown in Figure 4.10. In particular, it can be observed that the highest Q values are populated in the reaction, and the spectrum is clean above this line.

An unbound resonance is characterized by central energy and width. These resonances lie in the region above the confining quantum potential well. A nucleus becomes neutron or proton unbound when its neutron or proton separation energy crosses zero and its wave function extends all over the space and their energy spectrum is a continuum as opposed to the discrete energy levels of nucleons confined inside the potential well. At low, positive energies, these unbound states can exist as resonances for a finite time and these are confined to a finite region of space and can be measured experimentally [57]. This resonant decay can be modeled using a Breit-Wigner line shape and the scattering cross-section for a reaction $\mathrm{a} + \mathrm{X} \longrightarrow \mathrm{b} + \mathrm{Y}$ is of the form,

$$\sigma(E) = \frac{\pi}{k^2} g \frac{\Gamma_{aX}\Gamma_{bY}}{(E - E_R)^2 + \Gamma^2/4}, \tag{4.2}$$

where Γ_{aX} and Γ_{bY} are the entrance and exit channel widths and Γ is their sum. E_R is the central energy.

Figure 4.11 shows the measured Q-value spectrum from the ^{12}Be+d reaction. The first attempt to fit the spectrum was using a fixed-line shape. Unlike the ^{13}C where there are only discrete, bound states, in order to fit the Q-value spectrum of ^{13}Be, a pseudo-Voigt function folded with a non-resonant background of the function form of a fifth-degree in energy above the threshold was used. A pseudo-Voigt function is a convolution of Lorentzian (Eqn. 4.2) and Gaussian, to account for the lifetime of the states and the detector resolution, respectively. The results of the fit are shown in Table 4.2.

The fit in Figure 4.11 gives three peaks. The resolution of the detector, as a Gaussian width (shown in Table 4.2) obtained from the fits, was not practical. The detector response function is not a Gaussian since the protons from the reaction lose different amounts of energy depending on where the reaction happened inside the target and this difference plays a huge role in the detector resolution since the protons are of very less energy as can be seen in Figure 4.10. Thus, in order to interpret the data further it was necessary to use

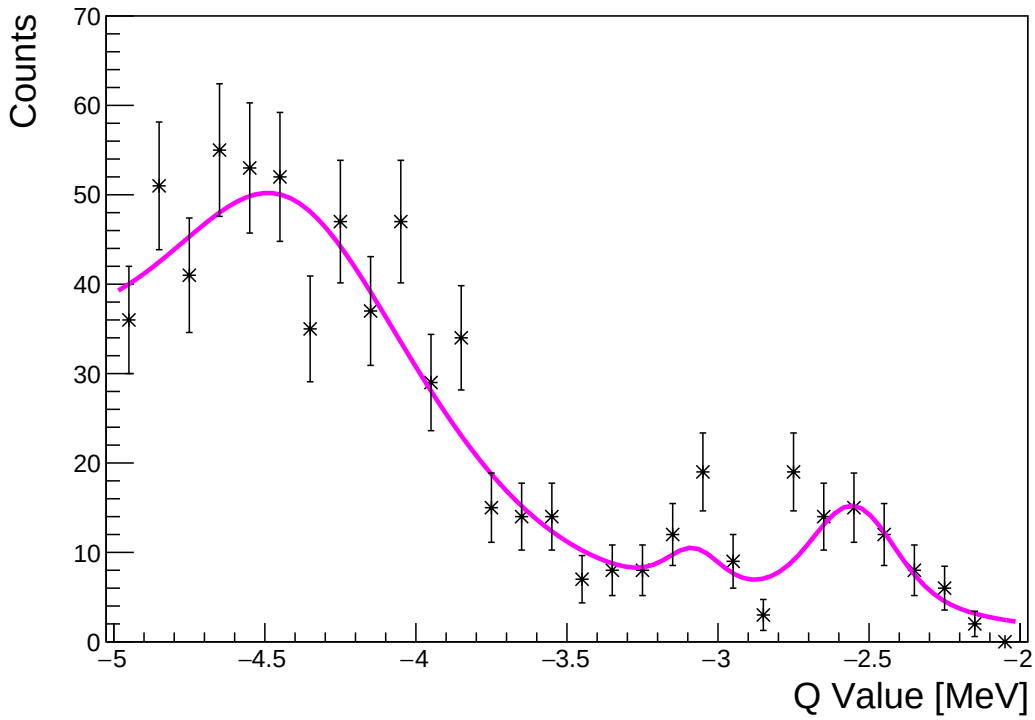

Figure 4.11: ^{13}Be Q-value spectrum obtained from ^{12}Be + d reaction. The data is shown as black points with statistical error bars. A global fit to the data is shown as a pink line using a convolution of three pseudo-Voigt functions to model three resonances.

Table 4.2: A table showing the Q values of the resonances in ^{13}Be using ^{12}Be + d reaction. The energies above the neutron threshold, Lorentzian width, and the Gaussian S.D. of the pseudo-Voigt function are also displayed. The Gaussian S.D.s are too small and hence these values cannot be used to model the ^{13}Be Q-value spectrum.

State	Q value	Energy above threshold	Lorentzian width	Gaussian S.D.
I	-2.65	0.43	0.30	0.25
II	-3.07	0.85	0.23	0.35
III	-4.01	1.78	0.36	0.49

a GEANT4 simulation that accounted for the energy loss of the beam in the ionization chamber, the energy loss of the beam and the reaction protons in the solid deuterium target, the resolution of the YU detector, and the non-resonant background.

4.6 GEANT4 Simulations

GEANT4 is a simulation toolkit developed by CERN to simulate the passage of particles through matter [58]. It has applications in particle physics, nuclear physics, accelerator physics, and other fields. It is object-oriented C++, Monte Carlo simulation software that can track the path of particles and their interactions with detectors according to physics models. Different physics processes are included covering hadronic, electromagnetic, and optical phenomena. The GEANT4 material database consists of a wide range of particles, elements, compounds, and materials, over an energy range spanning eV to TeV. Complicated detector geometries can be designed in GEANT4 to simulate an actual experiment that could be affected by detector efficiency and geometry.

The exact detector geometry and other parameters of the experiment setup were modeled in GEANT4 including the resolution of the silicon detectors in the simulation. GEANT4 was used to simulate the reaction of beam particles with the target and the passage of ejectile particles through the detector, given the beam species and the target material, and it provides a detector response function. The number of beam-on-target events sampled in the simulation can be varied. Increasing the sample size gives a better convergence for Monte Carlo simulations, but is also very expensive computationally and takes a long time to finish.

4.7 Bayesian Optimization

In this work, our aim was to accurately model the ^{13}Be Q-value spectrum by including the detector response and the energy losses in the target. In order to do this, the simulations needed to be repeated multiple times to find the best fit for the spectrum. Techniques like random search or grid search are not feasible in this scenario due to the computationally

intensive nature of these simulations. Hence, we resorted to a technique called Bayesian Optimization [59], which will be discussed in this section.

Bayesian Optimization (BayesOpt) is a technique to find the extremum of black-box functions which are functions whose analytic form is unknown [60, 61, 62]. In the context of BayesOpt, these functions are called objective, target, or test functions. The advantage over other methods is that the derivative of the function is not required in order to find the maxima and is faster and more effective than a random search of parameters which optimizes the objective function. Given a small number of evaluation inputs and their corresponding outputs of the objective function, BayesOpt iteratively selects the next evaluation point to explore so that the extremum is reached in a minimum number of iterations. BayesOpt is especially useful in finding the best parameters that fit a function when dealing with time-consuming fitting procedures. In such cases, a common gradient-based local optimization technique is not appropriate.

The two main components of BayesOpt are a Bayesian statistical model to model the objective function and an acquisition function which tells us where to sample next. The input variable $\mathbf{x}$, is represented as a vector, as there can be more than one input variable. The output, also known as the target is denoted as y. If there is a data set of n observations, it can be represented as $\{(\mathbf{x_i}, y_i)|i = 1, ..., n\}$

The aim of this method is to make predictions for new inputs, given this finite training data set. In order to do this, we have to assume some characteristics of f. An approach to do this is to assign a prior probability to every possible function that can fit the data where a higher probability is given to functions that are more plausible. The objective function is commonly expected to have certain properties to be able to use BayesOpt [63].

- The dimension of the input variable shouldn't be too large. $\mathbf{x} \in \mathbb{R}^d$, typically $d \leq 20$.
- The objective function should be continuous in order to use Gaussian process regression.

First, the objective function is evaluated at points chosen randomly. Then, a probability distribution based on the evaluated points, which in this case is a Gaussian process, is updated as more evaluations are made.

4.7.1 Gaussian Process

A Gaussian process (GP) is a probability distribution over continuous functions that could fit a set of points. In the case of regressions, GP provides confidence for the predicted function by incorporating prior knowledge. GP uses a multivariate normal Gaussian distribution with a mean vector and a covariance matrix. The mean vector is constructed at each $\mathbf{x_i}$, described by $\mu(\mathbf{x_i}) = \mathbb{E}[f(\mathbf{x_i})]$ and the covariance matrix, or kernel is calculated at each pair of points $\mathbf{x_i}$ and $\mathbf{x_j}$, defined by $k(\mathbf{x_i}, \mathbf{x_j}) = \mathbb{E}[(f(\mathbf{x_i}) - \mu(\mathbf{x_i}))(f(\mathbf{x_j}) - \mu(\mathbf{x_j}))]$. Our aim is to distance the input points for exploration to get maximum information with just a few evaluations. Hence, the kernel is defined in a way that closer input points give rise to a larger correlation as their function values are likely to be similar. A prior distribution is created which is a normal distribution of the above defined means and covariances. For k evaluations, this prior distribution on $[f(x_1), ..., f(x_k)]$ is given by [63],

$$f(x_{1:k}) \sim N(\mu(\mathbf{x}_{1:k}), k(\mathbf{x}_{1:k}, \mathbf{x}_{1:k})), \tag{4.3}$$

where N stands for normal distribution, $\mathbf{x}_{1:k}$ is a collection of the input points, $\mathbf{x}_1, ..., \mathbf{x}_k$. Similarly, $f(\mathbf{x}_{1:k}) = [f(\mathbf{x}_1, .., f(\mathbf{x}_k)]$, $\mu(\mathbf{x}_{1:k}) = [\mu(\mathbf{x}_1), .., \mu(\mathbf{x}_k)]$, and $k(\mathbf{x}_{1:k}, \mathbf{x}_{1:k}) = [k(\mathbf{x}_1, \mathbf{x}_1), .., k(\mathbf{x}_1, \mathbf{x}_k), .., k(\mathbf{x}_k, \mathbf{x}_1), .., k(\mathbf{x}_k, \mathbf{x}_k)]$.

After creating a prior distribution, the next step is to obtain information from it. Assume we made n observations and the function values are $f(\mathbf{x}_{1:n})$ and we would like to evaluate of $f(\mathbf{x})$ at a new point $\mathbf{x}$. We let this to be $k + 1^{th}$ iteration and the prior over $[f(\mathbf{x}_{1:n}), f(\mathbf{x})]$ is given by Eqn. 4.3. At this stage, Bayes' theorem can be used to calculate the conditional distribution of $f(\mathbf{x})$ [63],

$$f(\mathbf{x})|f(\mathbf{x}_{1:n}) \sim N(\mu_n(\mathbf{x}), \sigma_n^2(\mathbf{x})) \tag{4.4}$$

The mean and standard deviation of the above normal distribution are defined as,

$$\mu_n(\mathbf{x}) = k(\mathbf{x}, \mathbf{x}_{1:n})k(\mathbf{x}_{1:n}, \mathbf{x}_{1:n})^{-1}(f(\mathbf{x}_{1:n}) - \mu(\mathbf{x}_{1:n})) + \mu(\mathbf{x}) \tag{4.5}$$

$$\sigma_n^2(\mathbf{x}) = k(\mathbf{x}, \mathbf{x}) - k(\mathbf{x}, \mathbf{x}_{1:n})k(\mathbf{x}_{1:n}, \mathbf{x}_{1:n})^{-1}k(\mathbf{x}_{1:n}, \mathbf{x}) \tag{4.6}$$

In Bayesian statistics, this conditional probability is termed as the posterior probability distribution. From Eqn. 4.5, it can be seen that the mean, $\mu_n(\mathbf{x})$ is the kernel dependent weighted average of the prior mean at the point x, $\mu(\mathbf{x})$ and an estimate based on the previous evaluations, $f(\mathbf{x}_{1:n})$. The prior variance, $\sigma_n^2(\mathbf{x})$ and the posterior variance, $k(\mathbf{x}, \mathbf{x})$ differ by the amount of variance that was removed after observing $f(\mathbf{x}_{1:n})$.

As it was mentioned earlier, the kernel is chosen in such a way that the input points closer in space are strongly correlated. Suppose we consider three input points, $\mathbf{x}, \mathbf{x_1}, \mathbf{x_2}$, and they satisfy the conditions, $\|\mathbf{x} - \mathbf{x_1}\| < \|\mathbf{x} - \mathbf{x_2}\|$, where $\|\cdot\|$ denotes some norm, then the kernel should satisfy the condition, $k(\mathbf{x}, \mathbf{x_1}) > k(\mathbf{x}, \mathbf{x_2})$. Some of the commonly used kernel functions are Gaussian kernel and Màtern kernel [64]. Kernels are dependent on certain parameters that decide how quickly the function $f(\mathbf{x})$ changes with the input $\mathbf{x}$.

4.7.2 Acquisition Functions

The next important component in BayesOpt is the acquisition function (AF) which is calculated using the GP. There are two phases in the optimization procedure and they are the exploration phase and the exploitation phase. During the exploration phase, AF eliminates part of the input space that is very less probable to contain the maximizer of the function. This helps in shrinking the input space. During the exploitation phase, AF looks for the input values which are closest to the maximizer with high confidence. Hence, the AF plays an important role in estimating the function values efficiently by exploring regions where GP is most uncertain and exploiting the remaining parameter space by finding the input points with the highest function values.

Expected Improvement (EI) is a commonly used acquisition function. The logic behind the EI acquisition function is that at every step of evaluation, the best input parameter which maximizes the objective function will be the previously evaluated input point that gave the maximum value among all the input points that were sampled. Suppose that the iterations were stopped at an iteration number, n, with x_n being the input point and the observed value is $f(x_n)$. Assume that a solution needs to be returned from the evaluations that were already made and there will be no more iterations. Then the best choice will be to return the previously evaluated point, $x_i, i \leq n$ which gave the largest corresponding value

$f(x_i)$. If the process is iterated once more and evaluated at x obtaining $f(x)$, the highest function value can be either $f(x_i)$ or $f(x)$. Hence, the improvement, I in the best value after this iteration will be $f(x) - f(x_i)$ if it is positive or 0, otherwise, which can be written as $I = [f(x) - f(x_i)]^+$. We would like to find x that will maximize I and since $f(x)$ is unknown, our best guess will be to take an expectation value of I and choose the next point x which will maximize it. The expected improvement is defined as:

$$EI_n(x) = E_n(I). \tag{4.7}$$

Here, $E_n[\cdot]$ is the expectation value calculated under the posterior distribution (Eqn. 4.4) given the evaluations of the objective function at points $x_1, ..., x_n$. The next point of evaluation is given by $x_{n+1} = max(EI_n(x))$.

Another type of acquisition function is the upper confidence bound (UCB) function.

$$UCB(x) = \mu(x) + \zeta\sigma(x). \tag{4.8}$$

The parameter ζ determines the balance between the exploration ($\zeta \approx 1$) and the exploitation ($\zeta \approx 0$) phase of BayesOpt. When $\zeta = 0$, UCB equals the mean of the GP. Hence, UCB can be understood as a weighted sum of the mean and the standard deviation of the GP. Similar to the EI function, the next point of evaluation is chosen by $x_{n+1} = max(UCB_n(x))$. With these ingredient functions, a common algorithm for performing Bayesian optimization is given in Algorithm 1 [65].

Algorithm 1: A pseudo-code for Bayesian Optimization

```
Define prior bounds on function f
Observe f at n_0 initial points
while n ≤ N do
    Update the posterior distribution (GP) on f based on all previous data points
    Find the maximizer of the acquisition function, x_n, using the posterior
      distribution
    Find f(x_n)
    Increment n
end
Return: The point with the highest evaluated f(x) or the point with the largest
  posterior mean.
```

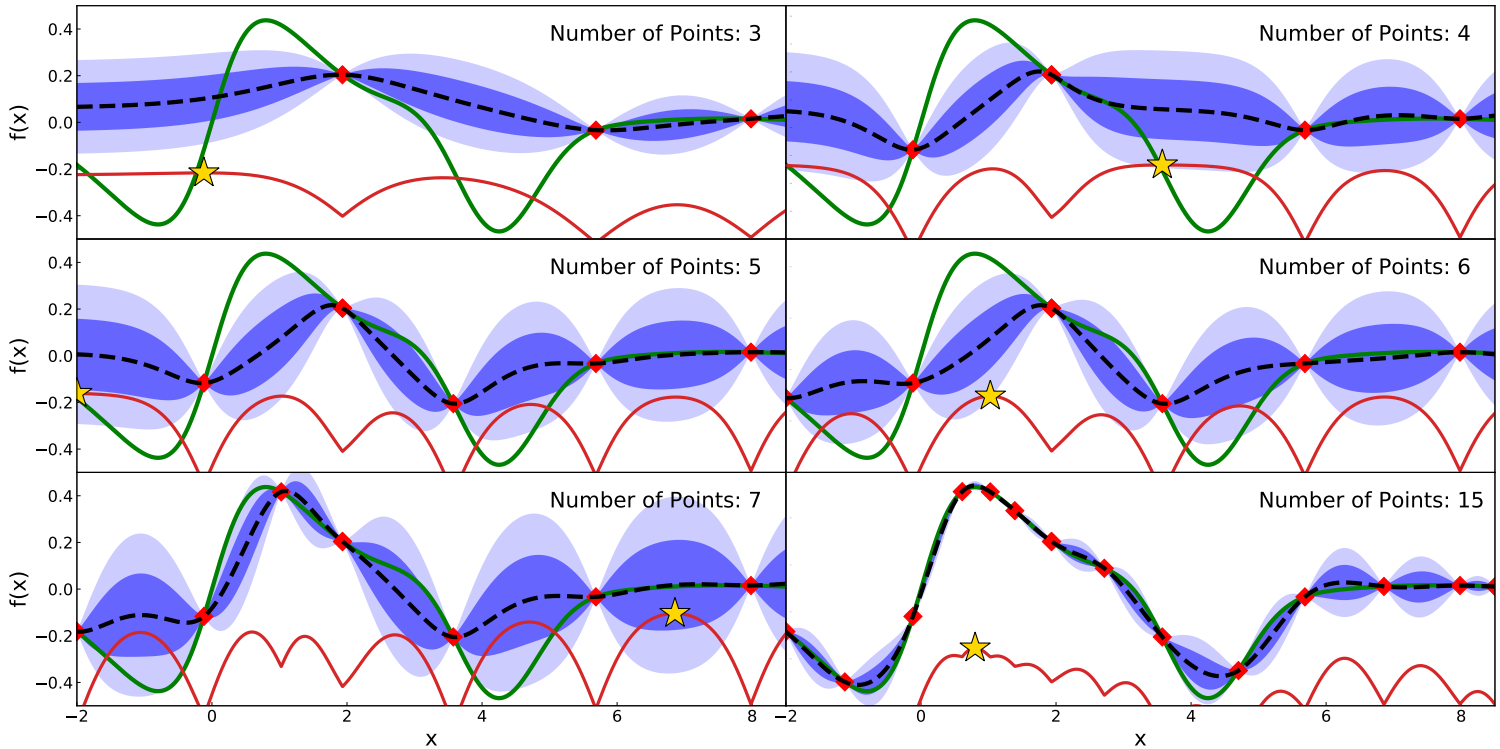

Figure 4.12: Bayesian optimization iterations performed to maximize the test function $f(x) = \left(1/(x^2+1) + e^{-(x-4)^2/2}\right)\sin(x)$ (green line). Three random evaluation points are shown as red markers. The objective function is displayed using a green curve. The mean, 1σ, and 2σ confidence intervals of the GP are shown as the black dashed line, dark blue, and light-shaded areas, respectively. The next point of evaluation obtained from the UCB acquisition function is displayed as a yellow star. As the BayesOpt routine progresses, the algorithm converges on the maximum of the function. Figure adapted from [65].

Using an example from [65], the Bayesian optimization procedure to maximize the function, $f(x) = \left(1/(x^2+1) + e^{-(x-4)^2/2}\right)\sin(x)$ is demonstrated in Figure 4.12. The process starts with the evaluation of the function at three random points, displayed as red markers. The objective function to be maximized is shown as a solid green line. The GP is depicted as a black-dashed line with 1σ and 2σ confidence intervals shown as dark and light blue shaded regions. An acquisition function calculated using the UCB method is shown as a red line and the next input point for evaluation is shown as a yellow star which is the maximum of the UCB. At first, three random input points are selected for evaluation. As the number of iterations increases, it can be seen that the GP converges to the test function and finds the global maximum. It is also interesting to see that there is a higher number of evaluations close to the maximum when compared to the other regions in the input space.

Chapter 5

Results and Discussion

In this chapter, the techniques mentioned in Chapter 4 will be applied to the Q-value spectrum of ^{13}Be to further interpret it. The GEANT4 simulations were coupled to the Bayesian optimization code to fit the spectrum and obtain the energies and widths of the low-lying strengths of ^{13}Be. We will also obtain an angular distribution for the lowest strength and fit it with different DWBA calculations. Towards the end of this chapter, we will compare our results with previous experiments.

5.1 Nilsson Levels

The shapes of very light nuclei can be considerably changed by adding just one nucleon as this has been reported in beryllium isotopes, like the N=8 shell gap breakdown in ^{12}Be [66]. This breakdown in N=8 results in the ground state of ^{12}Be being comprised of 70% sd-shell intruder configuration and with a p-shell configuration dominating the 0_2^+ state [66]. The low-lying levels of ^{13}Be could be affected by ^{12}Be core excitation. The simplest approach to model the shell structure of ^{13}Be will be to use the Nilsson model to fill the four protons and 9 neutrons in the lowest Nilsson levels. Since only the low-lying strength is studied in this work, eight neutrons can be treated as inactive. Assuming the same deformation of ^{12}Be [67] for ^{13}Be that is $\epsilon = 0.61$, a Nilsson diagram analysis was done as shown in Figure 5.1. This is a very crude way of filling the levels for ^{13}Be since the calculations were originally done for nuclei with $A \leq 50$. A projection of the diagram was obtained for $\epsilon = 0.61$ and

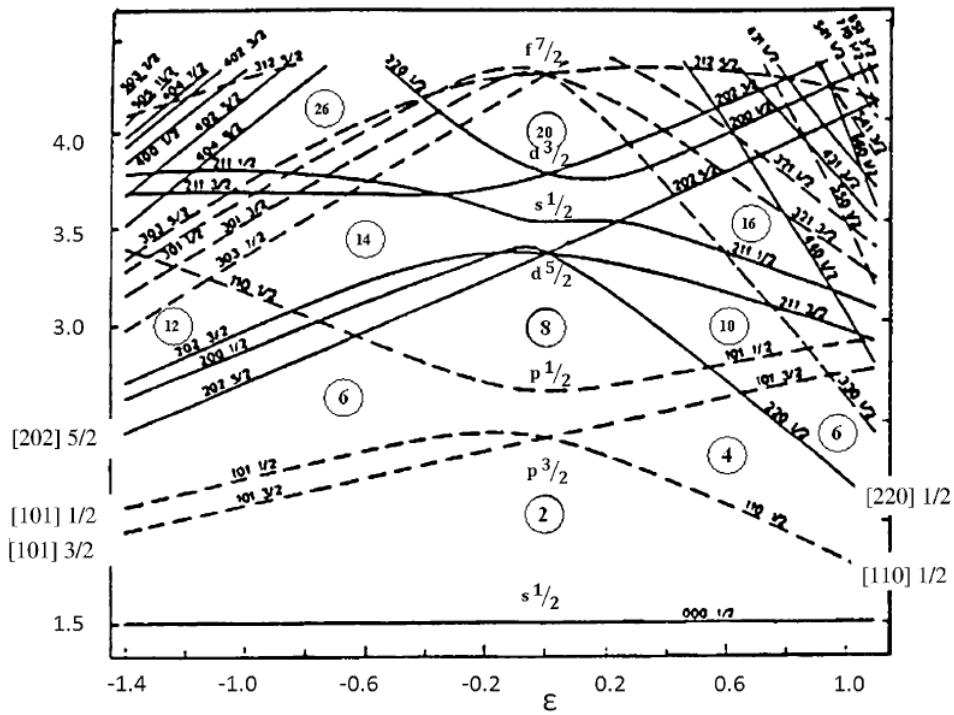

(a)

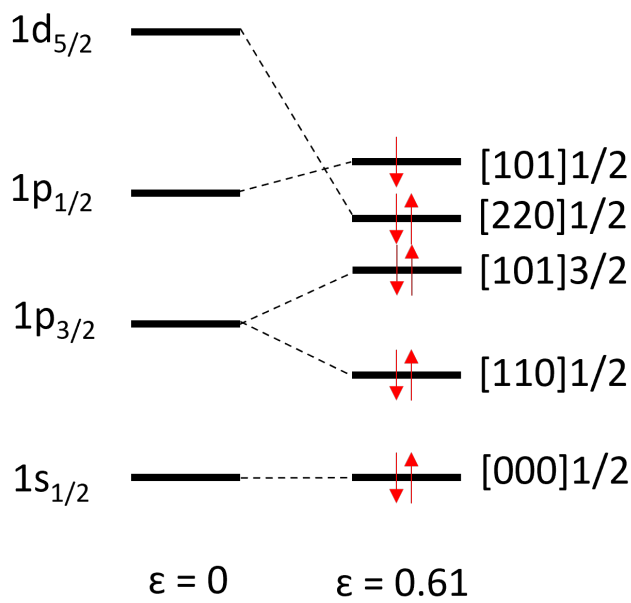

(b)

Figure 5.1: (a) shows Nilsson level diagram for neutrons for light nuclei obtained from [17]. (b) shows a schematic of the levels for ^{13}Be obtained by projecting the Nilsson diagram for $\epsilon = 0.61$.

the lowest levels were filled. Using this method, the low-lying level of ^{13}Be has a Nilsson level assignment of $[101]\frac{1}{2}$. The DWBA calculations presented in the upcoming section were carried out using the spherical shell model.

5.2 Bayesian Optimization and GEANT4 Simulations

In order to accurately model the ^{12}Be(d,p)^{13}Be reaction data, we reproduced the detector geometry in the GEANT4 simulation package. The energy loss of the ^{12}Be beam in the IC was simulated using the known thicknesses of the windows and the pressure of the isobutane gas. For consistency, the energy losses of the beam and the protons through the solid deuterium target were calculated using the GEANT4 energy loss tables throughout the data analysis as well as for the simulations. The detector resolution was characterized using data from the alpha calibrations. The non-resonant background was modeled using the fifth power of the energy above the neutron threshold, to reflect the increase in phase space. Since there was no background present in the angular region covered by the upstream YY1 detector resulting from the silver backing of the target, this did not need to be included in the simulation.

A detector response function was obtained from GEANT4 simulations using these inputs. A Q-value spectrum for ^{13}Be was simulated with the desired number of strengths, with each strength being defined by its energy, width, and probability by folding this detector response function with a Breit-Wigner line shape for parametrizing each strength from resonance. The energy, width, and probabilities of the strengths were chosen such that the simulated spectrum produced the best fit to the experimental data.

To quantify the goodness of the fits, χ^2 error was used as the measure. The χ^2 value of a fit is defined as,

$$\chi^2 = \frac{1}{N}\sum_{i=1}^{N}\left(\frac{y_{th}(x_i) - y_{exp}(x_i)}{\Delta y_{exp}(x_i)}\right)^2 \tag{5.1}$$

Here, x_i is the Q value, $y_{th}(x_i)$ and $y_{exp}(x_i)$ are the counts obtained from the simulation and from the data for the corresponding x_i, respectively. $\Delta y_{exp}(x_i)$ is the error in $y_{exp}(x_i)$, and N is the number of data points.

As it was described in Section 4.7, the maxima of a function can be obtained using BayesOpt. In this case, the aim was to maximize the inverse of χ^2-error of the fit. We have a black box function of the form $f(\mathbf{x})$, where $\mathbf{x}$ is a vector of all the parameters of the simulation, namely the positions, widths, amplitudes of the states, and $f(\mathbf{x})$ is the inverse of the χ^2-error of the fit obtained using these parameters. Hence, BayesOpt can be used in this situation.

In the first round of simulations, two strengths were input into the simulation and for the BayesOpt, a range for energies (in Q value), widths, and the intensity of these strengths, along with amplitude for the non-resonant background were given as bounds. These parameters were allowed to vary within these bounds for each iteration in BayesOpt and then the simulated spectrum was fitted to the data. For the BayesOpt routine, 50 exploration and 500 exploitation iterations were performed, with each iteration being a GEANT4 simulation with 100000 events. After the BayesOpt routine was complete, the fit with the least χ^2-error was obtained.

The Q value obtained on an event-by-event basis is shown in Figure 5.2 as data points with error bars. A global fit to the spectrum is shown as a red line. There is a broad structure between Q = -3.2 MeV and -2.2 MeV, which could also be interpreted as two peaks. This GEANT4 simulation demonstrates that even if there were two peaks in the broad structure above -3.4 MeV in Q value, the experimental resolution limits our ability to distinguish them. The asymmetric shape of the low-lying strength is due to the fact that low-energy protons traversing through the target lose different amounts of energy depending on where the reaction occurred inside the target. This low-lying strength is represented using a blue dashed line and it lies at 0.55 MeV above the threshold with a Breit-Wigner width of 0.11 MeV. There is a clear increase in intensity below Q=-3.4 MeV which is shown as a green dot-dashed line. This resonance lies at 2.22 MeV above the threshold with a width of 0.40 Mev and has been reported by previous experiments [30, 32, 34, 36, 37, 39]. The non-resonant background is shown as a black dotted line.

In order to find the error bars for the energies, the minimum value of χ^2, χ^2_{min} was stored and for each state, the energy was allowed to vary by small steps. The lower and upper bounds of the energy which produced a χ^2 value of $\chi^2_{min} + 1$ were taken as the 1σ error bars.

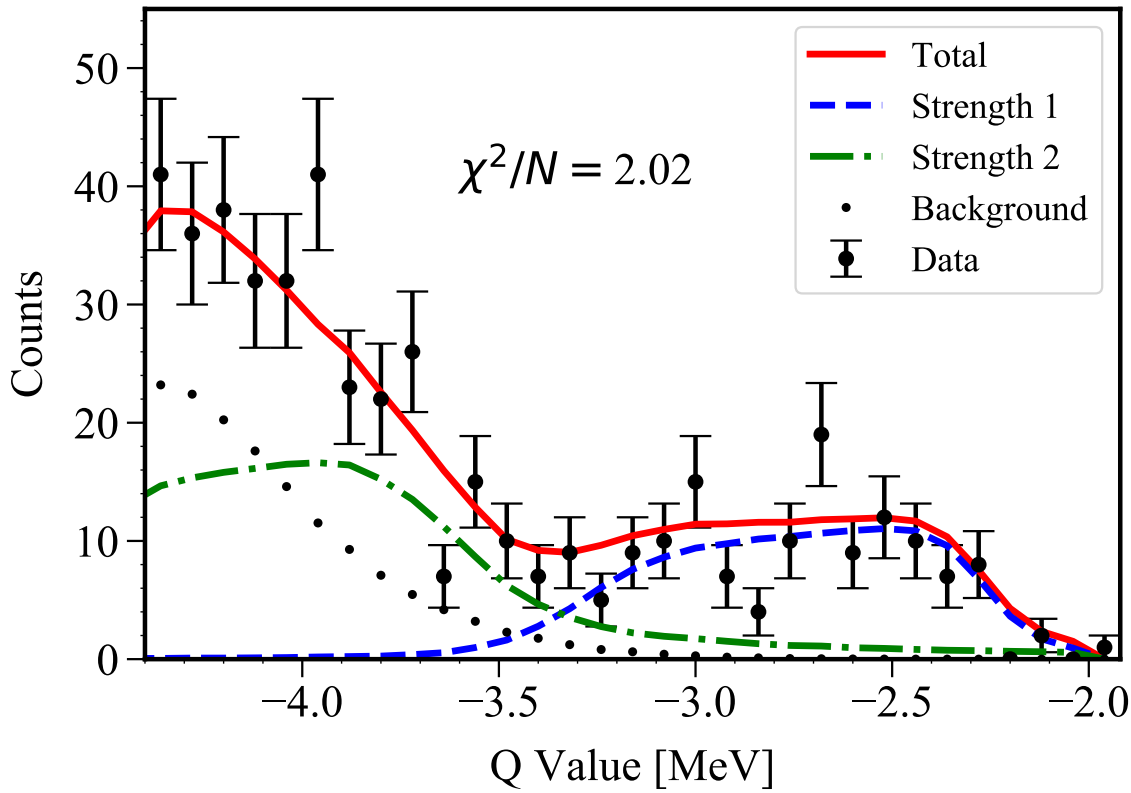

Figure 5.2: ^{13}Be Q-value spectrum obtained from ^{12}Be + d reaction. The data is shown as black points with statistical error bars. A global fit to the data obtained using Bayesian optimization is shown as a red line. Low-lying strength lying at 0.55 MeV above the threshold is denoted as a blue-dashed line. Strength at 2.2 MeV above the threshold is shown as a green dot-dashed line. The non-resonant background is shown as a black dotted line.

The same approach was carried out to find the error bars for the widths and is illustrated in Figure 5.3. The results are shown in Table 5.1.

5.3 Angular distributions

The angular distributions of the outgoing protons from the ^{12}Be(d,p) reaction give information about the spin and parity of the energy level of the transferred neutron. The reaction was analyzed in the distorted-wave Born approximation (DWBA) framework, with FRESCO [68]. The optical potential parameters were obtained from FRONT [48]. The disadvantage of this method is that it is very sensitive to the type of optical potentials used. In order to compensate for that ambiguity, we used different optical potentials and studied their sensitivity.

The solid angle ($d\omega$) of an object is defined as the ratio of the surface area (dA) of the segment of a sphere subtended by the object, to the square of the radius (r) of the sphere. It is given by,

$$d\omega = \frac{dA}{r^2}. \tag{5.2}$$

To calculate the solid angle covered by the YU detector, a sphere centered at the target position was considered, with the detector plane subtending this sphere. The solid angles were calculated for each ring. For the first 13 rings, it was calculated using the analytical formula given by Eqn. 5.3. For the last 3 rings, it was calculated numerically using the parameters from the drawing of the detector.

$$\Omega = 2\pi(\cos\theta_1 - \cos\theta_2). \tag{5.3}$$

Here, θ_1 and θ_2 are the polar angular ranges of the angular bin. The 2π factor comes from the entire azimuthal range of the detector. For the lowest-lying strength in energy above the threshold (strength 1 in Figure 5.2), the angular distribution was evaluated by dividing the data into three angular bins and the total counts were obtained for each bin so that we can see how the cross-section varies with the angle. The counts were then converted from the laboratory frame to the center of mass frame. The non-resonant background was

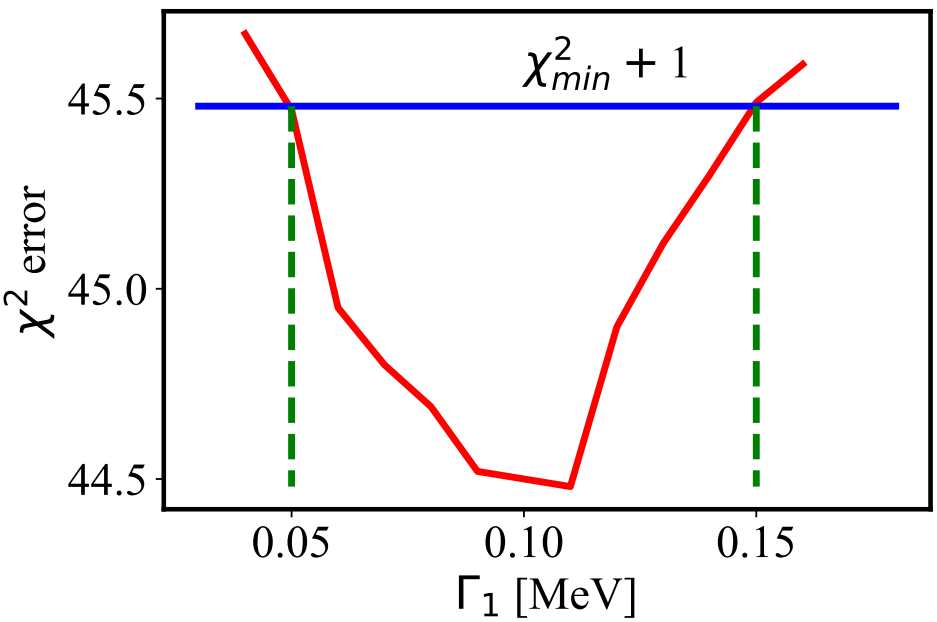

Figure 5.3: The width of strength 1 was varied from the optimum value (χ^2_{min})and the simulations were carried out and the data was fitted. The χ^2 values for these fits are plotted against the widths in red color. The blue horizontal line shows where the χ^2 value becomes $\chi^2_{min} + 1$. The corresponding widths were used as the 1σ confidence interval. It is shown as green dashed lines.

Table 5.1: A table showing the Q values and the Breit-Wigner widths of the two strengths in the continuum of ^{13}Be, obtained by fitting the Q-value spectrum of ^{12}Be + d reaction, using GEANT4 simulations and Bayesian optimization

Strength	Q value	Energy above threshold	Breit-Wigner width
1	$-2.75^{+0.08}_{-0.07}$	$0.55^{+0.08}_{-0.07}$	$0.11^{+0.04}_{-0.05}$
2	$-4.42^{+0.04}_{-0.05}$	$2.22^{+0.04}_{-0.05}$	$0.40^{+0.03}_{-0.04}$

subtracted from the data at this stage. Strength 2 was dominated by the non-resonant background and hence there were not enough statistics to divide the counts into different angular bins. After computing the ratio between the counts and the solid angle coverage for each bin, the resulting distribution was compared against calculations from FRESCO. Optical model calculations for the transfer reaction were calculated using Daehnick Global [46], Lohr-Haeberli, [47] and Perey-Perey [45] potentials for the deuteron-nucleus vertex, Koning and Delaroche [50] potential was used for the proton-nucleus vertex. The angular distributions of the protons coming the ^{12}Be(d,p)^{13}Be reaction were fitted with pure s,p, and d waves as well as mixtures of these waves namely, s and p, s and d, and p and d mixtures. The fits are shown in Figures 5.4, 5.5 and 5.6. The parameters used for the Lohr-Haeberli potential were radius, r=1.29 fm, diffuseness, a = 0.860 fm, and a spin-orbit term, with V_{SO} = 3.5 MeV. For the Daehnick-Global potential, r=1.17 fm, diffuseness, a = 0.773 fm, and V_{SO} = 3.122 MeV and that of Perey-Perey potential were, r=1.29 fm, a = 0.810 fm without a spin-orbit term.

When fitted with pure s, p, and d-waves, the *s*-wave component is the most sensitive to the different combinations of potentials, while *p* and *d* waves gave similar χ^2 values for the fits. Of the three waves, the p-wave fitted the data with the lowest χ^2 value in all the three combinations of the potentials. Mixtures of the waves gave an even lower χ^2-value compared to pure waves. A mixture of s and p waves fits data the best. This is in agreement with the results of Kondo et al. [37], Ribeiro et al. [43], and Corsi et al. [39]. With the Perey-Perey potential, the fit gave a mixture of 61% of s-wave and 39% of p-wave and with the Lohr-Haeberli potential, a mixture of 65% of s-wave and 35% of p-wave was obtained. The next best fit was with a mixture of s and d waves. All three potential combinations gave similar results. The Perey-Perey potential gave an 89% of s-wave and 11% of d-wave while the Daehnick Global and Lohr-Haeberli potentials gave a mixture of 91% of s-wave and 9% of d-wave. A mixture of p and d waves had zero contribution from the d wave and was completely a p wave with all the three potentials. This leads to the conclusion that if the low-lying strength is a mixture of two resonances, then it can be a mixture of either s and p waves or a mixture of s and d waves. The inferences are summarized in Table 5.2.

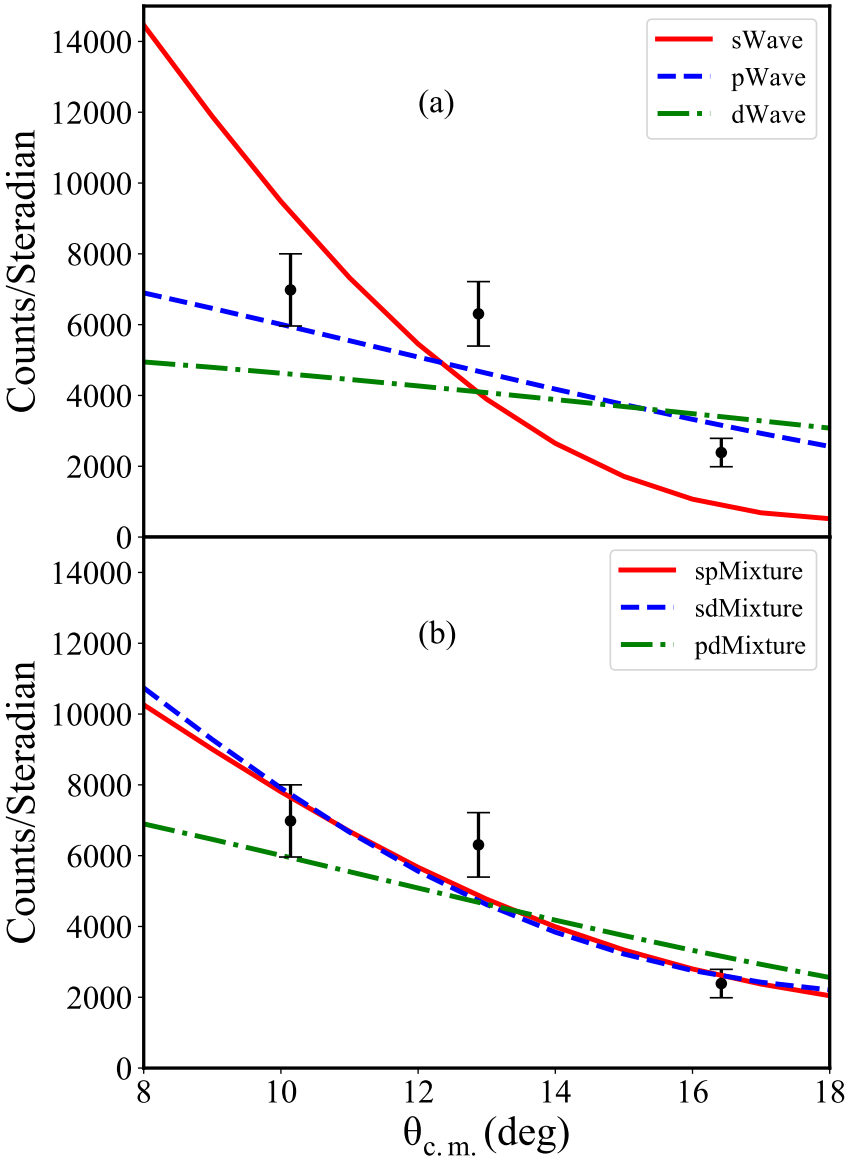

Figure 5.4: An angular distribution plot fitted with DWBA calculations performed using FRESCO with Daehnick Global potential as the deuteron vertex potential and Koning-Delaroche potential as the proton vertex potential. Plot (a) shows data fitted with pure waves and plot (b) shows data fitted with a mixture of waves.

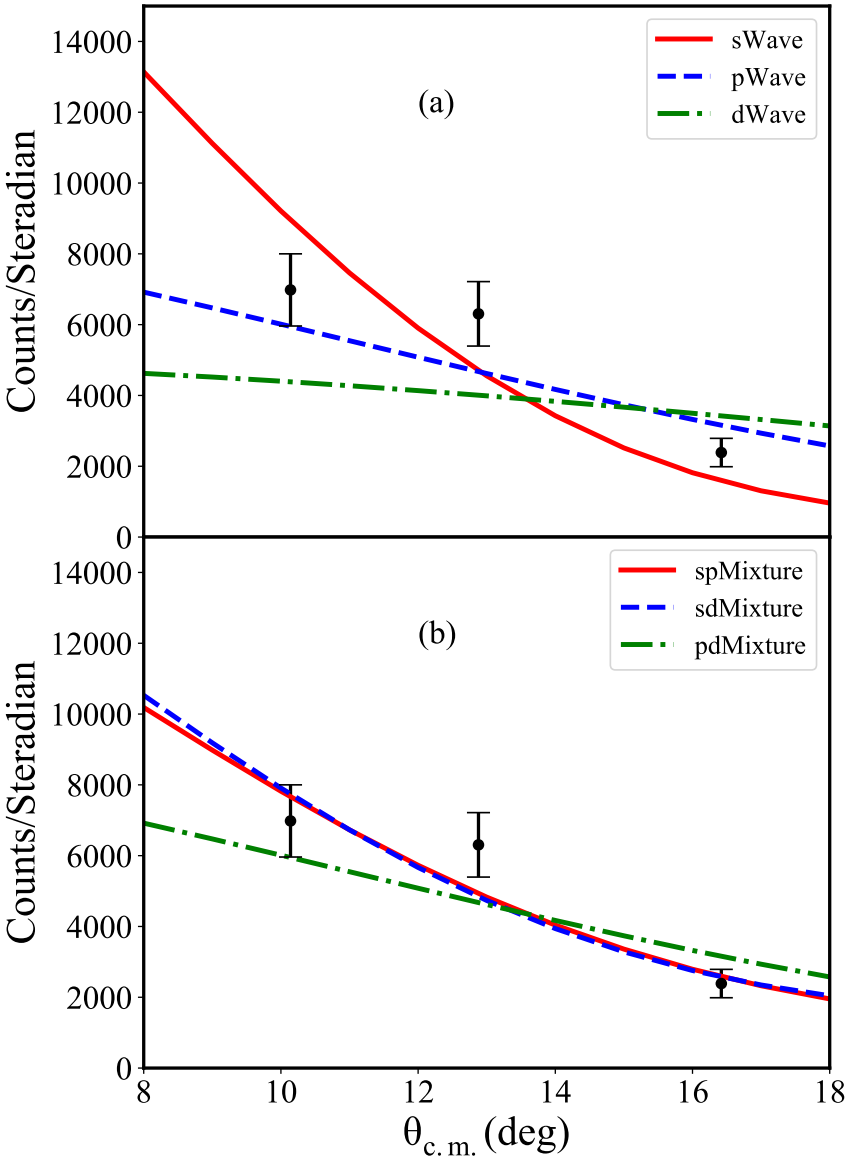

Figure 5.5: An angular distribution plot fitted with DWBA calculations performed using FRESCO with Lohr-Haeberli potential as the deuteron vertex potential and Koning-Delaroche potential as the proton vertex potential. Plot (a) shows data fitted with pure waves and plot (b) shows data fitted with a mixture of waves.

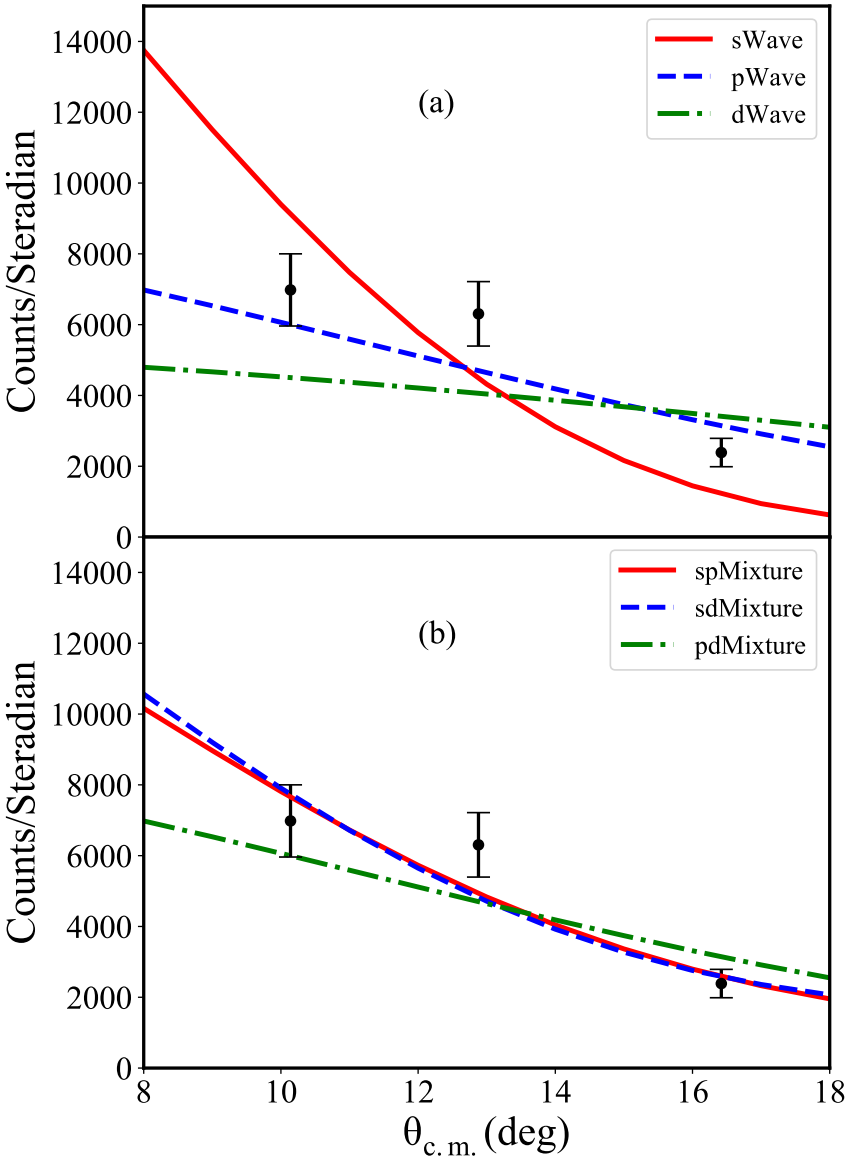

Figure 5.6: An angular distribution plot fitted with DWBA calculations performed using FRESCO with Perey-Perey potential as the deuteron vertex potential and Koning-Delaroche potential as the proton vertex potential. Plot (a) shows data fitted with pure waves and plot (b) shows data fitted with a mixture of waves.

Table 5.2: The fit parameters for the angular distribution obtained from the DWBA calculations performed using FRESCO with Daehnick Global, Lohr-Haeberli, and Perey-Perey potentials as the deuteron vertex potential and Koning-Delaroche potential as the proton vertex potential.

Wave/Mixture	**Fraction 1**	**Fraction 2**	χ^2	χ^2/N
Daehnick Global and Koning-Delaroche Potentials				
s wave	-	-	24.82	12.41
p wave	-	-	7.9	3.95
d wave	-	-	17.68	8.84
$s+p$ mixture	$0.66^{+0.02}_{-0.07}$ s	$0.34^{+0.07}_{-0.02}$ p	3.2	3.2
$s+d$ mixture	$0.91^{+0.01}_{-0.025}$ s	$0.09^{+0.025}_{-0.01}$ d	3.85	3.85
$p+d$ mixture	$1.00_{-0.05}$ p	$0.00^{+0.05}$ d	7.9	7.9
Lohr-Haeberli and Koning-Delaroche Potentials				
s wave	-	-	10.09	5.45
p wave	-	-	7.92	3.96
d wave	-	-	19.53	9.77
$s+p$ mixture	$0.65^{+0.06}_{-0.09}$ s	$0.35^{+0.09}_{-0.06}$ p	2.97	2.97
$s+d$ mixture	$0.91^{+0.01}_{-0.04}$ s	$0.09^{+0.04}_{-0.01}$ d	3.35	3.35
$p+d$ mixture	$1.00_{-0.06}$ p	$0.00^{+0.06}$ d	7.92	7.92
Perey-Perey and Koning-Delaroche Potentials				
s wave	-	-	17.02	8.51
p wave	-	-	7.59	3.79
d wave	-	-	18.5	9.25
$s+p$ mixture	$0.61^{+0.04}_{-0.085}$ s	$0.39^{+0.085}_{-0.04}$ p	2.95	2.95
$s+d$ mixture	$0.89^{+0.01}_{-0.005}$ s	$0.11^{+0.005}_{-0.01}$ d	3.44	3.44
$p+d$ mixture	$1.00_{-0.04}$ p	$0.00^{+0.04}$ d	7.59	7.59

5.4 Interpretation of the Results

For further interpretation, the results from five previous experiments were compared with the data. To study ^{13}Be, Kondo et al. [37], Aksyutina et al. [38], and Corsi et al. [39] performed neutron knockout reactions on ^{14}Be. Ribeiro et al. [43] performed a proton knockout from ^{14}B and Randisi et al. [32] carried out the same reaction in addition to the breakup of ^{15}B. Only resonances or virtual states up to ~ 2 MeV above the neutron threshold are considered for comparison. Both Kondo et al. and Corsi et al. have reported a virtual s-wave state and a p-wave resonance. Ribeiro et al. reported a low-lying s-wave resonance and have used a lower-lying p-wave resonance in their analysis using data from Kondo et al. [37]. Randisi. et al. reported low-lying s- and d-wave strengths. All these experiments have either reported two low-lying strengths in the energy range of 0 MeV to 1 MeV above the neutron threshold, and a higher-lying d-wave in their analysis. But, Aksyutina et al. have reported only one low-lying state below the ~ 2 MeV ($\frac{5}{2}^+$) resonance which is an s-wave resonance.

To compare our data with the results that have reported two low-lying strengths, strength 1 was assumed to be an unresolved combination of two resonances, or of a resonance and a virtual state, and they were named strengths 1a and 1b. The angular distribution fits using a mixture of waves were used to quantify this division. The amplitudes of both the strengths (strengths 1 and 2) and the non-resonant background were obtained from the fit using BayesOpt performed in Section 5.2. The amplitude of strength 1 was then convolved with the relative intensities obtained from the angular distribution fit using Perey-Perey and Koning-Delaroche potentials. Combining the information from both the BayesOpt fit and the angular distributions, amplitudes were given for three states. For comparing with results from Aksytuina et al., the amplitudes were directly used from the fit in Section 5.2. The positions and widths for these states were used from these experiments and GEANT4 simulations were performed using these inputs. The simulated spectrum was then scaled to the data. Bayesian optimization was not carried out in this part of the analysis.

A fit to the data using results from Randisi et al. is shown in Figure 5.7. Here, an s-fraction of 0.89 and a d-fraction of 0.11 were used. Similarly, a fit is shown in Figure 5.8 using the results from Ribeiro et al. where they have reported low-lying p- and s-wave strengths.

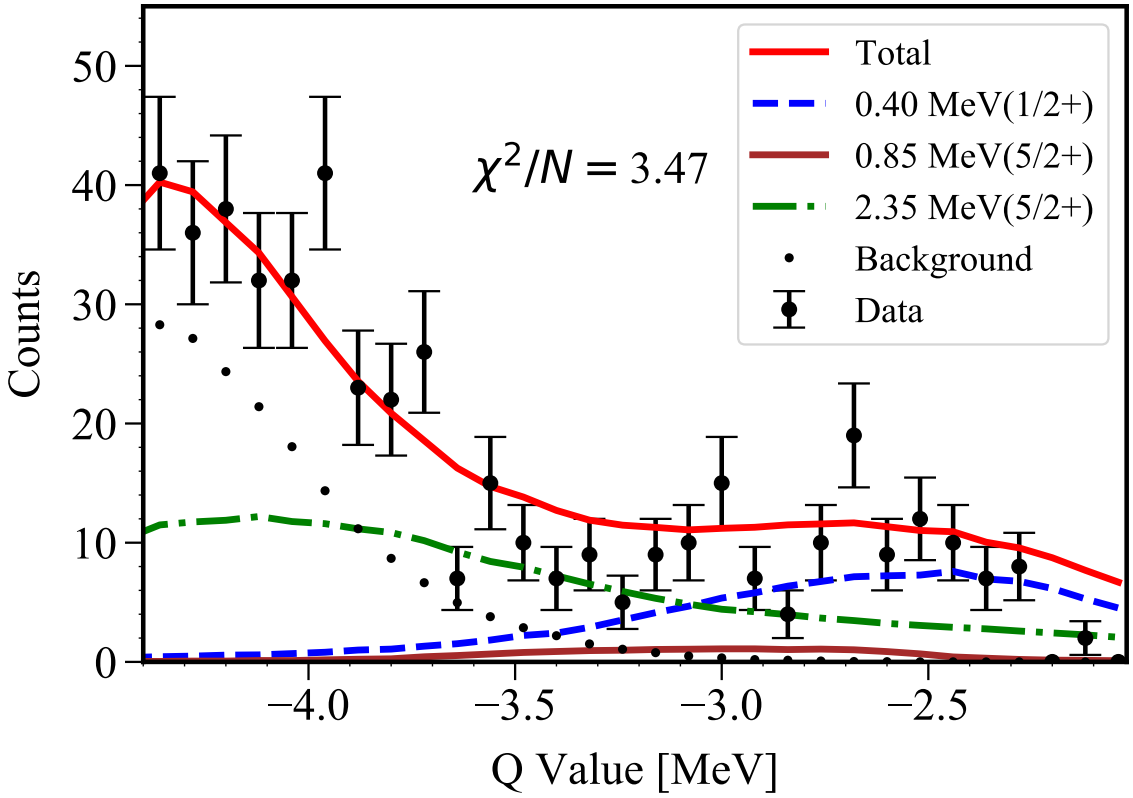

Figure 5.7: Data fitted with GEANT4 simulations with energy and widths obtained from Randisi et al. [32]. The amplitudes of the states were used from the angular distributions which were 89% of s wave and 11% of d wave.

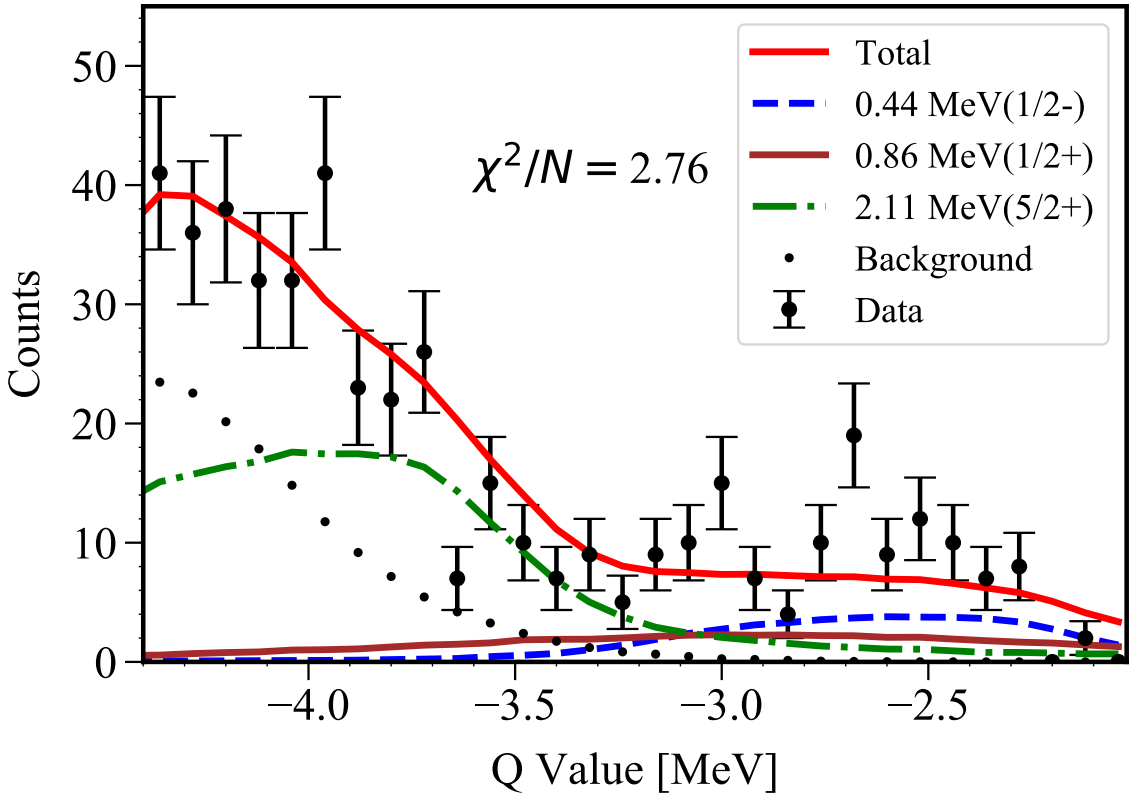

Figure 5.8: Data fitted with GEANT4 simulations with energy and widths obtained from Ribeiro et al. [43]. The amplitudes of the states were used from the angular distributions which were 39% of p wave and 61% of s wave.

Kondo et al and Corsi et al. have reported a virtual s-wave state. To compare their results with our data, the line shape for a virtual state was implemented in the GEANT4 simulations using Eqn. 5.4 [69]. The fits are shown in Figures 5.9 and 5.10.

$$\frac{d\sigma}{dE} \sim k \left[\frac{1}{\alpha^2 + k^2}\right]^2 \left[\cos(ka) - \frac{\alpha}{k}\sin(ka)\right], \tag{5.4}$$

where, $\alpha = \sqrt{2mE_B}$, E_B is the binding energy of the nucleus, a is the scattering length, and k is momentum. The results from Aksyutina et al. was used to fit the data with just two strengths as shown in Figure 5.11.

The fits using values from both Ribeiro et al. and Corsi et al. give similar χ^2 values and they are the lowest of all the five. Aksyutina et al. placed the well-known $\frac{5}{2}^+$, $\sim$ 2 MeV state at 1.95 MeV above the threshold and it differs by around 300 keV from this analysis. The widths reported by Kondo et al. and Randisi et al. for the same state are 2.4 MeV and 1.5 MeV, respectively. They are too large to agree with our data thus giving higher χ^2 values. As a next step, BayesOpt can be used to repeat these studies by letting the amplitudes for the strengths as free parameters instead of using them from the angular distributions but keeping the energies and widths of the states from the experiments. The results from the interpretation are summarized in Table 5.3.

5.5 Discussion

A Q-value spectrum of ^{13}Be was measured by performing neutron transfer using the ^{12}Be(d,p)^{13}Be reaction experiment. The low-lying strength in the continuum of ^{13}Be was exposed in this measurement. The Q-value spectrum was modeled using GEANT4 simulations and fitted using Bayesian optimization and the energies and widths of two strengths were obtained. The results from this experiment agree with all the previous experiments about the $\frac{5}{2}^+$ state around 2 MeV above the neutron threshold. In our case, we find the energy of that state to be 2.22 MeV above the threshold and width of 0.40 MeV. A low-lying strength was found to be at an energy of 0.55 MeV above the threshold.

A three-point angular distribution for the strength close to the threshold was fitted using DWBA calculations. Three different deuteron-vertex optical model potentials give similar

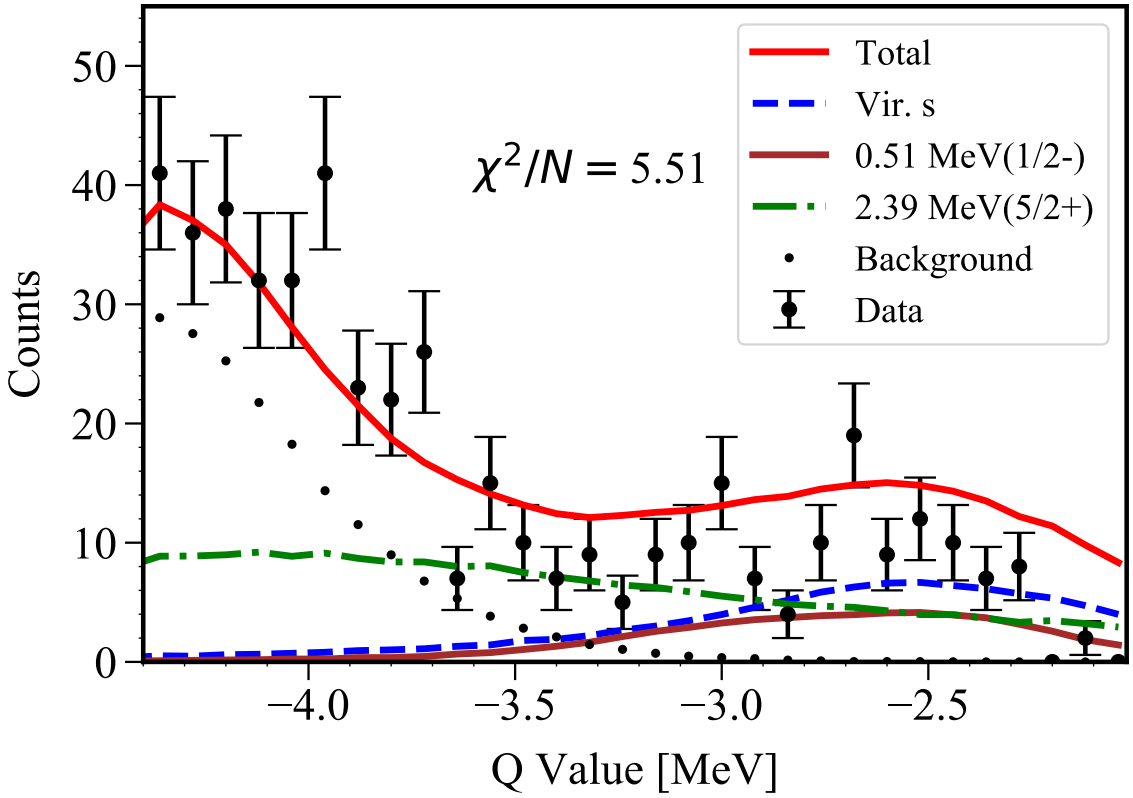

Figure 5.9: Data fitted with GEANT4 simulations with energy and widths obtained from Kondo et al. [37]. The amplitudes of the states were used from the angular distributions which were 61% of s wave and 39% of p wave.

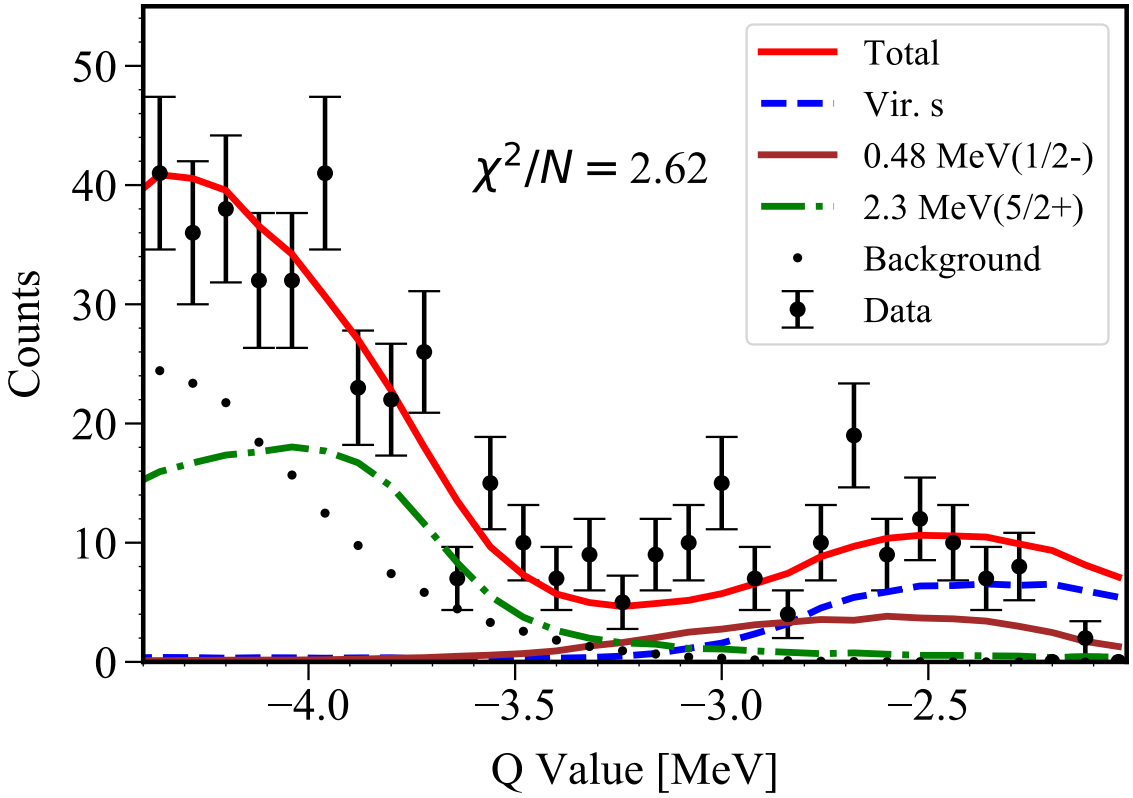

Figure 5.10: Data fitted with GEANT4 simulations with energy and widths obtained from Corsi et al [39]. The amplitudes of the states were used from the angular distributions which were 61% of s wave and 39% of p wave.

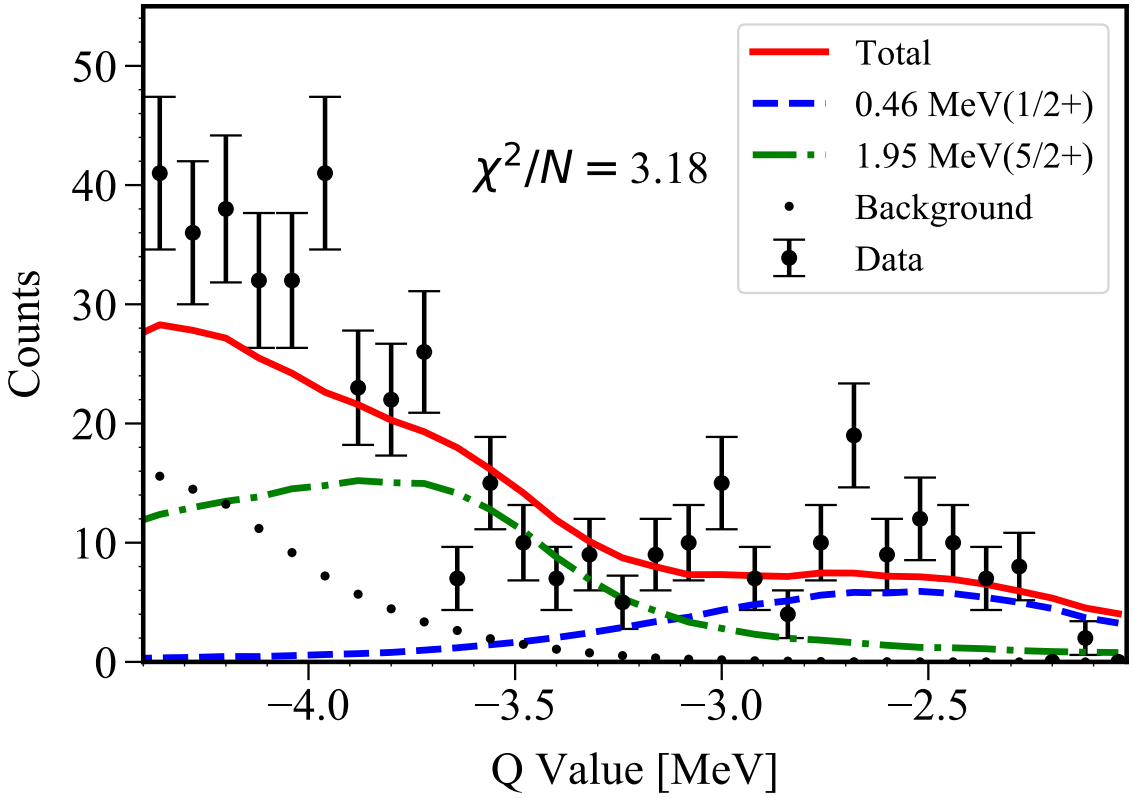

Figure 5.11: Data fitted with GEANT4 simulations with energy and widths obtained from Aksyutina et al. [38]. The amplitudes of the states were used directly obtained from BayesOpt results.

Table 5.3: The results from fitting the data with the results from experiments performed by Kondo et al. [37], Aksyutina et al. [38], Randisi et al. [32], Ribeiro et al. [43], and Corsi et al. [39], compared with the results from this work. E_r (MeV) denotes the energy in the case of resonance, and a_s (fm) is the scattering length in the case of a virtual s-wave state. Γ_r (MeV) is the width of the resonance. The amount of strengths 1a and 1b used in each of the fits are shown in percentages.

Experiment	Strength 1a			Strength 1b			Strength 2		χ^2/N
	a_s or E_r	Γ_r	Percentage	E_r	Γ_r	Percentage	E_r	Γ_r	
Kondo	-3.4	-	61%	0.51 ($\frac{1}{2}^-$)	0.45	39%	2.39 ($\frac{5}{2}^+$)	2.4	5.51
Aksyutina	0.46 ($\frac{1}{2}^+$)	0.75	100%	-	-	-	1.95 ($\frac{5}{2}^+$)	0.5	3.18
Randisi	0.40 ($\frac{1}{2}^+$)	0.80	89%	0.85 ($\frac{5}{2}^+$)	0.30	11%	2.35 ($\frac{5}{2}^+$)	1.50	3.47
Ribeiro	0.44 ($\frac{1}{2}^-$)	0.39	39%	0.86 ($\frac{1}{2}^+$)	1.70	61%	2.11 ($\frac{5}{2}^+$)	0.4	2.77
Corsi	-9.2	-	61%	0.48 ($\frac{1}{2}^-$)	0.20	39%	2.3 ($\frac{5}{2}^+$)	0.40	2.62
This work	0.55 ($\frac{1}{2}^-$)	0.11	100%	-	-	-	2.22	0.40	2.02

results except for pure s-wave. A s- and p-wave mixture, and an s- and d-wave mixture are not greatly affected by the choice of the deuteron vertex potential. The low-lying strength was found to be either one p-wave resonance or a combination of s- and p-, or s- and d-waves, both dominated by s-wave.

After comparing our data with the results from five other experiments, it was found that our results agree best with Corsi et al. and Ribeiro et al., even though they differ in the ordering and the shape of the low-lying states. Ribeiro et al. have reported a low-lying p-wave and an s-wave above it, and Corsi et al. have reported a virtual s-wave and a p-wave at higher energy above the threshold. There is less agreement with Randisi et al and Aksyutina et al. due to the difference in the width and the position of the $\frac{5}{2}^+$, ~ 2 MeV resonance, respectively, whereas disagreement with Kondo et al. because of the considerable contrast in the width of that resonance.

Chapter 6

Study of (d, n) Reactions Using NEXT

Similar to how we can study neutron transfer reactions by probing the protons from (d, p) reactions, proton transfer reactions can be studied by detecting the neutrons coming from (d, n) reactions. This is a challenging area since neutrons being neutral do not interact through charge with other particles unlike protons and other charged particles through scattering. Neutrons when interacting with nuclei of other materials can lead to the emission of charged particles or gamma rays, which can be turned into electrical signals and detected. In this chapter, we will talk about the development of a high-resolution time-of-flight neutron detector called NEXT and how it was used to study a well-known transfer reaction $^{20}\mathrm{Ne(d,n)}^{21}\mathrm{Na}$.

6.1 Introduction to Neutron Detectors

There are mainly two ways by which neutrons interact with matter. First, neutrons can elastically scatter with a nucleus of an atom, thereby transferring energy and the recoiling nucleus, in turn, ionizes that atom. If the material is correctly chosen, the emitted photons can be detected. This method is most efficient in light nuclei like hydrogen and helium. Secondly, neutrons can cause a nuclear reaction when interacting with certain materials and produce protons, gamma rays, and fission fragments, which can be detected. These are the common mechanisms used in neutron detectors. The detector material can be solid, liquid,

or gas for either of these methods. The recoil-type detection method will be focused on in this chapter.

In a recoil-type interaction, only the first interaction is measured and a neutron need not deposit its full energy during this event. Hence, the time-of-flight (TOF) method is often used to measure the kinetic energy of the neutron. The TOF is defined as the time it took for the neutron to travel the distance between the source and the detector. Excellent timing precision is crucial in this case. For example, the TOF range for a 1-10 MeV neutron for a distance of 1 m is 72-23 ns. A common material used for recoil-type detection is a plastic scintillator. Due to their fast response (in the range of nanoseconds), they are good for fast-neutron detection. The term light yield of a scintillator defines the number of photons generated per unit energy deposited by a particle moving in the medium. Different particles interact differently inside the scintillator to produce photons. Neutrons scatter elastically with the protons in a scintillating material and can transfer up to 100% of their energy compared to 28% for recoiling ^{12}C nuclei in organic scintillators. The recoiling protons excite the scintillator molecule and result in ionization and the emission of visible light. Photomultiplier tubes connected to the end of scintillator detectors can convert this light to electrical signals whose height depends on the energy of the recoiling nucleus.

Another factor to be considered is the gamma-ray sensitivity of neutron detectors. Nuclear materials usually emit more gamma rays than neutrons and the detector material should be properly chosen so that they can be distinguished, especially when studying a reaction. Gamma rays interact with electrons and transfer energy through Compton scattering. This can give rise to high-energy electrons which can produce ionization in the detector which will result in signals similar to those from neutrons. Due to the difference in the ionization densities of the recoiling protons and electrons in the scintillating medium, they produce different amounts of light though they have the same initial energy. Protons show a lower scintillation response than electrons for a particular energy.

In gas-filled detectors, the electrons scattered by gamma rays will deposit energy through a larger distance and hence take more time compared to a neutron interaction, and hence they can be differentiated. In organic scintillators, both neutrons and gamma rays have comparable detection sensitivity. Hence, the pulse height of both spectra is similar and is

not enough to distinguish between them. But certain scintillators respond differently to neutrons and gamma rays and this can be utilized in detecting neutrons in the presence of gamma-ray background. The difference lies in the shape of scintillation pulse due to recoiling protons (in the case of neutrons), and Compton scattered electrons (due to gamma rays). A method called pulse shape discrimination (PSD) [70] can be used to differentiate these signals.

In organic scintillators, fluorescence arises from excitations and transitions in the energy levels of organic molecules. In molecules, the electrons lie in hybridized orbitals called spin singlet (S) or triplet state (T). After interaction with radiation, molecules absorb kinetic energy, and the electrons get excited and go to higher excited states (S_N or T_N) and their lifetimes are different. There are two decay components in fluorescence, the main component decaying exponentially, giving a prompt fluorescence, and a slower component with the same wavelength causing a delayed emission. De-excitation from S_1 (first excited singlet state) gives rise to the fast component. The T_1 states are more mobile in organic molecules and they collide with each other and form singlet states [71]. $T_1 + T_1 \rightarrow S_0 + S_1$. Hence, the lifetime of T_1 and the rate of T_1T_1 collisions determine the lifetime of delayed emissions. The recoiled protons originating from neutron radiation travel a shorter distance and give rise to a higher number of triplets when compared to electrons resulting from the gamma-ray interactions which travel a longer range. Hence, neutron-induced pulses will have a higher level of delayed emission compared to the pulses produced by the gamma interaction as shown in Figure 6.1a. The PSD parameter is calculated by taking the ratio of the signal charge accumulated under the tail of the pulse to the total charge accumulated. Neutron-induced pulses will have a higher tail-to-total ratio because of the presence of more delayed emission. This technique is called the charge comparison method (CCM) [72]. This helps in distinguishing neutrons from gammas.

The figure of merit, FOM of the PSD of a neutron detector is defined as [71],

$$FOM = \frac{S}{\delta_{neutron} + \delta_{gamma}}, \tag{6.1}$$

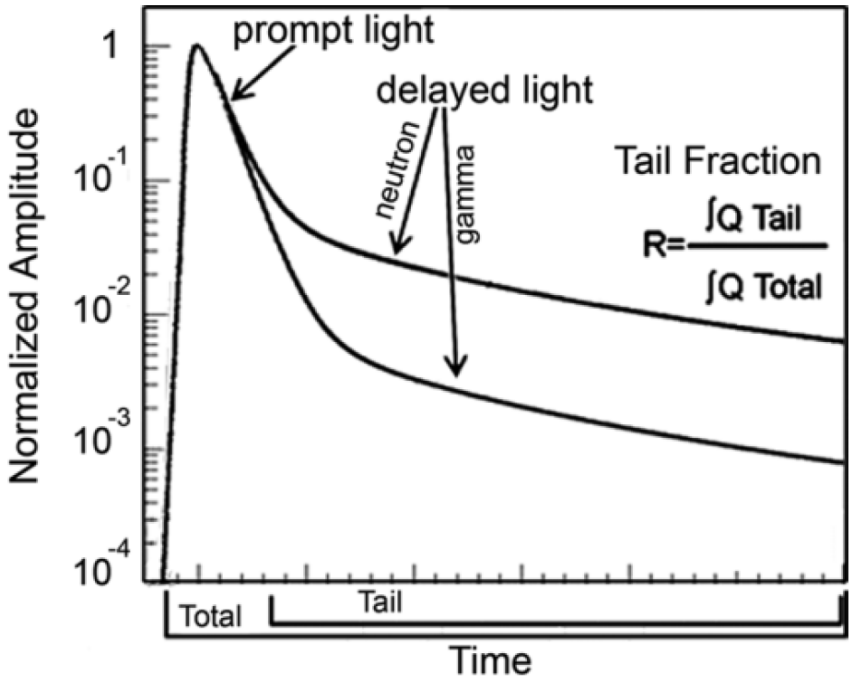

(a) Pulse shape of scintillation light from neutrons and gammas

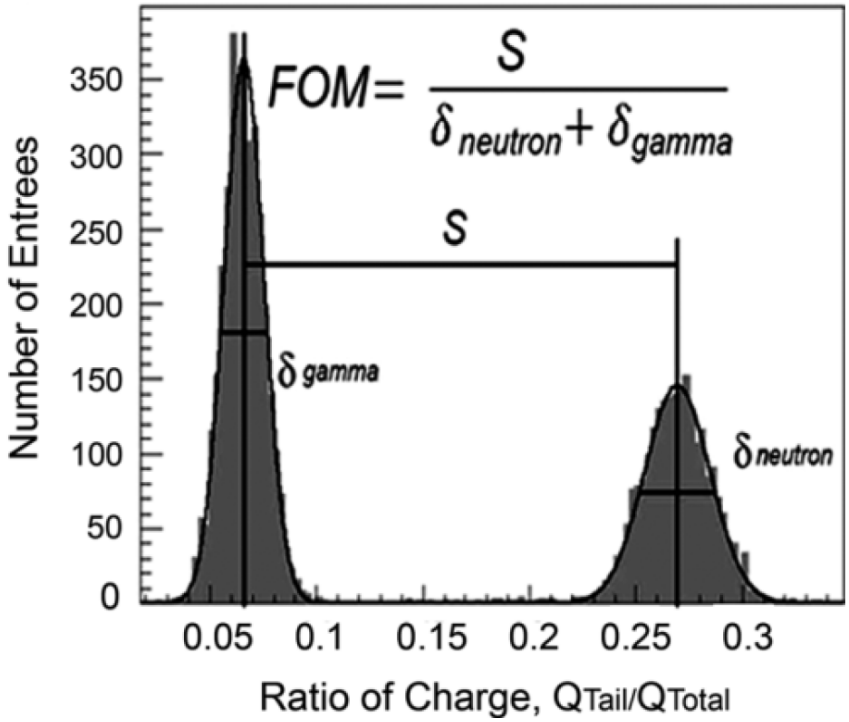

(b) Figure of merit

Figure 6.1: Calculation of figure of merit for a plastic scintillation detector. Figure adapted from [71].

where S is the separation between the neutron and gamma peaks, and $\delta_{neutron}$ and δ_{gamma} are the FWHM of the neutron and gamma peaks respectively, as given in Figure 6.1b. Higher FOM implies better discrimination between the neutrons and the gammas and hence materials with a higher FOM are preferred for building neutron detectors.

6.2 NEXT Detector

The disadvantages of plastic scintillator neutron detectors are the poor resolution from not knowing the interaction point for thick detectors and the huge background from gamma rays from interactions with the target and decay of RIBs. The Neutron dEtector with Xn (multi neutron) Tracking or NEXT is a high precision segmented detector to study neutrons from beta-delayed neutron emission and proton transfer reactions. During a transfer reaction experiment, gamma rays cause a considerable amount of background. The NEXT detector shows good PSD capabilities so as to identify this background. It is a time-of-flight detector, meaning, the energy of the neutron is found from its time-of-flight.

The energy resolution ΔE for a time-of-flight detector is given by,

$$\frac{\Delta E}{E} = \sqrt{\left(\frac{2\Delta T}{T}\right)^2 + \left(\frac{2\Delta L}{L}\right)^2} \tag{6.2}$$

Here, ΔT is the uncertainty in the time-of-flight of the neutron, T, and ΔL is the uncertainty in the path length, L. Hence, decreasing the uncertainty in the estimation of the neutron interaction point reduces ΔL and gives a better energy resolution. So, thick detectors lack good resolution even though they give good efficiency for neutron detection.

The NEXT detector array comprises segmented modules, each made of a pulse shape discrimination (PSD) plastic scintillator with both ends connected to position-sensitive photodetectors. The PSD plastic from Eljen (EJ-276) helps in neutron-gamma discrimination for reducing the background. The overall dimensions of each module are 48 mm $\times$ 50.8 mm $\times$ 254 mm which consists of 4 $\times$ 8 segments as shown in Figure 6.2a. Each segment measures 6 mm $\times$ 12.7 mm $\times$ 254 mm [73]. These segments are polished on all the sides and they are covered with 3M^{TM} Enhanced Specular Reflector (ESR) to enhance

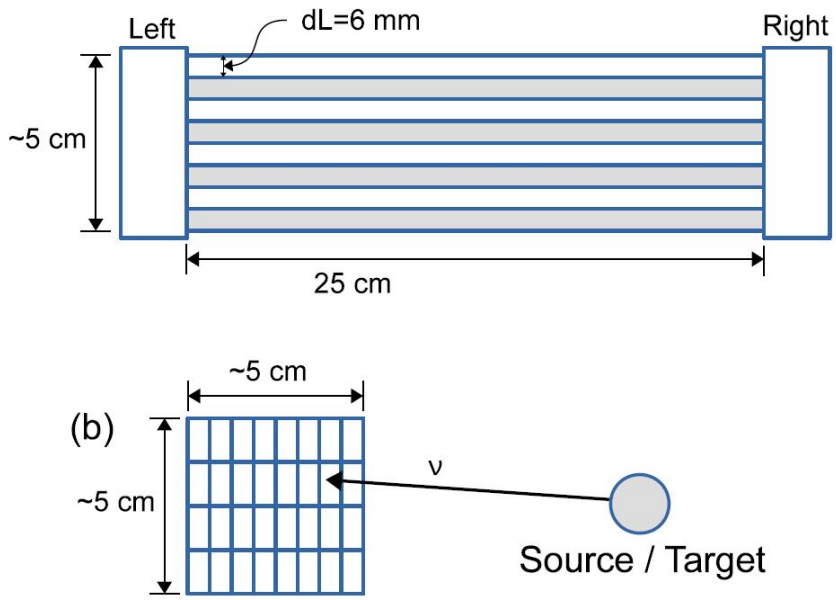

(a)

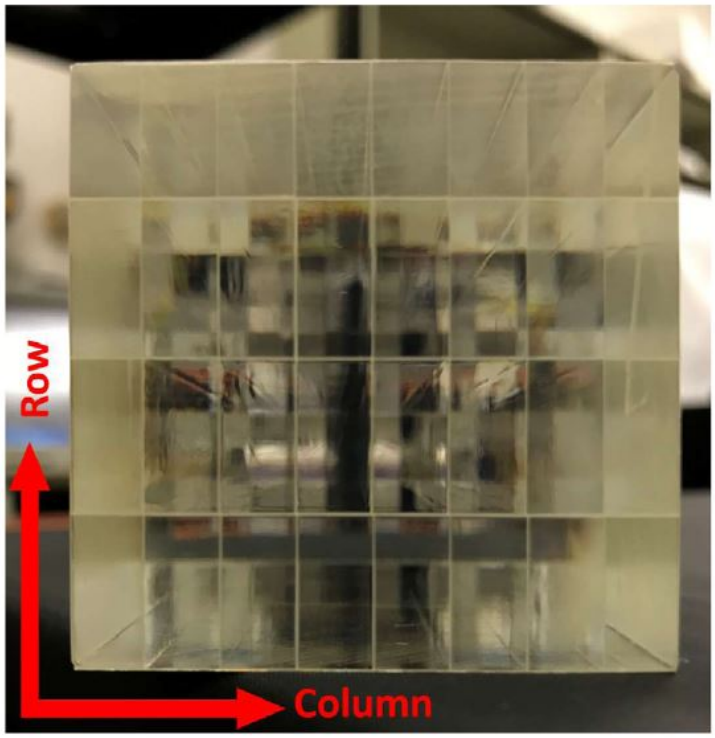

(b)

Figure 6.2: (a) shows the dimensions of a NEXT module. There are eight segments in the direction of neutrons. (b) shows a cross-sectional view of stacked scintillator crystals before they are wrapped. Figures adapted from [73].

the light yield. The ESR layer has 98% reflectivity in the visible spectrum. These segments are stacked with an air gap in between them as shown in Figure 6.2b. The segmentation in the detector gives a better position and hence a better energy resolution (around 15 keV for a 1 MeV neutron) without sacrificing the detection efficiency. The scintillators are then coupled to Hamamatsu H12700A position-sensitive photomultiplier tubes (PSPMTs) on both ends. These PSPMTs have an 8×8 segmentation with a readout for each anode and dynode. A Vertilon PSPMT Anger Logic Interface board was used to reduce the number of channels from 64 position signals to four anode readouts and a single readout for the last dynode. The scintillation position can be calculated using the four resistive network signals at the corners with the Anger Logic. These four anode signals for position and a single dynode signal for timing and PSD analysis are then recorded using 14-bit, 250 MHz XIA Pixie-16 digitizers. These digitizers record an analog-to-digital converter (ADC) trace for each PMT voltage signal and write it to the disk. 14-bit digitizers have a dynamic range of 0 to 16383 channels. The trace amplitude is determined by the optical properties of the scintillator, the PMT gain, and voltage bias. To measure the entire amount of light produced by an event, an integral of the trace is calculated and this is termed the trace integral or QDC.

6.2.1 Neutron-gamma discrimination

To reduce the gamma-ray background we need good neutron-gamma discrimination capability for the detector. Using a ^{252}Cf source, the scintillation light from both the neutrons and gamma rays was recorded by NEXT, and a PSD plot (Figure 6.3) was obtained. In this way, neutron and gamma-ray events can be separated. The range of integration for calculating the tail-to-total ratio was varied and studied to optimize the figure of merit using a ^{252}Cf source. The EJ-276 gives good neutron-gamma discrimination with a figure of merit of 1.2 ± 0.06 in the QDC range of 80000-90000.

6.3 ^{20}Ne(d, n)^{21}Na at ReA6 NSCL

Proton capture reactions which are denoted as (p,γ) are of significant interest in nuclear astrophysics. By adding protons, to an atomic nucleus continuously, new elements can be

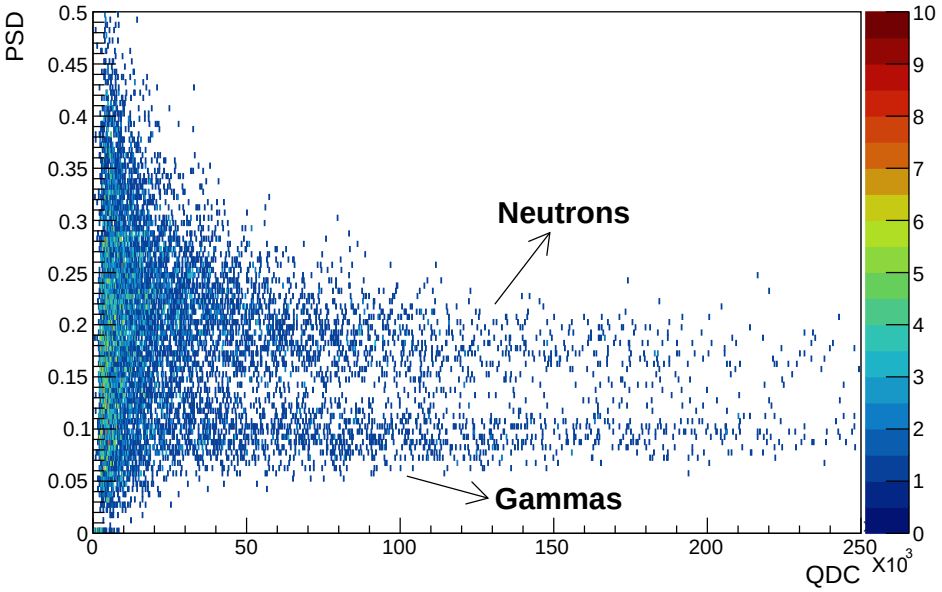

(a)

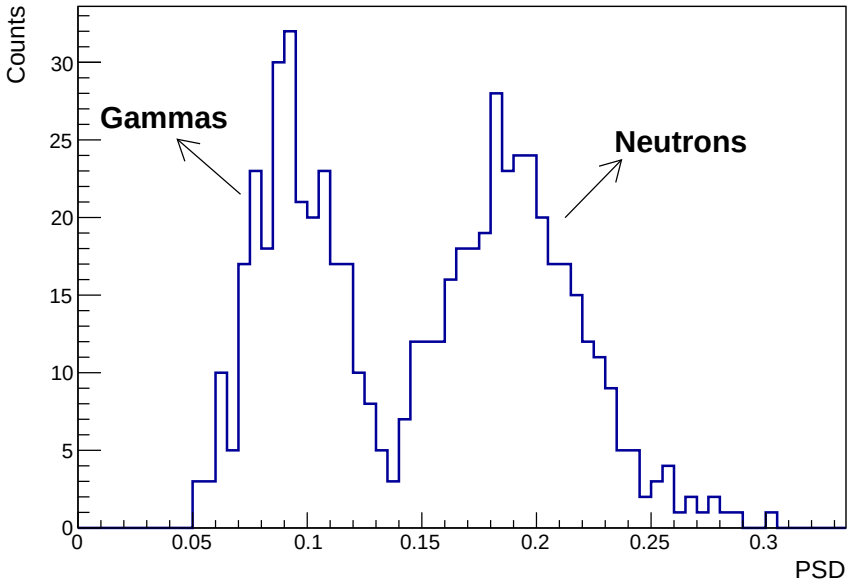

(b)

Figure 6.3: (a) shows PSD-QDC histogram obtained from a NEXT module for a ^{252}Cf source. The two bands from neutrons and gammas can be clearly distinguished. (b) shows projection of the PSD-QDC histogram in the QDC range of 80000-90000. A FOM of 1.2±0.06 was obtained using the criterion shown in Figure 6.1b.

produced, while emitting gamma rays. This is one of the mechanisms behind nucleosynthesis in stars and supernovae.

The most important energy sources in main sequence stars are the p-p chain and the CNO cycle by which hydrogen nuclei are fused into helium. Additionally, in larger-mass some second-generation stars, the Ne-Na cycle is also of importance in hydrogen burning [74]. The sequence is given by,

$$^{20}\mathrm{Ne}(p,\gamma)^{21}\mathrm{Na}(\beta^{+}\nu)^{21}\mathrm{Ne}(p,\gamma)^{22}\mathrm{Na}(\beta^{+}\nu)^{22}\mathrm{Ne}(p,\gamma)^{23}\mathrm{Na}(p,\alpha)^{20}\mathrm{Ne}. \tag{6.3}$$

This reaction cycle is not as important as the CNO cycle in terms of an energy source because of its slower reaction rates but it is important for the nucleosynthesis of neon and sodium. The ^{21}Ne produced during this cycle is of interest in the helium-burning in starts and also acts as a neutron source for the synthesis of heavier elements.

Making a direct measurement of (p,γ) reactions at astrophysically significant energies is incredibly difficult owing to the tiny cross-sections. Hence, we resort to indirect measurements by performing proton transfer instead of proton capture. Reactions like (^{3}He,d) and (d,n) are the usual alternatives but they have technical limitations. The former requires an enriched ^{3}He target which is very rare while the latter requires, the detection of neutrons, which is difficult because they have no charge, unlike protons. We decided here to use the (d,n) reaction technique.

6.3.1 Experiment Setup

The $^{20}\mathrm{Ne}(\mathrm{d},\mathrm{n})^{21}\mathrm{Na}$ reaction experiment was conducted at the ReA6 (Re-Accelerated) beam facility at the National Superconducting Cyclotron Laboratory (NSCL). This facility is unique in the sense that it provides low-energy radioactive ion beams by stopping them after being produced in-flight and then reaccelerating them to desired energies. The first step in the beam production is the collision of fast (80 MeV/u), continuous, stable, heavy-ion beams from the coupled-cyclotrons with the production target. The fragments from the primary reaction are separated in-flight from the primary ion beams. The high-energy rare-isotope fragments are then transported to a He-gas cell for thermalization to reach an energy

of 60 keV/u and then sent as continuous beams into a beam cooler buncher (BCB), where they are bunched and ejected as pulsed beams. The singly-charged ions are injected into the EBIT breeder. EBIT or electron beam ion trap is one of the main components of the ReA facility. It converts singly charged ions to higher-charge states by stripping off electrons prior to injecting them into the linear accelerator. The electron beam present in the EBIT creates highly charged ions (HCI) by electron-impact ionization and traps them by providing radial confinement through its space charge. The ions progress through a multi-harmonic buncher (MHB) and RF linear accelerator before being accelerated up to 6 MeV/u depending on the Q/A ratio [75].

Alternatively, ions of stable isotopes can be accelerated by injecting them from an external ion source in the EBIT. The beam production mechanism is illustrated in Figure 6.4.

Beam Characteristics

The total time period of the EBIT signal for this experiment was 130 ms with an ON period of 30 ms and an OFF period of 100 ms. When the EBIT was ON, the beam was bunched at 80.5 MHz. The beamline also delivered the beam in RF/5 frequency which was in 62.1 ns intervals. A gate and delay generator was used to make an AND gate of the EBIT signal and the RF buncher to create the trigger signal for the NEXT in order to avoid the NEXT from being triggered when the EBIT is OFF. This is shown in Figure 6.5. Signals from the EBIT, RF/5, and the EBIT-gated RF are shown. This long-enough gap between the subsequent pulses was crucial to measuring the TOF of slower neutrons. For this experiment, the TOF of a neutron with energy of 1 MeV was 43.35 ns.

6.3.2 Measurements using NEXT

The experiment was conducted in inverse kinematics. It was a commissioning run for two different kinds of detectors for neutron detection; the ORNL Deuterated Spectroscopic Array (ODeSA) and the UTK high resolution, NEXT detector modules. Our involvement focused on the latter detector and eleven modules were used. A major goal of this experiment was to commission NEXT for (d,n) reaction studies. The ReA RF microstructure poses a challenge

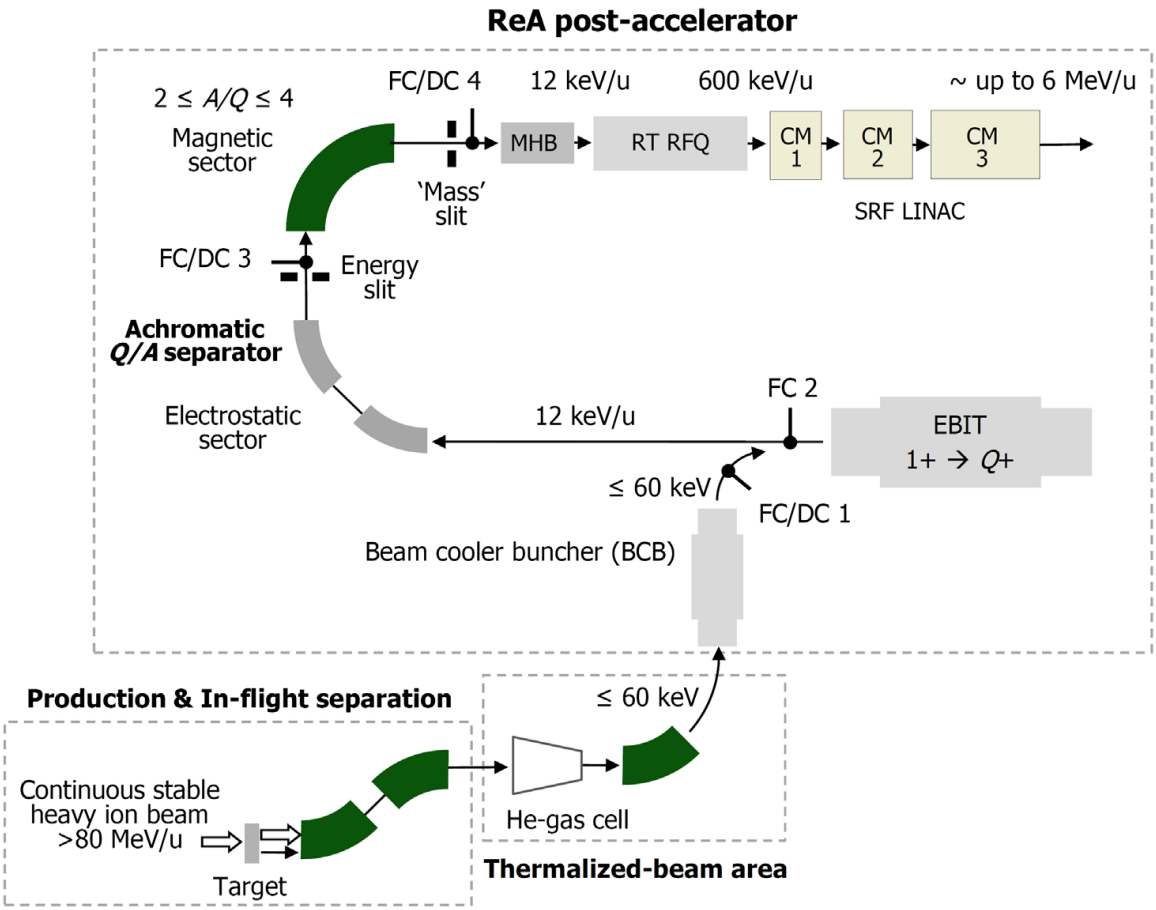

Figure 6.4: Schematic of the beam production mechanism at the ReA facility, NSCL. Figure adapted from [75].

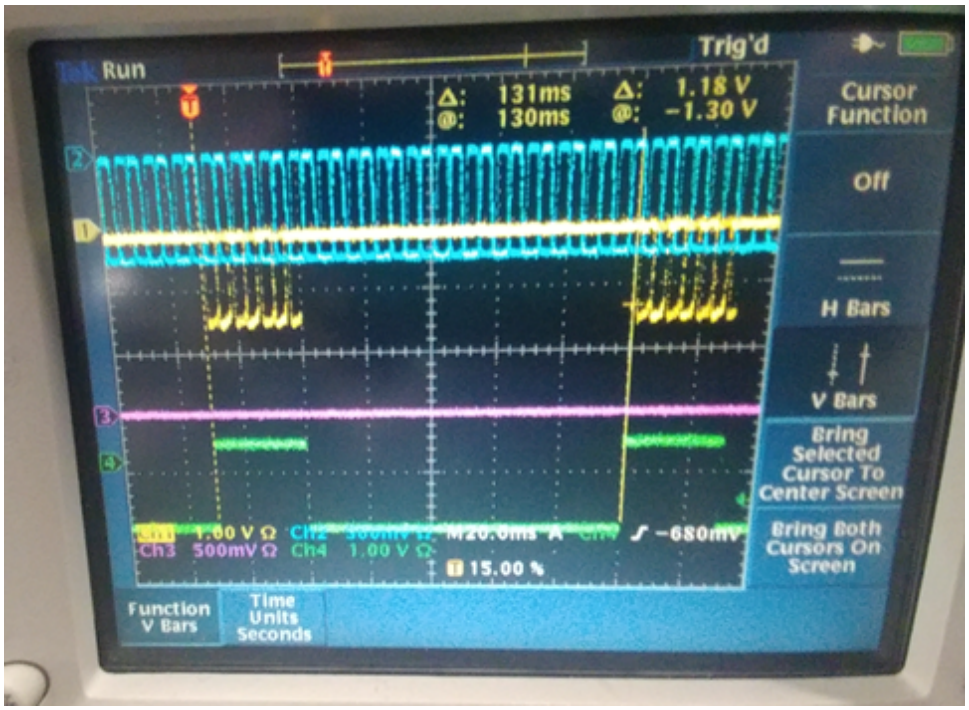

(a)

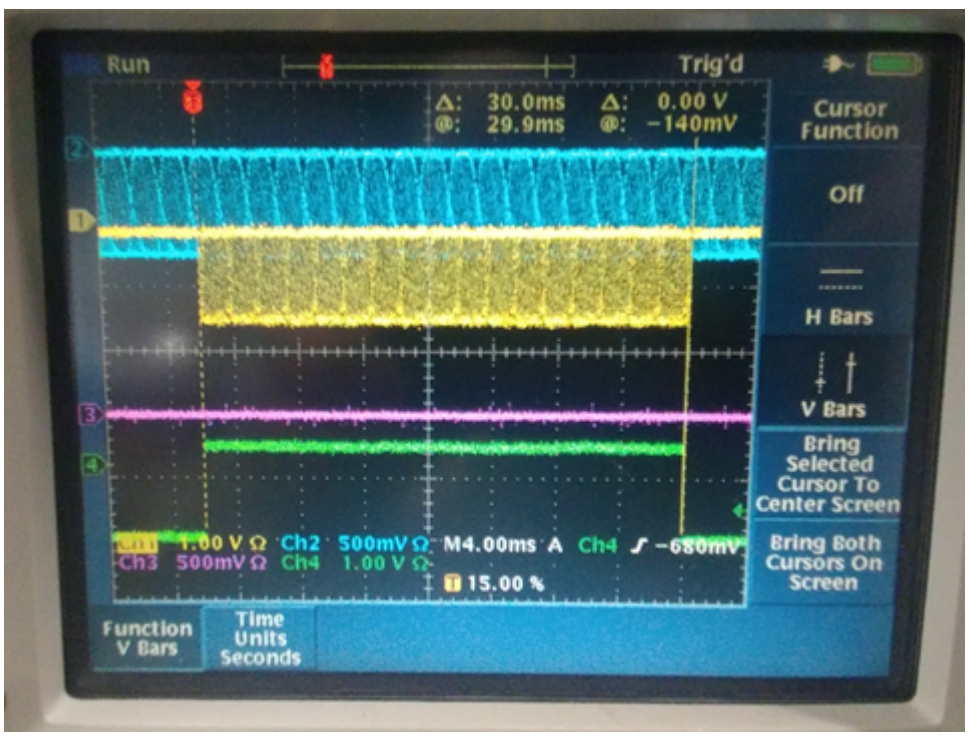

(b)

Figure 6.5: Signals from the EBIT (green), RF (cyan), and EBIT-gated RF (yellow). The EBIT-gated RF signal was used as the start trigger for the experiment. (b) shows a time period of 130 ms for the EBIT signal

when it comes to neutron TOF spectroscopy. 12.4 ns bunches are converted into 62.1 ns bunches with a harmonic buncher but this is not perfect and there is an approximately 5% leakage at 12.4 ns (termed as satellite bunches). This can create a wrap-around effect in neutron TOF. We decided to perform the well-known ^{20}Ne(d,n)^{20}Na reaction to demonstrate the detector technology for future (d, n) reaction studies by comparing the results with the known levels and strengths from the literature. The data from this experiment can also be used to fully assess and quantify different background sources from the experimental setup itself.

A stable beam of ^{20}Ne at 10.2 MeV/u was delivered by the ReA6 beamline to a C_2D_4 target of thickness 0.5 mg/cm^2 or 2 mg/cm^2 (Figure 6.7) were used. The neutrons from the $^{20}\mathrm{Ne(d,n)}^{21}\mathrm{Na}$ were detected using 11 NEXT modules as shown in Figure 6.6. Two HAGRiD (Hybrid Array of Gamma-Ray Detector) detectors were also used to detect the gamma rays from different reactions. The front faces of the NEXT detectors were placed at an average distance of 50 cm from the target and the array covered a laboratory angular range of 90° to 165°. The HAGRiD detectors were placed very close to the target chamber at 0° and 90° in the laboratory frame, to maximize the geometric efficiency while reducing the scattering of the neutrons into the neutron detectors.

6.3.3 Compton Scattering and Detector Light Response

When $\gamma-$rays enter a plastic scintillator, they can be scattered by the electrons present in the plastic via Compton scattering. The energy of the scattered γ-ray is given as,

$$E^{'} = \frac{E}{1 + (E/m_e c^2)(1 - \cos\theta)}, \tag{6.4}$$

where E is the energy of the incident γ-ray, m_e is the electron mass, and θ is the scattering angle. From this equation, we can see that maximum energy is transferred to the electrons by the γ-rays when they backscatter ($\theta = 180°$), and this maximum energy is given by,

$$E^{'}_{max} = \frac{E}{(2E/m_e c^2) + 1}. \tag{6.5}$$

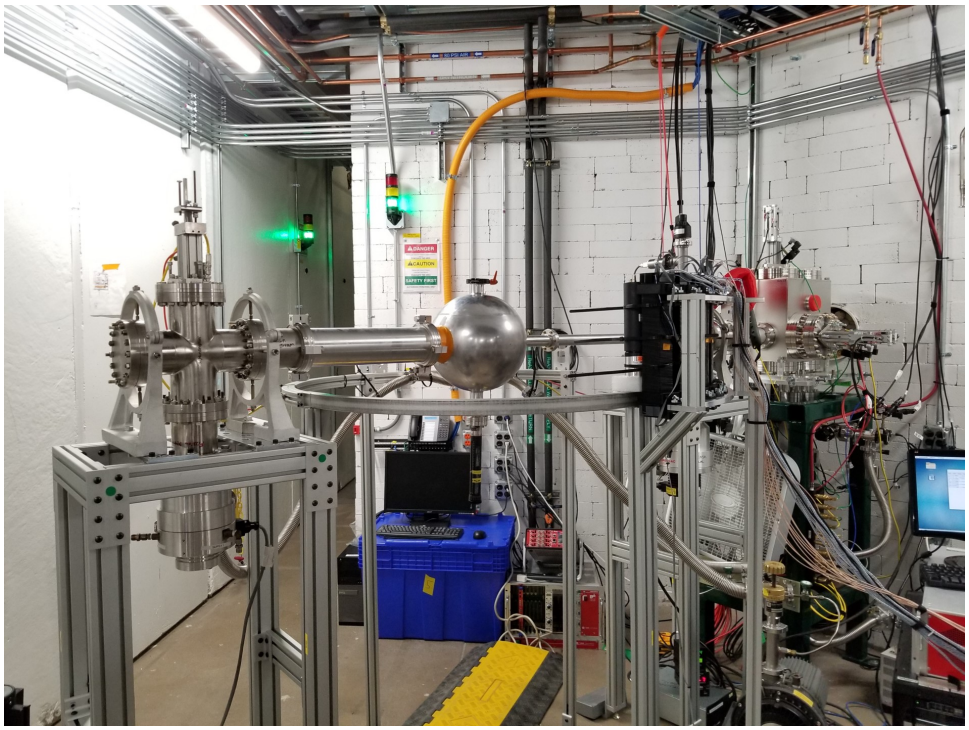

(a)

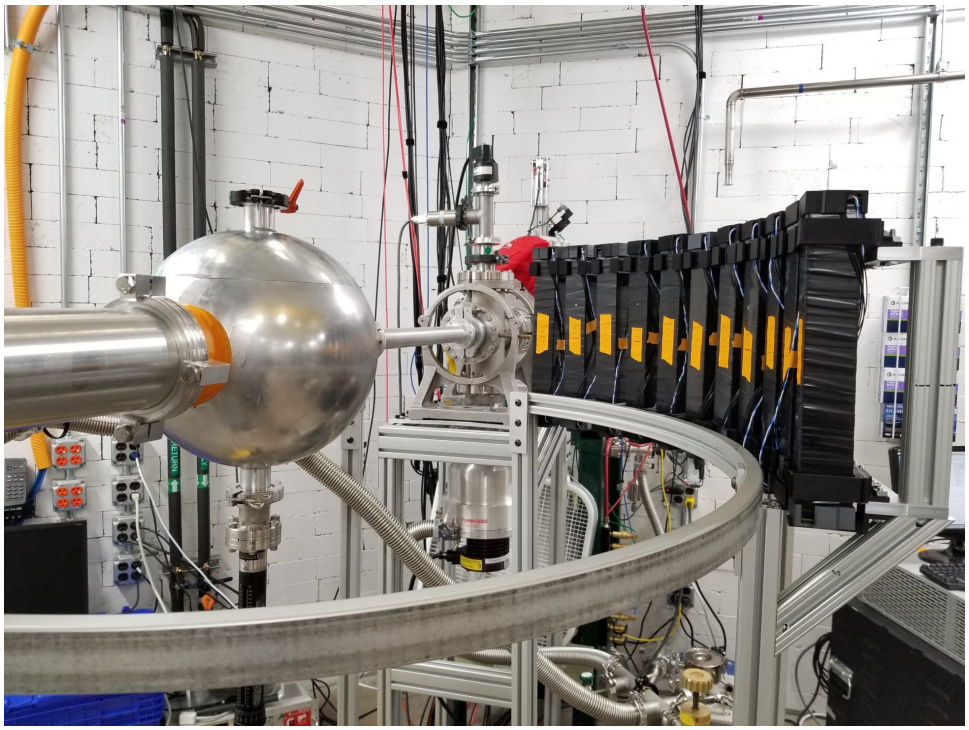

(b)

Figure 6.6: (a) shows the experiment setup with reaction chamber carrying the target connected to the beamline and the beam stop Faraday cup. (b) shows eleven NEXT modules covering a laboratory angular range of 90° to 165°.

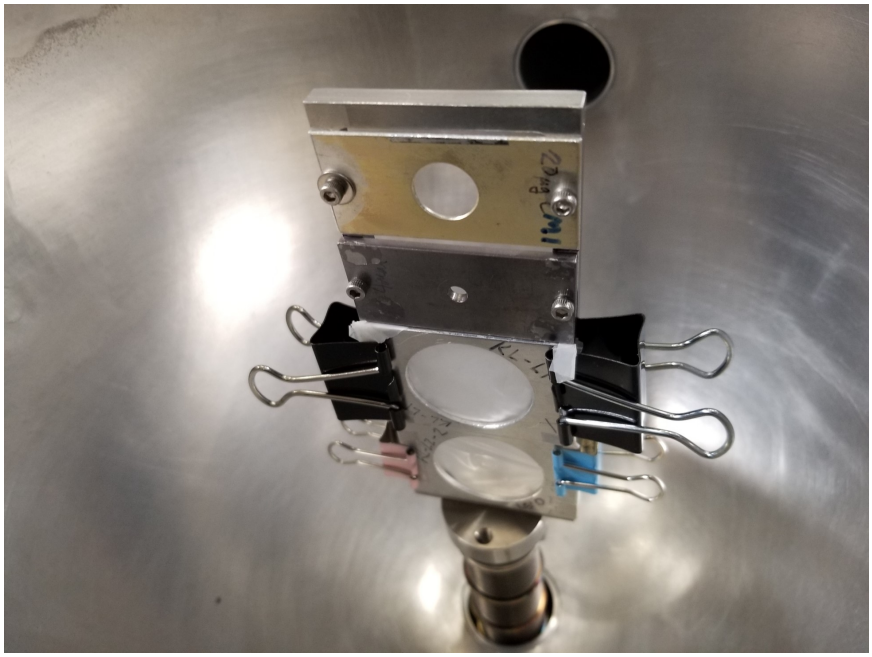

Figure 6.7: A photograph from inside the target chamber showing two C_2D_4 targets of thicknesses 0.5 mg/cm^2 and 2 mg/cm^2. A collimator was also used to take the data without the target.

When maximum energy is imparted to the electrons by the γ-rays, a feature called the Compton edge is seen. All the γ-rays which scatter at angles less than 180° are emitted at lower energies and the Compton-scattered recoiling electrons produce scintillation light thus creating a distribution of light yield and this gives rise to the Compton plateau. In the case of ^{137}Cs, which emits γ-rays of energy 662 keV, the Compton edge is seen at 478 keV as obtained from Equation 6.5. Figure 6.8 shows a QDC spectrum obtained from a NEXT module for a ^{137}Cs source.

The light yield of a scintillator depends on the type of interacting particle, and it is reported in terms of the electron equivalent ($eVee$). 1 $eVee$ of light yield is defined as the amount of scintillation light produced by an electron with an energy of 1 eV [55].

To combine the data from detectors made of different scintillation materials, the electron-equivalent light response of that detector needs to be calibrated. This is typically achieved using $\gamma-$ ray sources and in this case, a ^{137}Cs source was used. The $\gamma-$ rays emitted by the source after entering the plastic scintillator scatter with the electrons in the material and the recoiling electrons produce scintillation light.

6.3.4 Preliminary Analysis and Results

In neutron time-of-flight (TOF) spectroscopy, the energy of the neutron is calculated using the TOF of the neutron from the source to the detector and the distance between them. In the non-relativistic regime, the kinetic energy (T) of the neutrons can be calculated using the equation,

$$T = \frac{1}{2} M_n \left(\frac{d}{t}\right)^2, \tag{6.6}$$

where M_n is the mass, t is the TOF, and d is the flight-path distance of the neutron. In this study, we are interested in neutrons with energy less than 10 MeV and hence we can use the non-relativistic equation. A trigger signal is required to provide a reference for the neutron TOF. In this experiment, the EBIT gated RF signal was used as the trigger or start signal. An event is recorded only when there is a global validation which means that the start trigger along with the left and right signals from the detector are recorded. This helps in getting rid of the uncorrelated background. Since neutrons can be detected throughout

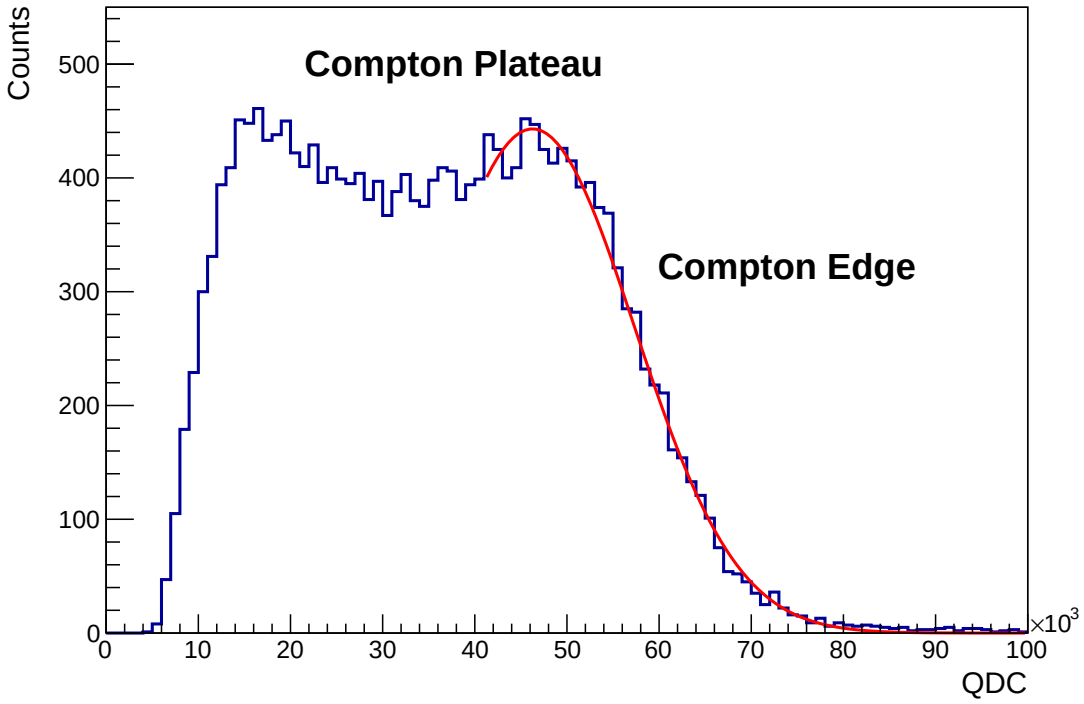

Figure 6.8: QDC histogram with a ^{137}Cs source showing Compton plateau and Compton edge.

the length of the detector, the flight path of the detected neutron may not be horizontal. Hence the TOF of the neutron is calculated by taking an average of the time recorded from both the ends of the detector.

$$TOF = \frac{t_R + t_L}{2} \tag{6.7}$$

Here we assume that the high-resolution time of the start signal is offset to zero. t_R and t_L are the times taken by the neutron to reach the detector from the source plus the scintillation light to be detected by the right and left ends of the detector, respectively. Depending on the individual channel offset of the digitizer, there can be a timing offset in the TOF. The offset is found using the prompt gamma flash. The gamma rays are produced when the beam strikes the target, which then travels to the detector with constant speed giving us a reference. Any TOF less than that of gamma flash is nonphysical and should be rejected. The prompt peak is fitted using a Gaussian function and is aligned to the time taken by the gamma rays to reach the detector.

The PSD-QDC spectrum from the reaction data is shown in Figure 6.9a. It can be seen that there is a huge background from the gamma rays and it is bleeding into the neutron PSD region for lower QDC values. In order to discriminate the neutrons from the gammas, the PSD-QDC histogram was projected onto ranges of QDCs. These spectra were then fitted with a convolution of two Gaussian functions. A projection in the QDC range of 200×10^3 to 220×10^3 as shown in Figure 6.9b. The minima of the fit between the gamma and neutron peaks were then identified for each of the spectra and these points were used to draw a gate on PSD which could be used to differentiate neutron and gamma signals efficiently.

The Compton edges of all the modules were obtained during the experiment using a ^{137}Cs source and it was used to gain-match the detectors so that the data could be combined. The TOF-QDC spectrum obtained from a single detector module is shown in Figure 6.10a. The position of the gamma flash in TOF was corrected to account for the time it takes for the gamma rays to reach the detector from the reaction chamber. The prompt gamma flash from the reaction is denoted as [c]. It was shifted to the end of the time range to account for the wraparound effect. The satellite bunches arising due to leakage from the harmonic buncher are denoted as [a]. These occur at 12.4 ns intervals. An anomalous peak (labeled as [b]) is visible at a TOF of 42.5 ns. This is due to gamma rays coming from the beam stop

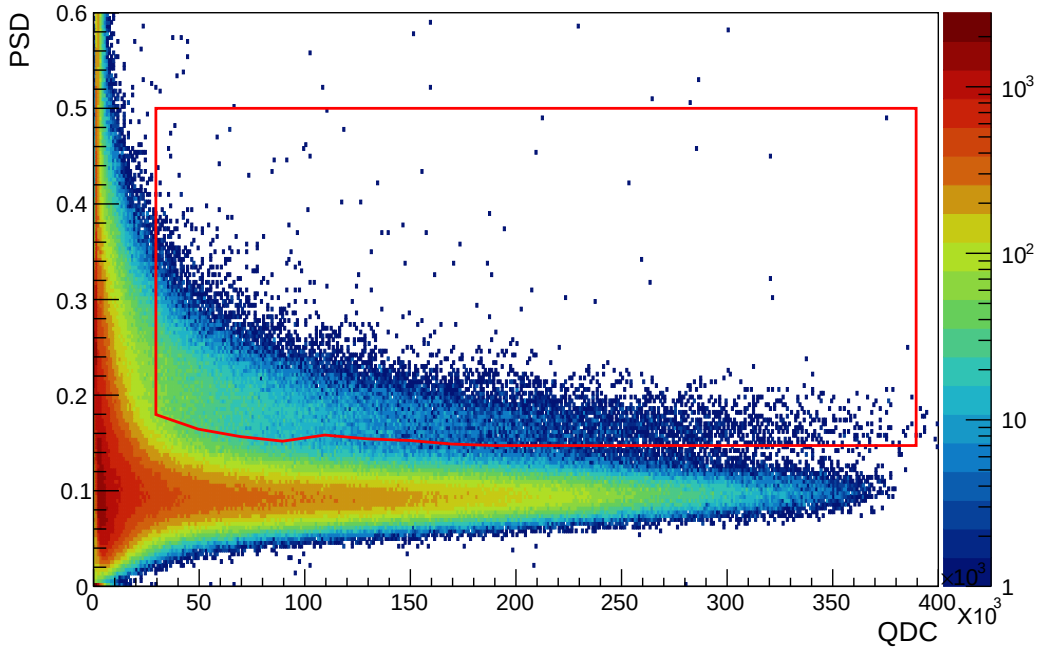

(a) PSD-QDC histogram for detector module 10 obtained from the reaction data.

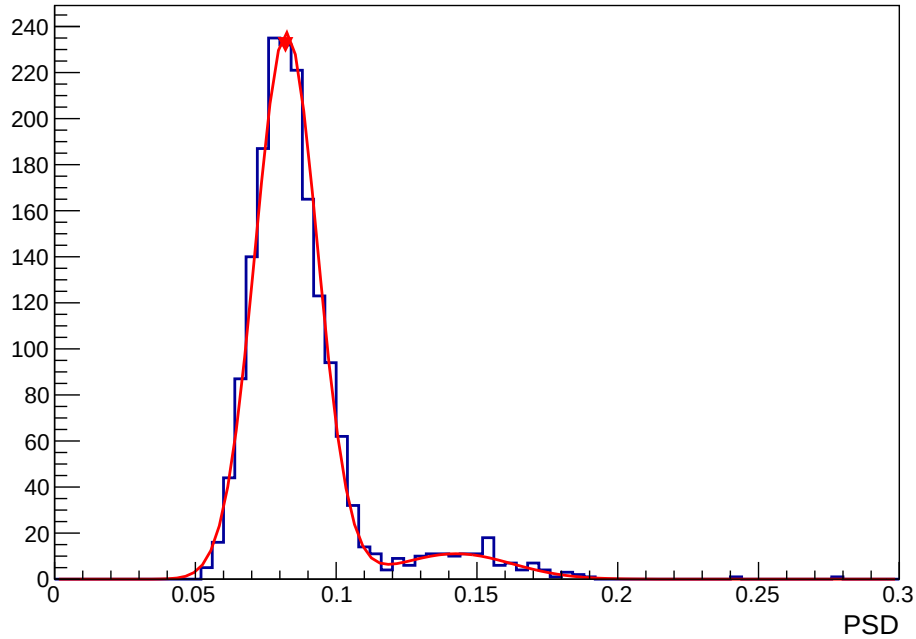

(b) Projection of PSD histogram in the QDC range of 200×10^3 to 220×10^3. The red curve shows a fit to the spectrum using a convolution of two Gaussian functions. The peaks at lower and higher PSDs are from gammas and neutrons respectively.

Figure 6.9: PSD histograms for module 10 from ^{20}Ne(d,n)^{21}Na reaction. The red gate shown in (a) is the locus of minimum between the gamma and neutron peaks, as shown in (b), for different QDC ranges. This gate was used to remove the gamma background.

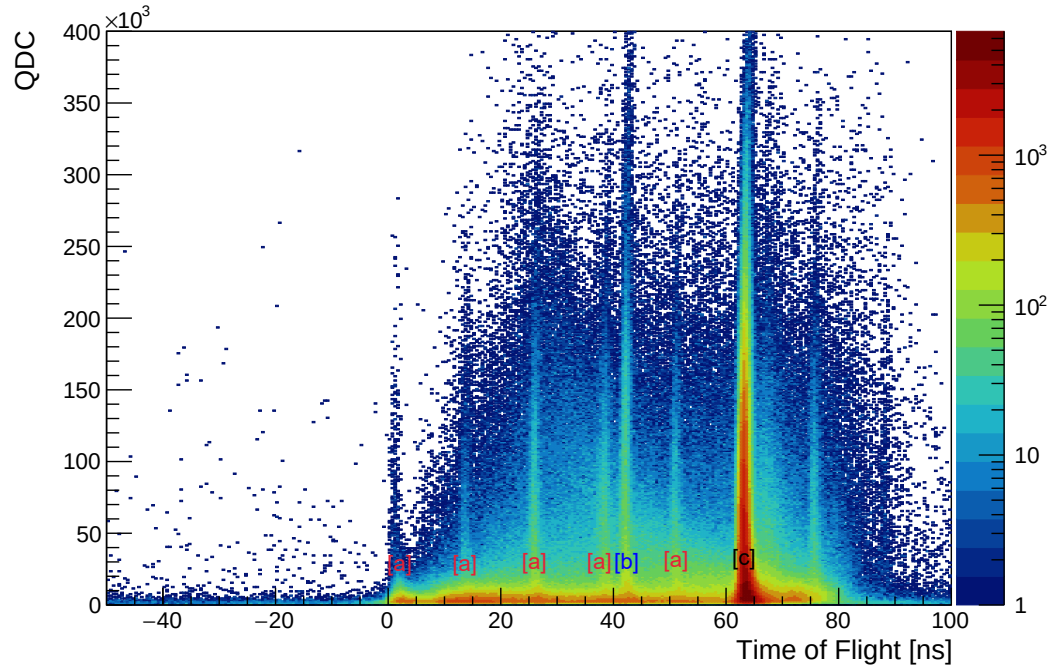

(a) TOF-QDC histogram before applying the PSD gate. a denotes gamma flashes from the reaction due to the leakage from the harmonic buncher. b denotes gamma peak from the beam stop. c denotes the prompt gamma flash from the reaction.

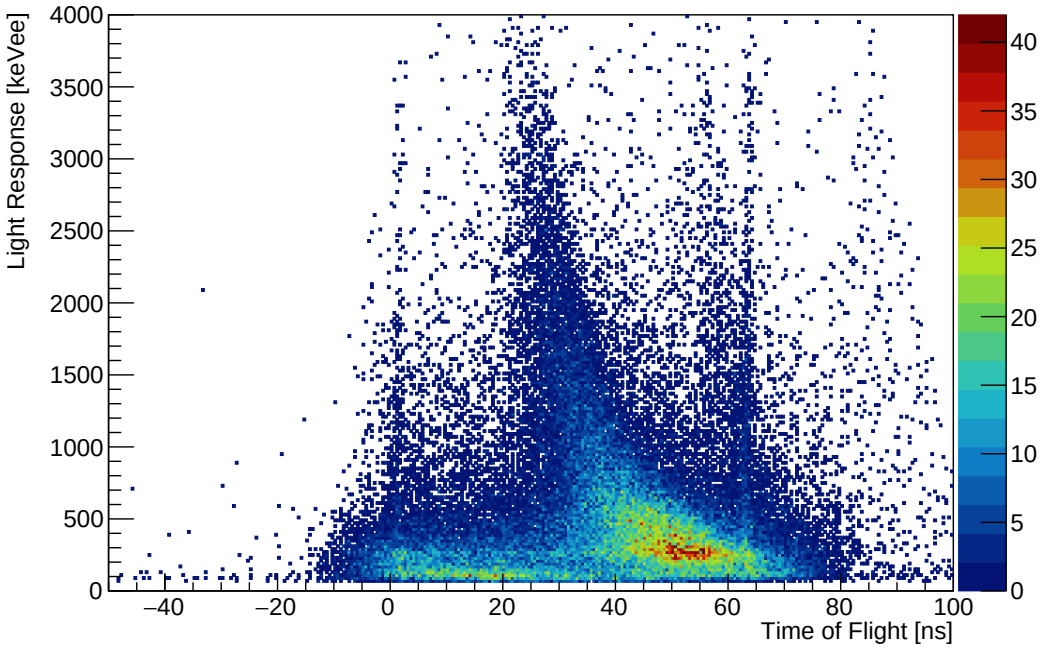

(b) TOF-QDC histogram after applying the PSD gate showing the 'banana' structure from the neutrons.

Figure 6.10: TOF-QDC histograms

and these have an actual TOF of 167.5 ns for the module at 92.58°, after accounting for the time taken by the beam to reach the beam stop and the gamma rays produced at the beam stop to reach the detector. Since the event window is 62.1 ns, this peak appears at 42.5 ns after two wraparounds. After gating on the neutrons on the PSD-QDC spectrum, most of the gamma background can be removed. Applying this gate to the TOF-QDC spectrum, we can see a 'banana'-shaped structure arising (Figure 6.10b), which comes from the neutrons.

This specific shape is due to the quadratic relation between the TOF and the energy of the neutrons which affects the light yield. A so-called banana gate can be used to make a boundary between sensible neutron detection events and noise. For given neutron energy and its corresponding TOF, there is a maximum light yield, and events below this gate are considered valid.

6.3.5 Summary and Future Work

Neutron detection is a challenging task due to the lack of direct ionization. In a (d, n) reaction, a huge amount of gamma rays is produced and plastic scintillator detectors are sensitive to both neutrons and gamma rays. Using the pulse shape discriminating capability of NEXT, we were able to remove a considerable amount of gamma-ray background and identified neutron events from beam-target interactions.

The full potential of NEXT lies in its segmentation. It has 8 layers in the direction of neutron interaction, each with a thickness of 6 mm. Hence, the point of neutron interaction inside the detector can be determined within 6 mm of position accuracy. The TOF of neutrons has to be corrected using the position map of NEXT which will give a better resolution. The neutrons are overwhelmed by the gamma background even after gating on the PSD. We can quantify the room background by using the beam-off data. It is necessary to combine the data from all the modules to maximize the statistics. Since the energies of the neutrons emerging from the reaction kinematics depend on the laboratory angle, we need to convert the TOF of the neutrons into the Q value of the reaction, thus removing the angular dependence. After combining all the data, we can analyze the Q value spectrum and identify the proton states in ^{21}Na populated by this reaction.

Bibliography

[1] Machleidt R, Entem DR. Chiral effective field theory and nuclear forces. Physics Reports. 2011;503(1):1 – 75. Available from: http://www.sciencedirect.com/science/article/pii/S0370157311000457. 1

[2] Jurgenson ED, Maris P, Furnstahl RJ, Navrátil P, Ormand WE, Vary JP. Structure of p-shell nuclei using three-nucleon interactions evolved with the similarity renormalization group. Phys Rev C. 2013 May;87:054312. Available from: https://link.aps.org/doi/10.1103/PhysRevC.87.054312. 1

[3] Barrett BR, Navrátil P, Vary JP. Ab initio no core shell model. Progress in Particle and Nuclear Physics. 2013;69:131–181. Available from: https://www.sciencedirect.com/science/article/pii/S0146641012001184. 1

[4] Hagen G, Papenbrock T, Ekström A, Wendt KA, Baardsen G, Gandolfi S, et al. Coupled-cluster calculations of nucleonic matter. Phys Rev C. 2014 Jan;89:014319. Available from: https://link.aps.org/doi/10.1103/PhysRevC.89.014319. 1

[5] Hagen G, Papenbrock T, Hjorth-Jensen M, Dean DJ. Coupled-cluster computations of atomic nuclei. Reports on Progress in Physics. 2014 sep;77(9):096302. Available from: https://doi.org/10.1088/0034-4885/77/9/096302. 1

[6] Carlson J, Gandolfi S, Pederiva F, Pieper SC, Schiavilla R, Schmidt KE, et al. Quantum Monte Carlo methods for nuclear physics. Rev Mod Phys. 2015 Sep;87:1067–1118. Available from: https://link.aps.org/doi/10.1103/RevModPhys.87.1067. 1

[7] Woolsey A. Investigation of the Thermal Neutron Diffusion Length in Graphite; 2018. 2

[8] Jensen AS, Riisager K, Fedorov DV, Garrido E. Structure and reactions of quantum halos. Rev Mod Phys. 2004 Feb;76:215–261. Available from: https://link.aps.org/doi/10.1103/RevModPhys.76.215. 3

[9] Tanihata I, Hamagaki H, Hashimoto O, Nagamiya S, Shida Y, Yoshikawa N, et al. Measurements of interaction cross sections and radii of He isotopes. Physics Letters

B. 1985;160(6):380 – 384. Available from: http://www.sciencedirect.com/science/article/pii/037026938590005X. 3

[10] Bakken. English Wikipedia, CC BY-SA 3.0; 2020. Available from: https://commons.wikimedia.org/w/index.php?curid=15039395. 4

[11] Mayer MG. On Closed Shells in Nuclei. Phys Rev. 1948 Aug;74:235–239. Available from: https://link.aps.org/doi/10.1103/PhysRev.74.235. 5

[12] Haxel O, Jensen JHD, Suess HE. On the "Magic Numbers" in Nuclear Structure. Phys Rev. 1949 Jun;75:1766–1766. Available from: https://link.aps.org/doi/10.1103/PhysRev.75.1766.2. 5

[13] Warburton EK, Brown BA. Effective interactions for the 0p1s0d nuclear shell-model space. Phys Rev C. 1992 Sep;46:923–944. Available from: https://link.aps.org/doi/10.1103/PhysRevC.46.923. 6

[14] Bohr A, Mottelson BR. Nuclear Structure. World Scientific Publishing Company; 1998. Available from: https://www.worldscientific.com/doi/abs/10.1142/3530. 8

[15] Ring P. The nuclear many-body problem. Texts and monographs in physics. New York: Springer-Verlag; 1980. 8, 9

[16] Krane KS. Introductory nuclear physics. New York, NY: Wiley; 1988. Available from: https://cds.cern.ch/record/359790. 7

[17] Nilsson SG. Binding states of individual nucleons in strongly deformed nuclei. Kong Dan Vid Sel Mat Fys Med. 1955;29N16:1–69. 9, 65

[18] Firestone RB, Shirley VS, Baglin CM, Chu SYF, Zipkin J. The Table of Isotopes-8th Edition. New York, NY: Wiley; 1996. 10

[19] Vaagen JS, Gridnev DK, Heiberg-Andersen H, Danilin BV, Ershov SN, Zagrebaev VI, et al. Borromean Halo Nuclei. Physica Scripta. 2000;T88(1):209. Available from: https://doi.org/10.1238/physica.topical.088a00209. 11

[20] Wimmer K, Kröll T, Krücken R, Bildstein V, Gernhäuser R, Bastin B, et al. Discovery of the Shape Coexisting 0^+ State in ^{32}Mg by a Two Neutron Transfer Reaction. Phys Rev Lett. 2010 Dec;105:252501. Available from: https://link.aps.org/doi/10.1103/PhysRevLett.105.252501. 13

[21] Al-Khalili J. In: An Introduction to Halo Nuclei. vol. 651; 2004. p. 77–112. 12

[22] Grigorenko L, Fomichev A, Ter-Akopian G. Light Exotic Nuclei at JINR: ACCULINNA and ACCULINNA-2 Facilities. Nuclear Physics News. 2014;24(4):22–27. Available from: https://doi.org/10.1080/10619127.2014.972180. 12

[23] Kravvaris K, Volya A. Study of clustering in isotopes of beryllium. AIP Conference Proceedings. 2018;2038(1):020026. Available from: https://aip.scitation.org/doi/abs/10.1063/1.5078845. 13

[24] von Oertzen W. Dimers based on the $\alpha + \alpha$ potential and chain states of carbon isotopes. Zeitschrift für Physik A Hadrons and Nuclei. 1997 Dec;357(4):355–365. Available from: https://doi.org/10.1007/s002180050255. 13

[25] Tanihata I. Neutron halos and exotic modes. Nuclear Physics, A. Dec 1990:411c–425c. Available from: http://inis.iaea.org/search/search.aspx?orig_q=RN:22030688. 13

[26] Tarutina T, Thompson IJ, Tostevin JA. Study of 14Be with core excitation. Nuclear Physics A. 2004;733(1):53 – 66. Available from: http://www.sciencedirect.com/science/article/pii/S0375947403019535. 13

[27] Descouvemont P. Halo structure of ^{14}Be in a microscopic ^{12}Be+n+n cluster model. Phys Rev C. 1995 Aug;52:704–710. Available from: https://link.aps.org/doi/10.1103/PhysRevC.52.704. 13

[28] Volya A, Zelevinsky V. Continuum shell model and nuclear physics at the edge of stability. Physics of Atomic Nuclei. 2014;77(8):969–982. Available from: https://doi.org/10.1134/S1063778814070163. 13

[29] Poppelier NAFM, Wood LD, Glaudemans PWM. Properties of exotic p-shell nuclei. Physics Letters B. 1985;157(2):120 – 122. Available from: http://www.sciencedirect.com/science/article/pii/0370269385915291. 13, 15

[30] Ostrowski AN, Bohlen HG, Demyanova AS, Gebauer B, Kalpakchieva R, Langner C, et al. Mass spectroscopy of13Be. Zeitschrift für Physik A Hadrons and Nuclei. 1992;343(4):489–490. Available from: https://doi.org/10.1007/BF01289828. 13, 14, 15, 16, 67

[31] Fortune HT. Unraveling the structure of ^{13}Be. Phys Rev C. 2013 Jan;87:014305. Available from: https://link.aps.org/doi/10.1103/PhysRevC.87.014305. 14

[32] Randisi G, Leprince A, Al Falou H, Orr NA, Marqués FM, Achouri NL, et al. Structure of ^{13}Be probed via secondary-beam reactions. Phys Rev C. 2014 Mar;89:034320. Available from: https://link.aps.org/doi/10.1103/PhysRevC.89.034320. 14, 15, 16, 67, 77, 78, 84

[33] Macchiavelli AO, Crawford HL, Campbell CM, Clark RM, Cromaz M, Fallon P, et al. Analysis of spectroscopic factors in ^{11}Be and ^{12}Be in the Nilsson strong-coupling limit. Phys Rev C. 2018 Jan;97:011302. Available from: https://link.aps.org/doi/10.1103/PhysRevC.97.011302. 14, 15

[34] Aleksandrov DV, Ganza EA, Glukhov YA. Observation of the isotope 13Be in the reaction 14C(7Li, 8B). Soviet Journal of Nuclear Physics. 1983;37(3):474–475. Available from: http://inis.iaea.org/search/search.aspx?orig_q=RN:15008476. 14, 16, 67

[35] Belozyorov AV, Kalpakchieva R, Penionzhkevich YE, Dlouhý Z, Piskor˘ S, Vincour J, et al. Spectroscopy of 13Be. Nuclear Physics A. 1998;636(4):419 – 426. Available from: http://www.sciencedirect.com/science/article/pii/S0375947498002176. 14, 16

[36] Simon H, Meister M, Aumann T, Borge MJG, Chulkov LV, Pramanik UD, et al. Systematic investigation of the drip-line nuclei 11Li and 14Be and their unbound subsystems 10Li and 13Be. Nuclear Physics A. 2007;791(3):267 – 302. Available

from: http://www.sciencedirect.com/science/article/pii/S037594740700509X. 14, 16, 67

[37] Kondo Y, Nakamura T, Satou Y, Matsumoto T, Aoi N, Endo N, et al. Low-lying intruder state of the unbound nucleus 13Be. Physics Letters B. 2010;690(3):245 – 249. Available from: http://www.sciencedirect.com/science/article/pii/S0370269310006234. 14, 16, 67, 72, 77, 81, 84

[38] Aksyutina Y, Aumann T, Boretzky K, Borge MJG, Caesar C, Chatillon A, et al. Structure of the unbound nucleus ^{13}Be: One-neutron knockout reaction data from ^{14}Be analyzed in a holistic approach. Phys Rev C. 2013 Jun;87:064316. Available from: https://link.aps.org/doi/10.1103/PhysRevC.87.064316. 14, 16, 77, 83, 84

[39] Corsi A, Kubota Y, Casal J, Gómez-Ramos M, Moro AM, Authelet G, et al. Structure of 13Be probed via quasi-free scattering. Physics Letters B. 2019;797:134843. Available from: http://www.sciencedirect.com/science/article/pii/S037026931930557X. 14, 16, 67, 72, 77, 82, 84

[40] Korsheninnikov AA, Nikolskii EY, Kobayashi T, Aleksandrov DV, Fujimaki M, Kumagai H, et al. Spectroscopy of 12Be and 13Be using a 12Be radioactive beam. Physics Letters B. 1995;343(1):53–58. Available from: https://www.sciencedirect.com/science/article/pii/037026939401435F. 16

[41] von Oertzen W, Bohlen HG, Gebauer B, von Lucke-Petsch M, Ostrowski AN, Seyfert C, et al. Nuclear structure studies of very neutron-rich isotopes of 7–10He, 9–11Li and 12–14Be via two-body reactions. Nuclear Physics A. 1995;588(1):c129–c134. Proceedings of the Fifth International Symposium on Physics of Unstable Nuclei. Available from: https://www.sciencedirect.com/science/article/pii/037594749500111D. 16

[42] Thoennessen M, Yokoyama S, Hansen PG. First evidence for low lying s-wave strength in ^{13}Be. Phys Rev C. 2000 Dec;63:014308. Available from: https://link.aps.org/doi/10.1103/PhysRevC.63.014308. 16

[43] Ribeiro G, Nácher E, Tengblad O, Díaz Fernández P, Aksyutina Y, Alvarez-Pol H, et al. Structure of ^{13}Be studied in proton knockout from ^{14}B. Phys Rev C. 2018 Aug;98:024603. Available from: https://link.aps.org/doi/10.1103/PhysRevC.98.024603. 16, 72, 77, 79, 84

[44] Glendenning NK. Direct nuclear reactions. New York: Academic Press; 1983. 19

[45] Perey CM, Perey FG. Compilation of phenomenological optical-model parameters 1954–1975. Atomic Data and Nuclear Data Tables. 1976;17(1):1–101. Available from: https://www.sciencedirect.com/science/article/pii/0092640X76900073. 27, 72

[46] Daehnick WW, Childs JD, Vrcelj Z. Global optical model potential for elastic deuteron scattering from 12 to 90 MeV. Phys Rev C. 1980 Jun;21:2253–2274. Available from: https://link.aps.org/doi/10.1103/PhysRevC.21.2253. 27, 72

[47] Lohr JM, Haeberli W. Elastic scattering of 9–13 MeV vector polarized deuterons. Nuclear Physics A. 1974;232(2):381–397. Available from: https://www.sciencedirect.com/science/article/pii/0375947474906277. 27, 72

[48] Tostevin JA. Reaction Codes; 2022. Available from: http://nucleartheory.eps.surrey.ac.uk/NPG/code.htm. 27, 69

[49] Varner RL, Thompson WJ, McAbee TL, Ludwig EJ, Clegg TB. A global nucleon optical model potential. Physics Reports. 1991;201(2):57–119. Available from: https://www.sciencedirect.com/science/article/pii/0370157391900390. 27

[50] Koning AJ, Delaroche JP. Local and global nucleon optical models from 1 keV to 200 MeV. Nuclear Physics A. 2003;713(3):231–310. Available from: https://www.sciencedirect.com/science/article/pii/S0375947402013210. 27, 72

[51] Ball GC, Hackman G, Krücken R. The TRIUMF-ISAC facility: two decades of discovery with rare isotope beams. Physica Scripta. 2016 jul;91(9):093002. Available from: https://iopscience.iop.org/article/10.1088/0031-8949/91/9/093002. 30

[52] Kanungo R. IRIS: The ISAC charged particle reaction spectroscopy facility for reaccelerated high-energy ISOL beams. Hyperfine Interactions. 2014;225(1):235–240. Available from: https://doi.org/10.1007/s10751-013-0904-8. 30, 31, 32, 33, 35, 37

[53] YY1 Micron Semiconductors;. Available from: http://www.micronsemiconductor.co.uk/product/yy1/. 35

[54] S3 Micron Semiconductors;. Available from: http://www.micronsemiconductor.co.uk/product/s3/. 36, 37

[55] Knoll GF. Radiation detection and measurement. 4th ed. Hoboken, N.J: John Wiley; 2010. 36, 101

[56] O B Tarasov DB. LISE++; 2022. Available from: http://lise.nscl.msu.edu/introduction.html. 44

[57] Quaglioni S. Light and unbound nuclei. The European Physical Journal Plus. 2018 Sep;133(9):385. Available from: https://doi.org/10.1140/epjp/i2018-12238-0. 54

[58] Agostinelli S, Allison J, Amako K, Apostolakis J, Araujo H, Arce P, et al. Geant4—a simulation toolkit. Nuclear Instruments and Methods in Physics Research Section A: Accelerators, Spectrometers, Detectors and Associated Equipment. 2003;506(3):250–303. Available from: https://www.sciencedirect.com/science/article/pii/S0168900203013688. 57

[59] Nogueira F. Bayesian Optimization: Open source constrained global optimization tool for Python; 2014–. Available from: https://github.com/fmfn/BayesianOptimization. 58

[60] Mockus J. On Bayesian methods for seeking the extremum. Optimization Techniques IFIP Technical Conference. 1974:400–404. Cited By 102. 58

[61] Snoek J, Larochelle H, Adams RP. Practical Bayesian Optimization of Machine Learning Algorithms. In: Pereira F, Burges CJC, Bottou L, Weinberger KQ, editors.

Advances in Neural Information Processing Systems. vol. 25. Curran Associates, Inc.; 2012. Available from: https://proceedings.neurips.cc/paper/2012/file/05311655a15b75fab86956663e1819cd-Paper.pdf. 58

[62] Rasmussen CE, Williams CKI. Gaussian Processes for Machine Learning (Adaptive Computation and Machine Learning). The MIT Press; 2005. 58

[63] Frazier PI. A Tutorial on Bayesian Optimization; 2018. 58, 59

[64] Genton MG. Classes of kernels for machine learning: a statistics perspective. Journal of machine learning research. 2001;2(Dec):299–312. 60

[65] Hooker J, Kovoor J, Jones KL, Kanungo R, Alcorta M, Allen J, et al. Use of Bayesian Optimization to understand the structure of nuclei. Nuclear Instruments and Methods in Physics Research Section B: Beam Interactions with Materials and Atoms. 2022;512:6–11. Available from: https://www.sciencedirect.com/science/article/pii/S0168583X21003906. 61, 62, 63

[66] Pain SD, Catford WN, Orr NA, Angélique JC, Ashwood NI, Bouchat V, et al. Structure of ^{12}Be: Intruder d-Wave Strength at $N = 8$. Phys Rev Lett. 2006 Jan;96:032502. Available from: https://link.aps.org/doi/10.1103/PhysRevLett.96.032502. 64

[67] Iwasaki H, Motobayashi T, Akiyoshi H, Ando Y, Fukuda N, Fujiwara H, et al. Quadrupole deformation of 12Be studied by proton inelastic scattering. Physics Letters B. 2000;481(1):7–13. Available from: https://www.sciencedirect.com/science/article/pii/S0370269300004287. 64

[68] Thompson IJ. Coupled reaction channels calculations in nuclear physics. Computer Physics Reports. 1988;7(4):167–212. Available from: https://www.sciencedirect.com/science/article/pii/0167797788900056. 69

[69] Bertsch GF, Hencken K, Esbensen H. Nuclear breakup of Borromean nuclei. Phys Rev C. 1998 Mar;57:1366–1377. Available from: https://link.aps.org/doi/10.1103/PhysRevC.57.1366. 80

[70] Sangster RC, Irvine JW. Study of Organic Scintillators. The Journal of Chemical Physics. 1956;24(4):670–715. Available from: https://doi.org/10.1063/1.1742595. 88

[71] Zaitseva N, Glenn A, Carman L, Hatarik R, Hamel S, Faust M, et al. Pulse Shape Discrimination in Impure and Mixed Single-Crystal Organic Scintillators. IEEE Transactions on Nuclear Science. 2011;58(6):3411–3420. 88, 89

[72] Ranucci G. An analytical approach to the evaluation of the pulse shape discrimination properties of scintillators. Nuclear Instruments and Methods in Physics Research Section A: Accelerators, Spectrometers, Detectors and Associated Equipment. 1995;354(2):389 – 399. Available from: http://www.sciencedirect.com/science/article/pii/0168900294008868. 88

[73] Heideman J, Pérez-Loureiro D, Grzywacz R, Thornsberry CR, Chan J, Heilbronn LH, et al. Conceptual design and first results for a neutron detector with interaction localization capabilities. Nuclear Instruments and Methods in Physics Research Section A: Accelerators, Spectrometers, Detectors and Associated Equipment. 2019;946:162528. Available from: http://www.sciencedirect.com/science/article/pii/S0168900219310617. 90, 91

[74] Rolfs C, Rodne WS, Shapiro MH, Winkler H. Hydrogen burning of 20Ne and 22Ne in stars. Nuclear Physics A. 1975;241(3):460 – 486. Available from: http://www.sciencedirect.com/science/article/pii/037594747590398X. 94

[75] Lapierre A, Bollen G, Crisp D, Krause SW, Linhardt LE, Lund K, et al. First two operational years of the electron-beam ion trap charge breeder at the National Superconducting Cyclotron Laboratory. Phys Rev Accel Beams. 2018 May;21:053401. Available from: https://link.aps.org/doi/10.1103/PhysRevAccelBeams.21.053401. 95, 96

Vita

Jerome Mathew Kovoor is from Kerala, India. He attended high school at his hometown and went to attend Indian Institute of Science Education and Research, Thiruvananthapuram in Kerala, from where he graduated with a dual degree of Bachelor of Science and Master of Science in Physics with a minor in Mathematics. Later he came to the University of Tennessee, Knoxville to pursue graduate school in 2017.